

**THERMOACOUSTIC ENGINES IN
ALTERNATE GEOMETRY RESONATORS**

FINAL REPORT

**Grant Numbers:
N00014-89-J-3087
N00014-93-1-1125**

**The Jamie Whitten
National Center for
Physical Acoustics**



*The
University of Mississippi*

DTIC QUALITY INSPECTED 3

**THERMOACOUSTIC ENGINES IN
ALTERNATE GEOMETRY RESONATORS**

FINAL REPORT

**Grant Numbers:
N00014-89-J-3087
N00014-93-1-1125**

Submitted to:

**Office of Naval Research
ONR 331
800 North Quincy Street
Arlington, Virginia 22217-5660**

by:

**Richard Raspet and Henry E. Bass and Jay A. Lightfoot
Department of Physics and Astronomy and
National Center for Physical Acoustics
University of Mississippi
University, Mississippi 38677**

PARGUM/NCPA REPORT LC0997-01

September 1997

DTIC QUALITY INSPECTED 3

DISTRIBUTION STATEMENT A

**Approved for public release
Distribution Unlimited**

19971121 046

REPORT DOCUMENTATION PAGEForm Approved
OMB No. 0704-0188

Public reporting burden for this collection of information is estimated to average 1 hour per response, including the time for reviewing instructions, searching existing data sources, gathering and maintaining the data needed, and completing and reviewing the collection of information. Send comments regarding this burden estimate or any other aspect of this collection of information, including suggestions for reducing this burden to Washington Headquarters Services, Directorate for Information Operations and Reports, 1215 Jefferson Davis Highway, Suite 1204, Arlington, VA 22202-4302, and to the Office of Management and Budget, Paperwork Reduction Project (0704-0188), Washington, DC 20503.

1. AGENCY USE ONLY (Leave blank)		2. REPORT DATE 12 Sep 97	3. REPORT TYPE AND DATES COVERED Final Report, 01 Aug 1992 - 14 Sep 1996	
4. TITLE AND SUBTITLE Thermoacoustic Engines in Alternate Geometry Resonators			5. FUNDING NUMBERS PE 61153N	
6. AUTHOR(S) Richard Raspet, H.E. Bass and Jay A. Lightfoot			G N00014-89-J-3087 G N00014-93-1-1125	
7. PERFORMING ORGANIZATION NAME(S) AND ADDRESS(ES) Department of Physics & Astronomy and National Center for Physical Acoustics University of Mississippi University MS 38677			8. PERFORMING ORGANIZATION REPORT NUMBER PARGUM/NCPA Report LC0997-01	
9. SPONSORING / MONITORING AGENCY NAME(S) AND ADDRESS(ES) Office of Naval Research ONR 331 800 North Quincy Street Arlington, VA 22217-5660			10. SPONSORING / MONITORING AGENCY REPORT NUMBER	
11. SUPPLEMENTARY NOTES Ph.D. dissertation of Jay Alan Lightfoot. Reporting covers a parent grant and its associated EPSCoR grant.				
12a. DISTRIBUTION / AVAILABILITY STATEMENT Approved for public release: Distribution unlimited			12b. DISTRIBUTION CODE	
13. ABSTRACT (Maximum 200 words) The purpose of the research reported herein is to branch out from thermoacoustics in the plane wave geometry to study radial wave thermoacoustic engines. Specifically, two possible advantages were sought from radial systems: (i) reduction of harmonic generation due to natural anharmonicity of the resonators and (ii) improved engine performance using naturally sloped stacks. Results show that that the anharmonicity of the resonator significantly reduces non-linear harmonic generation and that sloped stacks significantly improve the refrigerator coefficient of performance in plane wave systems.				
14. SUBJECT TERMS Thermoacoustic engines; Thermoacoustic refrigerators; Radial wave prime movers and refrigerators			15. NUMBER OF PAGES 130	
			16. PRICE CODE	
17. SECURITY CLASSIFICATION OF REPORT UNCLASSIFIED	18. SECURITY CLASSIFICATION OF THIS PAGE UNCLASSIFIED	19. SECURITY CLASSIFICATION OF ABSTRACT UNCLASSIFIED	20. LIMITATION OF ABSTRACT	

THERMOACOUSTIC ENGINES IN ALTERNATE GEOMETRY RESONATORS

A Dissertation

Presented for the

Doctor of Philosophy

Degree

The University of Mississippi

Jay Alan Lightfoot

May, 1997

DEDICATION

This dissertation is dedicated to my wife

Debbie,

my best friend and the love of my life.

ACKNOWLEDGMENTS

I would like to thank Dr. Richard Raspet, Dr. Henry Bass, and Dr. Pat Arnott for sharing their expertise and experience as well as for their patience with my lack thereof. I would also like to thank the remaining committee members, Dr. Bruce Denardo and Dr. Jeff Roux. I am grateful to Dr. Doug Shields for my early exposure to research in graduate school. Many thanks go to Mike Booke, Mike Reep, and Paul Dakin for their excellent machining and to Michael Ossofsky and Robert Abbott for constructing the heat exchangers for the radial wave prime mover. Thanks also go to Jim Belcher, my fellow Arkansas Razorback fan and thermoacoustics cohort; Keith Olree, Sean Neill, Matt Miley, David Brown, and Hari Eswaren who suffered through the course work with me and actually made it fun ... sometimes; Nancy Cramer for handling many office details; Jeremy Webster, Sean Cordry, Carl Frederickson, Chris Lawrenson, Mark Sprague, and Stephen Wood. Special thanks go to the National Center for Physical Acoustics for the fellowship which made graduate school financially possible, and to the Office of Naval Research for funding the NCPA fellowship and supporting this work through the Environmentally Safe Ships Program. I am also grateful to my parents, Dan and Dolores Lightfoot, for their love and support. Finally, I wish to thank my wonderful wife, Debbie, who throughout my graduate work has endured a difficult job in addition to a difficult husband.

ABSTRACT

The purpose of this research is to branch out from thermoacoustics in the plane wave geometry to study radial wave thermoacoustic engines. Two possible advantages of radial systems are proposed: a reduction in harmonic generation due to the natural anharmonicity of the resonator, and the possibility of improved engine performance using naturally sloped stacks.

The radial wave prime mover is described. Experimental results for the temperature at which oscillations begin are compared with theoretical predictions. Accounting for a pore distribution in the stack and temperature discontinuities between the stack and heat exchangers, theory and experiment are shown to be in agreement. In addition, spectral measurements in the radial prime mover show that the anharmonicity of the resonator significantly reduces non-linear harmonic generation.

To gain a better understanding of naturally sloped stacks in the radial engine, the physics of sloped stacks is extended to the plane geometry, where fewer constraints exist. A theoretical treatment of thermoacoustic engines with varying stack pore cross-section and/or varying resonator cross-section in the temperature gradient supporting stack region is presented along with numerical results for plane and radial wave prime movers and refrigerators. Results show significant improvements in refrigerator coefficient of performance in plane wave systems.

TABLE OF CONTENTS

1 INTRODUCTION.....	1
1.1 MOTIVATION FOR STUDYING THERMOACOUSTIC ENGINES.....	1
1.2 PREVIOUS RELEVANT RESEARCH IN THERMOACOUSTICS.....	3
1.3 OVERVIEW OF DISSERTATION	4
2 REVIEW OF RADIAL WAVE THERMOACOUSTIC THEORY	6
2.1 INTRODUCTION.....	6
2.2 BASIC EQUATIONS AND ASSUMPTIONS.....	7
2.3 AREA AVERAGED EQUATION OF MOTION IN A PORE.....	12
2.4 AREA AVERAGED EQUATION OF STATE IN A PORE.....	13
2.5 ACOUSTIC PRESSURE WAVE EQUATION	15
2.6 FIRST ORDER IMPEDANCE EQUATION.....	16
2.7 SPECIFIC ACOUSTIC IMPEDANCE AND PRESSURE TRANSLATION THEOREMS.....	17
2.8 NUMERICAL DETERMINATION OF ONSET TEMPERATURE	18
2.9 THE IMPORTANCE OF ONSET TEMPERATURE	22
3 RADIAL WAVE THERMOACOUSTIC PRIME MOVER DESIGN.....	23
3.1 INTRODUCTION.....	23
3.2 INITIAL DESIGN I: SMALL ALUMINUM/STEEL RESONATOR.....	23

3.3 INITIAL DESIGN II: LARGE CONCRETE/PLYWOOD RESONATOR.....	32
3.3.1 <i>Plane wave model</i>	33
3.3.2 <i>Radial Wave Model</i>	36
3.4 FINAL DESIGN.....	37
3.5 EXPERIMENTAL MEASUREMENTS AND ASSOCIATED ERRORS	46
4 RADIAL WAVE THERMOACOUSTIC PRIME MOVER EXPERIMENTAL RESULTS AND COMPARISON TO THEORY.....	47
4.1 INTRODUCTION	47
4.2 COMPARISON OF PLANE AND RADIAL WAVE HARMONIC GENERATION	48
4.3 INITIAL COMPARISON OF EXPERIMENTAL AND THEORETICAL ONSET TEMPERATURES	56
4.4 NON-UNIFORM STACK PLATE SPACING.....	60
4.5 TEMPERATURE DISCONTINUITIES BETWEEN THE HEAT EXCHANGER AND THE STACK FACE	67
5 THEORY OF SLOPED STACKS IN PLANE AND RADIAL WAVE THERMOACOUSTIC ENGINES	81
5.1 INTRODUCTION	81
5.2 PREVIOUS RELEVANT ANALYSIS.....	86
5.3 WAVE EQUATION FOR THERMOACOUSTIC ENGINES WITH SLOPED STACKS.....	88

5.4 PRESSURE, BULK VELOCITY, AND SPECIFIC ACOUSTIC IMPEDANCE.....	91
5.5 ENTHALPY FLOW	93
5.6 FINITE DIFFERENCE SOLUTION	94
6 SLOPED STACK RESULTS FOR PLANE AND RADIAL WAVE PRIME	
MOVERS AND REFRIGERATORS	96
6.1 INTRODUCTION.....	96
6.2 PRIME MOVER RESULTS	101
<i>6.2.1 Plane Wave Prime Mover.....</i>	<i>101</i>
<i>6.2.2 Radial Wave Prime Mover</i>	<i>107</i>
6.3 REFRIGERATOR RESULTS	109
<i>6.3.1 Plane Wave Refrigerator.....</i>	<i>109</i>
<i>6.3.2 Radial Wave Refrigerator</i>	<i>116</i>
7 CONCLUSIONS.....	117
LIST OF REFERENCES	122

LIST OF FIGURES

Figure 2.1:	Stack design assumed for deriving the radial wave thermoacoustic equations.	8
Figure 2.2:	Radial geometry definitions.....	9
Figure 2.3:	Radial wave prime mover schematic for describing the numerical implementation of the radial thermoacoustic theory.	19
Figure 3.1:	Original radial wave thermoacoustic prime mover.	24
Figure 3.2:	Schematic of a single element of the radial prime mover stack.	27
Figure 3.3:	Schematic of spacers used in constructing the radial stack.	28
Figure 3.4:	Schematic of a single element used to create the original cold heat exchanger.	30
Figure 3.5:	Schematic of the plane wave prime mover model with dimensions similar to those of the large radial wave prime mover.	34
Figure 3.6:	Schematic of the resonator portion of the large radial prime mover.	38
Figure 3.7:	The radial wave thermoacoustic prime mover.	40
Figure 3.8:	Radial wave prime mover thermoacoustic elements.	41
Figure 3.9:	A single stack element from the radial wave thermoacoustic prime mover.	42
Figure 3.10:	Professional line drawing of the radial wave prime mover.....	44

Figure 4.1:	Radial prime mover acoustic spectrum.	53
Figure 4.2:	Plane prime mover acoustic spectrum.	55
Figure 4.3:	Experimental onset temperatures for air-filled radial prime mover and original theoretical predictions.	58
Figure 4.4:	Experimental onset temperatures for argon-filled radial prime mover and original theoretical predictions.	59
Figure 4.5:	Distribution of plate spacing in the radial prime mover stack.	62
Figure 4.6:	Illustration of the gaps present between the radial stack and heat exchangers.	69
Figure 4.7:	Demonstration of the temperature discontinuity between stack and heat exchanger for $\ell/L = .036$	72
Figure 4.8:	Demonstration of the temperature discontinuity between stack and heat exchanger for $\ell/L = .002$	73
Figure 4.9:	Comparison of experiment and theory including stack-heat exchanger gaps for air with $\ell_{eff} = 0.2$ mm.	76
Figure 4.10:	Comparison of experiment and theory including stack-heat exchanger gaps for argon with $\ell_{eff} = 0.2$ mm.	77
Figure 4.11:	Comparison of experiment and theory including stack-heat exchanger gaps for air with $\ell_{eff} = 0.41$ mm.	79

Figure 4.12:	Comparison of experiment and theory including stack-heat exchanger gaps for argon with $\ell_{eff} = 0.41$ mm.	80
Figure 5.1:	$\text{Im}[F^*(\lambda_T) / F^*(\lambda)]$ as a function of plate spacing.	82
Figure 5.2:	Thermal penetration depth as a function of temperature.	83
Figure 5.3:	Stacks in the radial geometry.	85
Figure 5.4:	Sloped stack plane wave thermoacoustic engine.	87
Figure 6.1:	Onset temperatures as a function of pressure for the sloped and parallel stacks in a radial prime mover.	97
Figure 6.2:	Plane wave stacks used in prime mover and refrigerator calculations.	99
Figure 6.3:	Maximum acoustic power and stack plate spacing as a function of stack location in the plane wave prime mover.	103
Figure 6.4:	Velocity and impedance at the cold side of the plane wave prime mover stack where acoustic power is generated.	106
Figure 6.5:	Maximum acoustic power and plate spacing over a range of stack locations in the radial wave prime mover.	108
Figure 6.6:	Maximum COP and plate spacings over a range of stack locations in the plane wave refrigerators.	110

Figure 6.7:	Velocity and temperature profiles in the parallel and segmented plane wave stacks.....	112
Figure 6.8:	Velocity and temperature profiles in the varying tube cross-section parallel and sloped plane wave stacks.	114
Figure 6.9:	Maximum COP and plate spacings over a range of stack locations in the radial wave refrigerator.	117

LIST OF TABLES

Table 3.1:	Description of the original small radial wave prime mover.....	25
Table 3.2:	Description of the plane wave prime mover with dimensions similar to those of the large radial wave prime mover.	35
Table 3.3:	Description of the large radial wave prime mover.....	45

LIST OF SYMBOLS

<i>Symbol</i>	<i>Description</i>
A_i	resonator cross-section covered by a given pore size
A_{hot}	resonator cross-section at the hot side of the stack
A_{res}	resonator cross-sectional area
A_p	pore cross-sectional area
a	resonator radius
COP	coefficient of performance
c	sound speed
c_p	isobaric heat capacity per unit mass
F	thermoviscous dissipation function
f_0	resonance frequency
h	resonator axial height
$H_m^{(j)}$	Hankel function of order m and type j
\bar{H}_2	enthalpy flow
i	$\sqrt{-1}$
Im	imaginary part of a quantity

k	acoustic propagation constant
k_0	adiabatic acoustic propagation constant
ℓ	length of gap between stack and heat exchanger
ℓ_{eff}	effective length of gap between stack and heat exchanger
L	stack length
n	total number of pores in a section
N_{Pr}	Prandtl number
p	total pressure
p_0	ambient pressure
p_1	acoustic pressure
P_i	acoustic pressure at the hot side of the stack for a given pore size
P_j	acoustic pressure at the cold side of the stack for a given pore size
P_{cold}	acoustic pressure at the cold face of the stack
P_{hot}	acoustic pressure at the hot face of the stack
Q	quality factor of resonance
\bar{Q}_2	heat flow
R	twice pore cross-sectional area divided by pore perimeter
r	radial coordinate
$\hat{\mathbf{r}}$	radial unit vector

Re	real part of a quantity
s	total entropy
s_0	ambient entropy
s_l	acoustic or excess entropy
t	time
T	total temperature
T_0	ambient temperature
T_H	hot heat exchanger temperature
T_C	cold heat exchanger temperature
T_l	acoustic or excess temperature
ΔT	onset temperature difference (at which acoustic oscillations begin)
\mathbf{v}	total particle velocity vector
v_z	transverse particle velocity
v_r	radial component of the particle velocity
V_i	volume velocity at the hot side of the stack for a given pore size
V_j	volume velocity at the cold side of the stack for a given pore size
V_{cold}	volume velocity at the hot side of the stack
V_{hot}	volume velocity at the hot side of the stack
V_{rb}	bulk particle velocity
\overline{W}_2	work flow

Z	specific acoustic impedance
z	axial coordinate
\hat{z}	axial unit vector
Z_{int}	intrinsic impedance
Z_{bl}	boundary layer specific acoustic impedance
α	function used in stack impedance equation
β	volume coefficient of expansion
γ	ratio of isobaric to isochoric specific heats
δ_K	thermal penetration depth
δ_v	viscous penetration depth
η	dynamic viscosity
θ	azimuthal coordinate
κ	thermal conductivity
κ_C	thermal conductivity of cold fluid in gap
κ_H	thermal conductivity of hot fluid in gap
κ_S	thermal conductivity of stack at midpoint temperature
λ	shear wave number = $R\sqrt{2} / \delta_v$
λ_T	thermal disturbance number = $R\sqrt{2} / \delta_K$
ρ	total gas density

ρ_0	ambient gas density
ρ_l	acoustic gas density
Ω	stack or heat exchanger porosity
Ω_i	stack porosity of a given pore size
ω	angular frequency

Chapter 1

Introduction

1.1 Motivation for Studying Thermoacoustic Engines

During the twentieth century, refrigerators and air conditioners in the United States have evolved from being luxuries, to modern conveniences, to necessities. As governments have become more environmentally conscious, refrigerants have been closely scrutinized. In particular, it has been determined that Chloroflourocarbons (CFCs) and Hydrochloroflourocarbons (HCFCs) are destroying the earth's protective ozone layer. The diminishing of the ozone layer leads to increased levels of ultraviolet (UV) radiation reaching the Earth's surface. For people, overexposure to UV rays can lead to skin cancer, cataracts, and a weakened immune system. Increased UV can also lead to reduced crop yield and disruptions in the marine food chain.¹ As a result, the manufacture of CFCs has been banned beginning in 1996 in the industrialized countries, and will later be banned in non-industrialized countries. Likewise, the production of the most harmful HCFCs will be banned beginning in 2003.² An ozone friendly refrigerant, Hydroflourocarbon (HFC), has been developed as a temporary substitute for CFC and HCFC. HFCs are considered to be a temporary fix because, although HFC is ozone

friendly, the Global Warming Potential of HFC is estimated to be 3200 times that of carbon dioxide over a twenty year period.^{3,4} Therefore, there is growing pressure for the future control and replacement of HFCs as well.

One approach to providing the world with environmentally safe refrigeration is application of the technological advances in the developing field of thermoacoustics.⁵ The two types of thermoacoustic engines are the thermoacoustic prime mover and the thermoacoustic refrigerator. The thermoacoustic prime mover converts heat from a high-temperature heat source into acoustic power, rejecting waste heat to a low-temperature heat sink.⁵ The thermoacoustic refrigerator uses the compressions and expansions of an acoustic wave in the presence of a solid “stack” to pump heat from a lower temperature reservoir to a higher temperature reservoir. Excellent reviews of thermoacoustic engines are available.^{5,6,7}

Thermoacoustic engines possess several features which are appealing to manufacturers and consumers. First, the operating fluid in thermoacoustic systems is typically Helium, Argon, Xenon, or some mixture of these inert gases.^{8,9} Second, the only moving parts in the thermoacoustic refrigeration system are those related to driving the standing wave in the resonator, and in the case of the heat driven thermoacoustic refrigerator there are no moving parts. Third, thermoacoustic engines are relatively simple in design. These attributes lead to refrigeration systems which are environmentally safe, highly reliable, and easy to manufacture.

1.2 Previous Relevant Research in Thermoacoustics

However, in order for the public to embrace this new technology, it must not only be environmentally safe, but also economical. In an effort to produce thermoacoustic refrigeration systems which are more efficient, experimental and theoretical investigations of many variations of plane wave thermoacoustic engines have been conducted. These studies include: different stack geometries (parallel plate,⁶ pin-array,¹⁰ spiral,¹¹ and other pore shapes¹²), stack location in the standing wave,^{8,9} stack pore size,^{8,12} resonator shape,⁸ and heat exchanger design.^{9,13,14} Generally available numerical routines have also been developed for evaluation of thermoacoustic systems.^{12,15}

An additional variation of thermoacoustic engines which has recently been considered is thermoacoustic engines with constant characteristic pore dimension in the fundamental radial mode of a cylindrical resonator. The relevant radial wave thermoacoustic equations have been derived, numerical code has been developed for evaluation of radial wave thermoacoustic engines, and theoretical predictions for radial wave prime movers and refrigerators have been made.¹⁶ However, previous to the present work, an operational radial wave thermoacoustic engine had not been constructed.

1.3 Overview of Dissertation

The focus of this research is the construction and evaluation of a radial wave thermoacoustic prime mover for purposes of testing theoretical predictions for the onset temperature (the temperature difference across the stack at which oscillations are sustained) and examining the behavior of the system in the presence of these thermally induced oscillations. In particular, attention is given to the expected reduction of nonlinear harmonic generation in the radial wave prime mover when compared to a plane wave prime mover.

An additional variation of the stack region which deserves consideration in plane and radial wave thermoacoustic engines is varying plate spacing or sloped stacks. The sloped stack is somewhat awkward from a construction standpoint in the plane wave case, but this difficulty disappears in the radial wave case, since a stack composed of vertical plates of constant thickness naturally leads to a varying plate spacing between consecutive plates. Therefore, in addition to an experimental study of radial wave thermoacoustic prime movers, a theoretical treatment of sloped stack plane and radial wave thermoacoustic systems will also be presented.

The core of this dissertation proceeds as follows. Chapter 2 reviews radial wave thermoacoustic theory and describes its numerical implementation. The radial wave prime mover design and construction is laid out in Chapter 3. Experimental results from the radial wave prime mover are compared with theoretical predictions in Chapter 4.

Sloped stack thermoacoustic theory and a description of its numerical implementation is presented in Chapter 5. Chapter 6 presents numerical results of the sloped stack theory for plane and radial wave thermoacoustic prime movers and refrigerators. The discussion is summarized and conclusions are presented in Chapter 7.

Chapter 2

Review of Radial Wave Thermoacoustic Theory

2.1 Introduction

One of the goals of this dissertation is to corroborate the existing radial wave thermoacoustic theory by comparing experimental results to theoretical predictions. Swift briefly mentioned thermoacoustics in the radial mode of a cylindrical resonator,⁶ and developed the radial mode thermoacoustic wave equation. Arnott *et al.*¹⁶ derived coupled first-order differential equations for pressure and specific acoustic impedance in the temperature gradient supporting stack, and pressure and impedance translation equations for open resonator sections and heat exchangers. Numerical implementation of these quantities allows for the prediction of the onset temperature difference, the temperature difference across the stack at which acoustic oscillations are induced.¹⁶ The rest of this chapter will review the radial wave thermoacoustic theory and its numerical implementation as described in References 12 and 16. The format of Ref. 12 will be closely followed.

2.2 Basic Equations and Assumptions

The following assumptions are made as a precursor to deriving the radial wave thermoacoustic equations. The “stack” is composed of stacks of washer shaped pieces (as in Fig. 2.1) so that the transverse coordinates in a pore are z and θ , while the longitudinal coordinate is r , as shown in Fig. 2.2. The ambient temperature in the stack is a function of r . The pore wall temperature is unaffected by temperature variations in the gas caused by an acoustic wave. Constant frequency pressure variations occur in the pore, and the pore walls are assumed rigid and non-porous.

The varying fluid quantities in a pore are pressure, particle velocity, temperature, entropy, and density. Due to the geometry of the pores, none of these quantities is dependent upon the θ coordinate. Assuming acoustic waves of radian frequency ω , approximations to first order are

$$p(r, t) = p_0 + p_1(r) \exp(-i\omega t), \quad (2.1)$$

$$\mathbf{v}(r, z, t) = [v_z(r, z)\hat{\mathbf{z}} + v_r(r, z)\hat{\mathbf{r}}] \exp(-i\omega t), \quad (2.2)$$

$$T(r, z, t) = T_0(r) + T_1(r, z) \exp(-i\omega t), \quad (2.3)$$

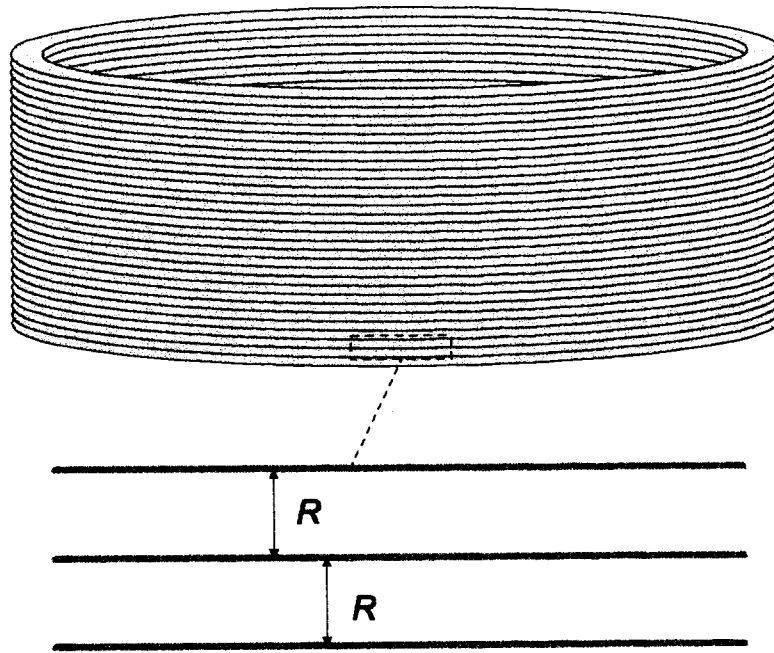


Figure 2.1: Stack design assumed for deriving radial wave thermoacoustic equations.

R denotes the vertical space between two adjacent plates.

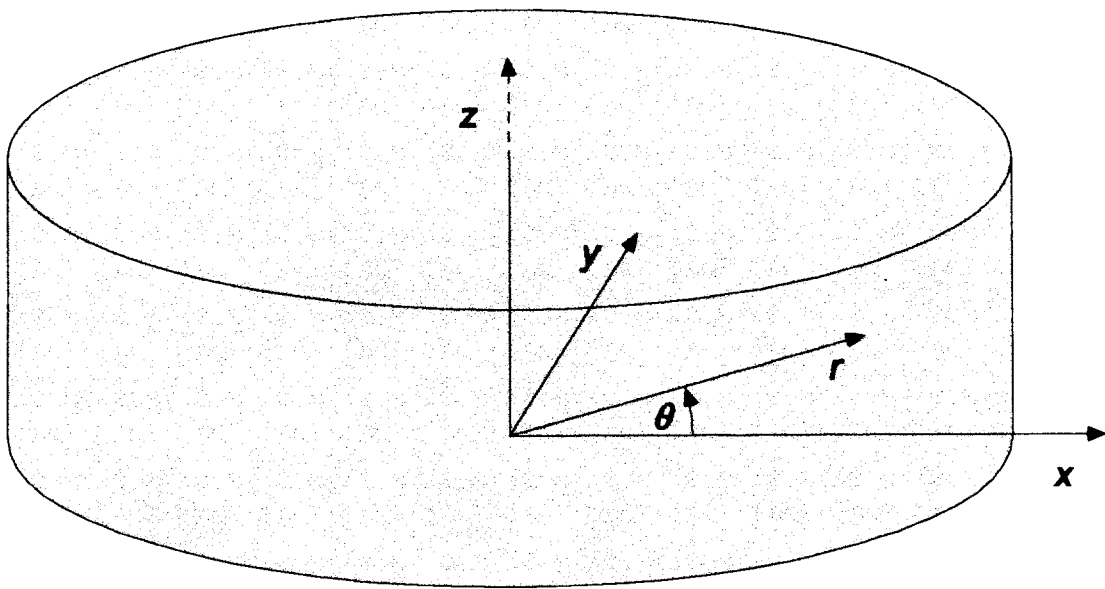


Figure 2.2: Radial geometry.

$$s(r, z, t) = s_0(r) + s_1(r, z) \exp(-i\omega t), \quad (2.4)$$

$$\rho(r, z, t) = \rho_0(r) + \rho_1(r, z) \exp(-i\omega t), \quad (2.5)$$

where subscript 0 indicates ambient values and subscript 1 indicates the acoustic (first order) values, and v_z and v_r are the transverse and radial components of the velocity, respectively.

The transverse variation of the fluid quantities is much greater than the radial variation due to boundary conditions at the pore walls, and the magnitude of the radial velocity is much greater than the transverse velocity. In addition, if the ratio of the plate spacing to the acoustic wavelength is small then the acoustic pressure may be considered to be a function of r only,¹⁷ as in Eq. 2.1. Assuming constant frequency waves, the approximate set of governing equations to first order are given by the r component of the Navier-Stokes equation,¹⁸ the continuity equation, the equations of state for density and entropy,¹⁹ and the heat transfer equation.²⁰

$$-i\omega\rho_0(r)v_r(r, z) = -\frac{\partial p_1(r)}{\partial r} + \eta\frac{\partial^2 v_r(r, z)}{\partial z^2}, \quad (2.6)$$

$$-i\omega\rho_1(r,z) + \rho_0(r)\frac{\partial v_z(r,z)}{\partial z} + \frac{1}{r}\frac{\partial}{\partial r}[r\rho_0(r)v_r(r,z)] = 0, \quad (2.7)$$

$$\rho_1(r,z) = -\rho_0(r)\beta T_1(r,z) + \frac{\gamma}{c^2} p_1(r), \quad (2.8)$$

$$s_1(r,z) = \frac{c_p}{T_0(r)} T_1(r,z) - \frac{\beta}{\rho_0(r)} p_1(r), \quad (2.9)$$

$$-i\omega c_p \rho_0(r) T_1(r,z) + c_p \rho_0(r) v_r(r,z) \frac{\partial T_0(r)}{\partial r} = -i\omega \beta T_0(r) p_1(r) + \kappa \frac{\partial^2 T_1(r,z)}{\partial z^2}, \quad (2.10)$$

where c_p is the isobaric heat capacity per unit mass, $\beta = -(\partial\rho/\partial T)_p / \rho_0(r)$ is the volume coefficient of expansion, γ is the ratio of specific heats, η is dynamic viscosity, κ is thermal conductivity, and c is sound speed. In the derivation of Eq. (2.10), which accounts for temperature gradient in the stack, the convective derivative is evaluated using Eq. (2.9) and the relation $\mathbf{v} \cdot \nabla s = c_p v_r(r,z) [dT_0(r)/dr] / T_0(r)$. Eqs. (2.6)-(2.10) are identical to the governing equations for plane wave prime movers except for the continuity equation, Eq. (2.7). The additional term in the radial case is due to the changing resonator cross-section.

2.3 Area Averaged Equation of Motion in a Pore

Assuming a solution to the Navier-Stokes equation of the form

$$v_r(r, z) = \frac{F(z, \lambda)}{i\omega\rho_0} \frac{dp_1(r)}{dr}, \quad (2.11)$$

where

$$\lambda = R\sqrt{\frac{\rho_0\omega}{\eta}} = \frac{R\sqrt{2}}{\delta_v}, \quad (2.12)$$

R is the plate spacing as shown in Fig. 2.1 (in general twice the pore area divided by the pore perimeter), and δ_v is the viscous boundary layer thickness; and plugging into Eq. (2.6) gives

$$F(z, \lambda) = 1 - \frac{R^2}{i\lambda^2} \frac{d^2 F(z, \lambda)}{dz^2}, \quad (2.13)$$

subject to the boundary condition that $F(z, \lambda) = 0$ at the pore walls. $F(z, \lambda)$ is the thermoviscous dissipation function. The cross-sectionally averaged form of Eq. (2.11) is given by¹²

$$v_r(r) = \overline{v_r(r,z)} = \frac{F(\lambda)}{i\omega\rho_0(r)} \frac{dp_1(r)}{dr}, \quad (2.14)$$

where $F(\lambda)$ is the area average of $F(z,\lambda)$ over the cross section of the pore. For a parallel plate arrangement, or a washer style radial stack, the thermoviscous dissipation function is given by

$$F(\lambda) = 1 - \frac{2}{\lambda\sqrt{-i}} \tanh\left[\frac{\lambda\sqrt{-i}}{2}\right]. \quad (2.15)$$

2.4 Area Averaged Equation of State in a Pore

Rearranging Eq. (2.10) and making use of Eq. (2.11) and the thermodynamic identity $T_0\beta^2/c_p = (\gamma - 1)/c^2$ yields

$$T_1(r,z) + \frac{R^2}{i\lambda_r^2} \frac{\partial^2 T_1(r,z)}{\partial z^2} = \frac{\gamma - 1}{\beta c^2 \rho_0(r)} p_1(r) - \frac{F(z,\lambda)}{\omega^2 \rho_0(r)} \frac{dT_0(r)}{dr} \frac{dp_1(r)}{dr} \quad (2.16)$$

for the fluctuating temperature in the pore, where

$$\lambda_T = R \sqrt{\frac{\rho_0 c_p \omega}{\kappa}} = \frac{R \sqrt{2}}{\delta_\kappa}, \quad (2.17)$$

and δ_κ is the thermal penetration depth. The solution to Eq. (2.16) for $T_1(r, z)$ is given by

$$T_1(r, z) = \frac{\gamma - 1}{\beta c^2 \rho_0(r)} F(z, \lambda_T) p_1(r) - \frac{[dT_0(r)/dr]}{\omega^2 \rho_0(r)} \left[\frac{F(z, \lambda_T) - N_{Pr} F(z, \lambda)}{1 - N_{Pr}} \right] \frac{dp_1(r)}{dr}, \quad (2.18)$$

where $N_{Pr} = \eta c_p / \kappa$ is the Prandtl number.

Inserting Eq. (2.18) into Eq. (2.8), the equation of state for the acoustic density fluctuation is

$$\rho_1(r, z) = \left[\gamma - (\gamma - 1) F(z, \lambda_T) \right] \frac{p_1(r)}{c^2} + \frac{\beta}{\omega^2} \frac{dT_0(r)}{dr} \left[\frac{F(z, \lambda_T) - N_{Pr} F(z, \lambda)}{1 - N_{Pr}} \right] \frac{dp_1(r)}{dr}. \quad (2.19)$$

Averaging Eq. (2.19) over a pore cross-section yields

$$\rho_1(r) = \left[\gamma - (\gamma - 1) F(\lambda_T) \right] \frac{p_1(r)}{c^2} + \frac{\beta}{\omega^2} \frac{dT_0(r)}{dr} \left[\frac{F(\lambda_T) - N_{Pr} F(\lambda)}{1 - N_{Pr}} \right] \frac{dp_1(r)}{dr}, \quad (2.20)$$

where $\rho_l(r)$, $F(\lambda)$, and $F(\lambda_T)$, are the area averages of $\rho_l(r, z)$, $F(z, \lambda)$, and $F(z, \lambda_T)$.

2.5 Acoustic Pressure Wave Equation

Averaging Eq. (2.7) over a pore cross-section produces

$$-i\omega\rho_l(r) + \rho_0(r)\frac{\partial v_r(r)}{\partial r} + \left[\frac{1}{r}\rho_0(r) - \beta\rho_0(r)\frac{dT_0(r)}{dr} \right] v_r(r) = 0. \quad (2.21)$$

Inserting Eqs. (2.14) and (2.20) for $v_r(r)$ and $\rho_l(r)$ into Eq. (2.21) yields

$$\frac{\rho_0(r)}{F(\lambda)} \frac{\partial}{\partial r} \left[\frac{F(\lambda)}{\rho_0(r)} \frac{dp_1(r)}{dr} \right] + \frac{1}{r} \frac{dp_1(r)}{dr} + 2\alpha(\lambda, \lambda_T) \frac{dp_1(r)}{dr} + k^2(\lambda, \lambda_T) = 0, \quad (2.22)$$

where

$$\alpha(\lambda, \lambda_T) = \frac{\beta}{2} \frac{dT_0(r)}{dr} \left[\frac{F(\lambda_T)/F(\lambda) - 1}{1 - N_{pr}} \right], \quad (2.23)$$

and

$$k^2(\lambda, \lambda_T) = \frac{1}{F(\lambda)} \frac{\omega^2}{c^2} [\gamma - (\gamma - 1)F(\lambda_T)]. \quad (2.24)$$

Eq. (2.22) is the wave equation for the acoustic pressure. Notice that the second term provides the only difference between Eq. (2.22) and the wave equation in the plane geometry.¹²

2.6 First Order Impedance Equation

For purposes of integration, Eq. (2.22) can be rewritten as two first order differential equations for the total acoustic pressure as a function of total particle velocity and for the impedance as a function of position. Define as a pore the space between two plates. Let n be the total number of pores in the section, $A_{res}(r)$ the resonator cross-sectional area at r , $A_p(r)$ the cross-sectional area of a pore at r , $V_{rb}(r)$ the bulk velocity at r , and Ω the porosity or the ratio of open area at r to $A_{res}(r)$. Volume velocity is $A_{res}(r)V_{rb}(r) = nA_p(r)v_r(r)$, but $\Omega = nA_p(r)/A_{res}(r)$; therefore, $v_r(r) = V_{rb}(r)/\Omega$. Using this result in Eq. (2.14) yields

$$\frac{dp_1(r)}{dr} = ik(\lambda, \lambda_T)Z_{int}(r)V_{rb}(r), \quad (2.25)$$

where the intrinsic impedance of the stack is

$$Z_{\text{int}}(r) = \frac{\rho_0 \omega}{\Omega(r) F(\lambda) k(\lambda, \lambda_T)} \quad (2.26)$$

Defining the specific acoustic impedance as $Z(r) = p_1(r)/V_{rb}(r)$, and inserting Eq. (2.25) into Eq. (2.22) with $A_{\text{res}}(r) = 2\pi r h$, where h is the resonator height, produces the following first order equation for $Z(r)$

$$\frac{dZ(r)}{dr} = ik(\lambda, \lambda_T) Z_{\text{int}}(r) \left[1 - \frac{Z^2(r)}{Z_{\text{int}}^2(r)} \right] + \left\{ 2\alpha(\lambda, \lambda_T) + \frac{1}{r} \right\} Z(r). \quad (2.27)$$

2.7 Specific Acoustic Impedance and Pressure Translation Theorems

For open resonator and heat exchanger sections in which there are no ambient temperature gradients, it is not necessary to use Eq. (2.27). Rather, impedance and pressure translation equations, which allow simple calculation of values at a location $r-d$ when the value at r is known, are preferable. The general, linearly independent solution to the plane wave equation for complex pressure and velocity is a combination of sines and cosines. For the radial wave equation, however, the solution is a combination of Bessel functions of the first and second kinds, which may be combined to form Hankel functions.²¹ The pressure and impedance translations may be found for plane waves in

Ref. 12 and for radial waves in Ref. 16. The radial wave translation equation for pressure is

$$p_1(r-d) = p_1(r) \frac{\pi k r i}{4} \left\{ H_1^{(1)}[kr] H_0^{(2)}[k(r-d)] - H_1^{(2)}[kr] H_0^{(1)}[k(r-d)] \right. \\ \left. - i \frac{Z_{\text{int}}}{Z(r)} \left(H_0^{(2)}[kr] H_0^{(1)}[k(r-d)] - H_0^{(1)}[kr] H_0^{(2)}[k(r-d)] \right) \right\}. \quad (2.28)$$

The translation equation for specific acoustic impedance is

$$Z(r-d) = \frac{Z_{\text{int}} \left\{ Z(r) \left(H_1^{(1)}[kr] H_0^{(2)}[k(r-d)] - H_1^{(2)}[kr] H_0^{(1)}[k(r-d)] \right) \right. \\ \left. - i Z_{\text{int}} \left(H_0^{(2)}[kr] H_0^{(1)}[k(r-d)] - H_0^{(1)}[kr] H_0^{(2)}[k(r-d)] \right) \right\}}{\left\{ Z_{\text{int}} \left(H_1^{(1)}[k(r-d)] H_0^{(2)}[kr] - H_1^{(2)}[k(r-d)] H_0^{(1)}[kr] \right) \right. \\ \left. - i Z(r) \left(H_1^{(1)}[k(r-d)] H_1^{(2)}[kr] - H_1^{(2)}[k(r-d)] H_1^{(1)}[kr] \right) \right\}}. \quad (2.29)$$

In Eqs. (2.28) and (2.29), $H_m^{(j)}[x]$ are Hankel functions of order m , type j , and argument x .

2.8 Numerical Determination of Onset Temperature

For a thermoacoustic system similar to that of Fig. 2.3, having elements with specified dimensions, inner and outer temperatures, and plate spacings in the case of stack and heat exchanger sections, the onset temperature or the temperature difference

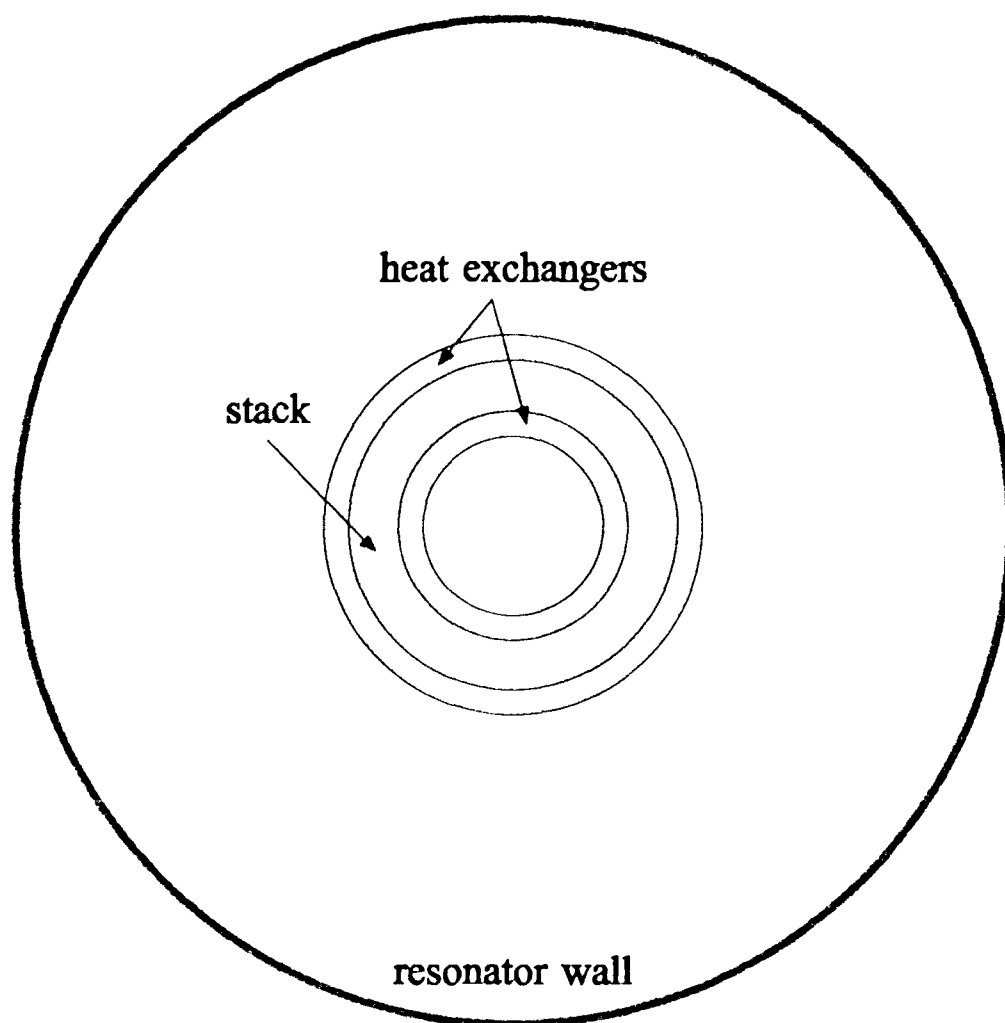


Figure 2.3: Schematic of a radial wave prime mover for describing the numerical implementation of the radial thermoacoustic theory.

across the stack at which oscillations will be spontaneously generated can be numerically calculated. The ambient temperature gradient across the stack, derived from the simple heat conduction equation, is given by

$$\frac{dT_0(r)}{dr} = \frac{T_{out} - T_{in}}{r \ln[r_{out}/r_{in}]}, \quad (2.30)$$

where subscript *out* refers to the radial outer edge of the stack and subscript *in* refers to the radial inner edge of the stack.

The onset temperature difference, ΔT , and resonant frequency, f_0 , are determined by numerically searching for values of ΔT and f_0 which produce the same values for the calculated impedance looking to the right at some position with that computed looking to the left. Denote Z_- and Z_+ as the impedance at the inner radius of the inner heat exchanger calculated from the center of the resonator and the outer wall of the resonator, respectively. The pressure and impedance at r for a known acoustic pressure at the center of the resonator are

$$p_1(r) = p_1(0)J_0(kr), \quad (2.31)$$

and

$$Z(r) = -iZ_{int} \frac{J_0(kr)}{J_1(kr)}. \quad (2.32)$$

Eqs. (2.31) and (2.32) can be derived by setting $r = 0$, $d = -r$, and $Z(0) = \infty$, in Eqs. (2.28) and (2.29). Z_{int} is calculated directly from Eq. (2.32), using the appropriate inner radius of the inner heat exchanger.

Z_{+} is computed by beginning with the impedance at the outer wall of the resonator. The impedance at the resonator wall is the boundary layer impedance, denoted by Z_{bl} , and can be shown to be²²

$$Z_{bl} = -\frac{\rho_0 c^2}{\gamma - 1} \sqrt{\frac{\rho_0 c_P}{i\omega\kappa}} \frac{J_0[(1+i)a/\delta_\kappa]}{J_1[(1+i)a/\delta_\kappa]} \approx \frac{\rho_0 c^2}{\gamma - 1} \sqrt{\frac{\rho_0 c_P}{i\omega\kappa}}, \quad (2.33)$$

where a is the resonator radius. The approximation in Eq. (2.33) is valid for $a \gg \delta_\kappa$, which is always satisfied in the open resonator section of a thermoacoustic system. With Z_{bl} at the resonator wall known, the impedance at the outer edge of the outer heat exchanger is computed using Eq. (2.29). This value of impedance is used again in Eq. (2.29), with k and Z_{int} appropriate for the heat exchanger, to determine the impedance at the interface between the outer heat exchanger and the stack. With this impedance value used as a boundary condition, Eq. (2.27) is numerically integrated using a fourth order Runge-Kutta algorithm to determine the impedance at the interface between the stack

and the inner heat exchanger. Finally, Eq. (2.29) is used again to determine Z_+ , the impedance at the inside of the inner heat exchanger. The process is repeated for different values of ΔT and f_0 until $Z_- = Z_+$.

2.9 The Importance of Onset Temperature

DeltaT (ΔT) is an important quantity in thermoacoustic engines for several reasons. The total power generated by a prime mover is the power generated by the temperature gradient supporting stack (which is proportional to ΔT) minus the thermal and viscous losses in the stack. Arnott *et al.*²³ showed that a prime mover will begin to make sound when the total power generated in the prime mover overcomes other losses in the heat exchangers and the resonator. Therefore, ΔT is proportional to the ratio of the acoustic power dissipated in the entire system (including the stack, heat exchangers, and any external load) to the acoustic power generated by the stack. Secondly, ΔT measurements are relatively easy to make, so that predictions and measurements can be compared to determine whether or not the numerical models making the predictions are accurate, giving added assurance that predictions for refrigerators will be correct.

Chapter 3

Radial Wave Thermoacoustic Prime Mover Design

3.1 Introduction

Although, as seen in the previous chapter, theoretical work on radial wave thermoacoustics has been considered, a radial wave thermoacoustic engine had not been built prior to this work. To test the radial wave thermoacoustic theory, an operational radial wave prime mover was designed and constructed. A physical description of the working prime mover and measurements will be presented in this chapter. In addition, two *non-operational* initial designs will be described.

3.2 Initial Design I: Small Aluminum/Steel Resonator

The present radial wave prime mover has evolved over time. A schematic of the original design is shown in Fig. 3.1, and dimensions of its components are listed in Table 3.1. Initially, the thermoacoustic elements were housed in a cylindrical resonator 10.2 cm high and 30.5 cm in diameter. The outer ring of the resonator was 2.54 cm thick in the radial direction and was made of aluminum. The top and bottom plates were 0.95 cm thick stainless steel with 0.5 cm deep grooves cut at the location of the stack to

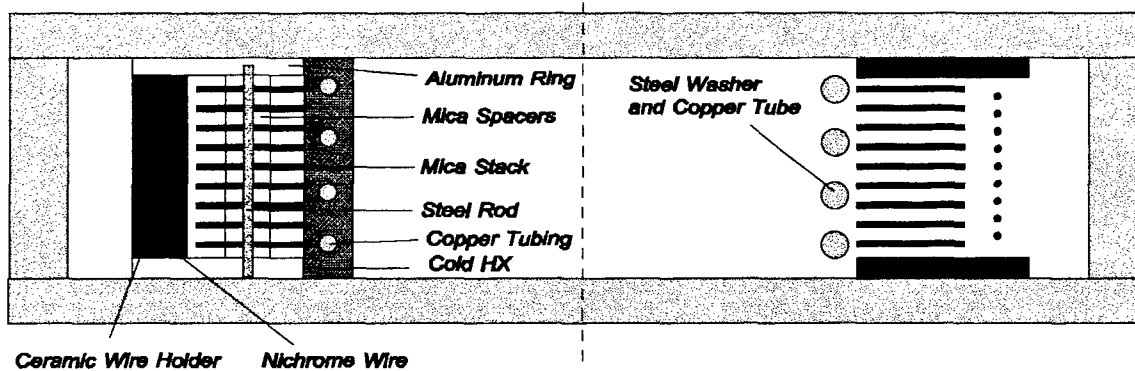


Figure 3.1: Original radial wave thermoacoustic prime mover design. Left of the center line shows a cross-section at one of the wire supports and shows a cold heat exchanger plate. Right of the center line shows a cross-section away from the wire supports and shows the open space in the cold heat exchanger.

	RADIAL LENGTH (cm)	R (cm)	POROSITY	MATERIAL
HOT TUBE NEAR TUBE WALL	2.0	10.16	1.00	—
HOT HEAT EXCHANGER	0.1	1.0	0.90	copper
STACK	1.25	0.038	0.60	mica
COLD HEAT EXCHANGER	1.27	0.081	0.25	copper
COLD TUBE NEAR TUBE CENTER	10.62	10.16	1.00	—

Table 3.1: Description of the original small radial wave prime mover. R is the plate spacing in heat exchangers and the stack, and the resonator height in open tube sections

reduce thermal conduction across the stack casing (the plates). The resonator was sealed using high temperature lubricated O-rings between the outer ring and the top and bottom plates (placed in grooves machined into the outer ring). The intended operating fluid was a 60% Helium, 40% Argon mixture at a pressure of 1.8 atm. This gas mixture was chosen due to its low Prandtl number, a quality associated with ideal thermoacoustic working fluids.^{6,7,9} The corresponding frequency of operation was about 1.8 kHz. The stack and heat exchangers were located *outside* the pressure node, forcing the outer side of the stack to be heated and the inner side of the stack to be held at ambient temperature, since the hot side must always face the nearest pressure antinode.¹⁶

The stack was composed of washer shaped silicon bonded mica paper pieces fabricated by Micatron Incorporated. A schematic of a single stack element is shown in Fig. 3.2. The inner diameter of the pieces was 23.78 cm, the outer diameter 26.28 cm, and the vertical thickness was 0.015 cm. The solid dots in Fig. 3.2 are eight equally spaced holes which allowed the stack pieces to be fed onto stainless steel rods with washers between to maintain the spacing. A total of 183 of these mica plates stacked on top of each other comprised the 10.2 cm tall stack. Spacing between the pieces was maintained by eight equally spaced smaller mica washers (shown in Fig. 3.3), 0.64 cm in diameter and 0.038 cm thick, placed over 3 mm diameter stainless steel rods. The mica was chosen for its high heat tolerance (up to 773 K) and its very low thermal conductivity of 0.163 W/(m*K) at a temperature of 293 K. Two stainless steel pieces,

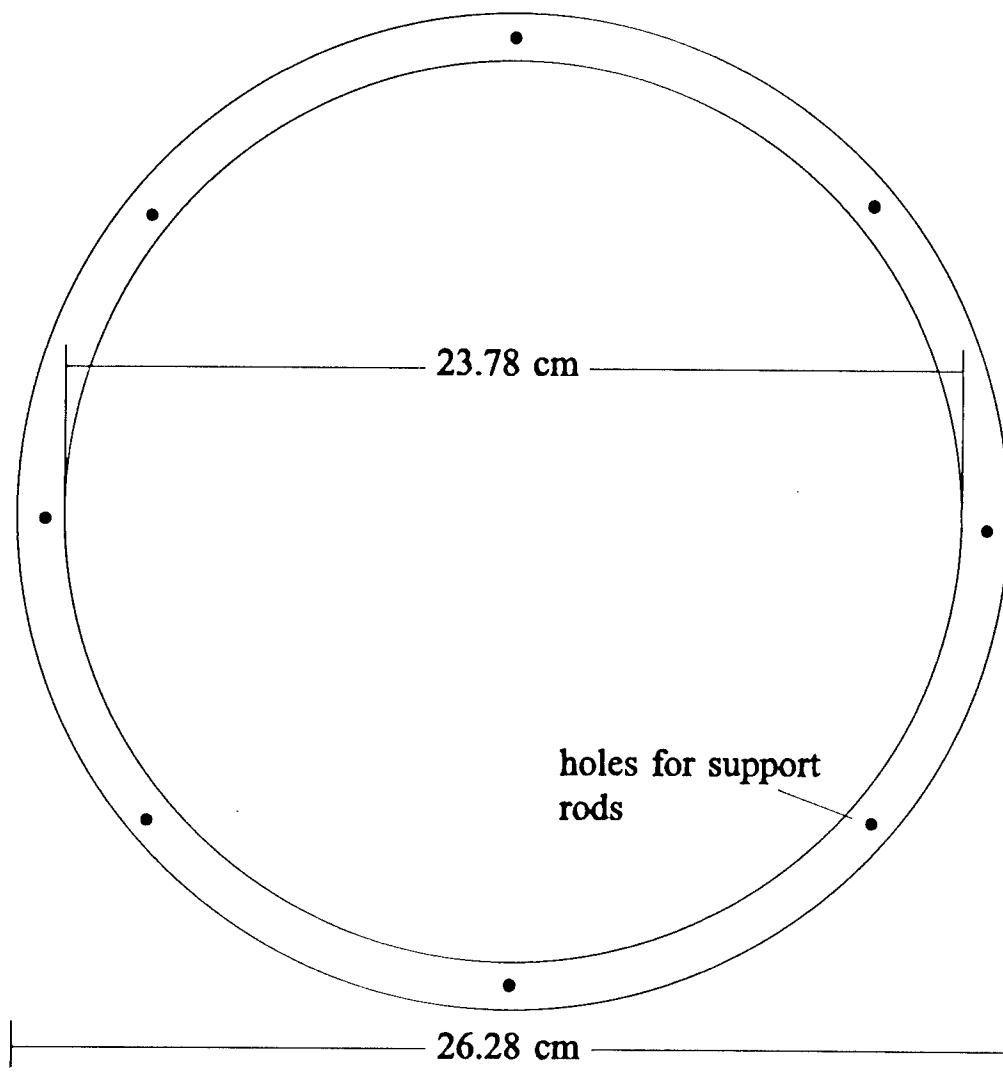


Figure 3.2: A single element of the radial wave “washer” style stack. The element is composed of silicon bonded mica paper with a thickness of 0.01524 cm.

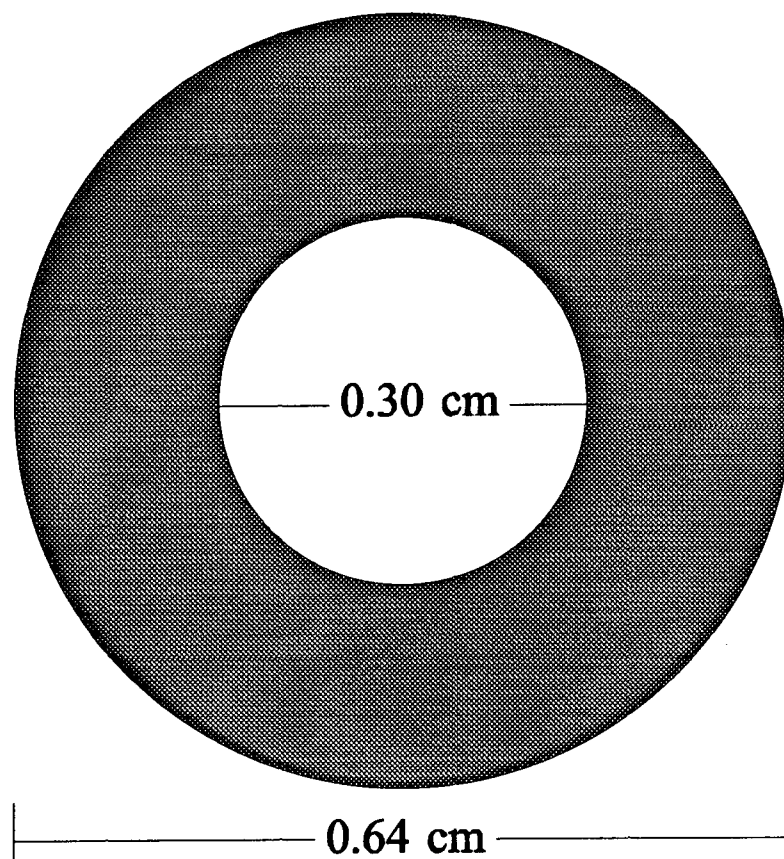


Figure 3.3: Mica spacer used to maintain proper spacing in the radial stack.

with the same radial dimensions as the stack pieces and a thickness of 0.5 mm, were placed on top and bottom of the stack to provide some rigidity. Upon completion of the stack, it was noticed that there were not enough spacer washers to maintain a proper plate spacing in the stack, so 0.038 cm diameter high temperature Teflon thread was placed between spacer locations (thus increasing the total number of supports to sixteen) to help maintain the proper spacing between successive stack elements.

The finned cold (inner) heat exchanger was constructed by Pat Arnott, Robert Abbott, and Michael Ossofsky at the University of Nevada at Reno. It was composed of four standard ¼ in. copper tubes bent into circles, with copper plates (each having four pre-punched holes to fit snugly over the tubing) fed onto the tubing. Steel washers were placed between the copper plates to maintain the plate spacing. The individual copper plates were 10 cm tall, 1.27 cm in the radial direction, and 0.762 mm thick. A diagram of a single heat exchanger plate is shown in Fig. 3.4. The washer spacers were also 0.762 mm thick. Plumbing was attached to the copper tubes to allow water to be circulated, thus cooling the gas at the inner face of the stack.

The hot side was heated by 8.5 meters of 80% Nickel, 20% Chromium resistively heated wire. The wire diameter was 1 mm. The heater design was chosen for the experimental convenience of quick heating.⁹ Ceramic rods were used to hold the wire in place. The heater was capable of dissipating 3 kW of electric power.

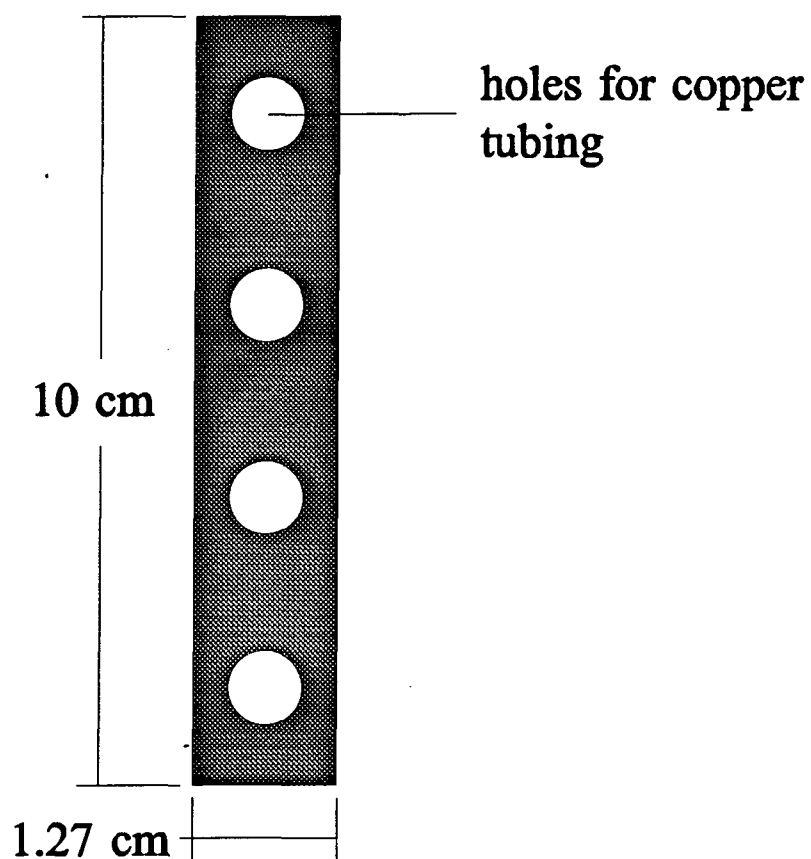


Figure 3.4: A single element of the cold heat exchanger. The plate material is copper, and the plate thickness is 0.762 mm. The holes provide a snug fit for standard $\frac{1}{4}$ inch copper tubing.

Prior to onset of oscillations, the thermoacoustic gain as a function of temperature difference can be measured by monitoring the quality factor Q (the resonant frequency of the system divided by the difference between the half-power point frequencies).^{24,25,26} In a thermoacoustic engine, as the temperature difference across the stack increases, Q also increases, until it approaches infinity. When Q becomes infinite, the system is in onset and spontaneously begins to produce sound. For the original system of Fig. 3.1, Q of the empty resonator (empty in the sense that no thermoacoustic elements were installed, though electrical leads and plumbing for these elements were present) at the fundamental radial mode of oscillation was 730, compared to a predicted value of 900. With all of the thermoacoustic components installed, the Q was measured to be 29.5, compared to a predicted value of 35. Discrepancies between experiment and theory were due to the fact that plumbing and electrical leads were unaccounted for in the numerical calculations, but were present in the experiments. When the Q as a function of the temperature difference across the stack was monitored, the Q of the resonator increased as the temperature difference across the stack increased, as expected. However, the cold heat exchanger could not remove enough heat to establish the necessary temperature difference across the stack to produce spontaneous oscillations. The predicted temperature difference needed to produce spontaneous oscillations was 251 K for the Helium-Argon mixture at a pressure of 1.8 atm. In the experiment, the cold side was held at ambient temperature (293 K) until the hot side

reached about 400 K. At this point, the cold heat exchanger could no longer keep up with the heat being transported across the stack, and a temperature difference of about 100 C was maintained as both sides of the stack increased in temperature. The Q increased while the cold side remained near ambient temperature, but as the cold side began to increase in temperature, the stack plate spacing became non-optimized, and the Q decreased.

3.3 Initial Design II: Large Concrete/Plywood Resonator

It was decided that the best option to produce an operational prime mover would be to increase the size of the system, so that the radial dimension (radius) was of the same order as the length of typical resonators in plane wave systems, thus reducing the operating frequency and in turn the losses in the system. Looking at the general equations for work flow in a thermoacoustic engine,^{6,12} it is not obvious that a lower frequency leads to a reduction in the losses. However, when examined under the short-stack approximation where the gain and loss terms have been separated as in Eq. 18 of Ref. 16 and Eq. 3 of Ref. 23, it is seen that both the losses due to dissipation of potential and kinetic energy are directly proportional to the frequency of oscillation, while the gain term is dependent upon frequency only through the thermoviscous dissipation function.

Rather than starting from scratch, the original stack and cold heat exchanger were incorporated into the new design. Arnott's numerical routine¹⁶ was used to optimize the radial dimension of a resonator such that the onset temperature was a

minimum using the existing stack in air at atmospheric pressure (air was chosen rather than the 60% He - 40% Ar mixture due to concerns over pressurizing and depressurizing a cavity with such a large flat surface area). The height of the resonator was held at 10.2 cm, just as in the small system. Prior to constructing this engine, a plane wave model was constructed to make sure that the relative size of the elements in the radial system which was being considered did not have any inherent problems. In the next chapter, results from the plane wave model and the final radial system will be compared, particularly looking at the generation of higher harmonics.

3.3.1 *Plane wave model*

Fig. 3.5 shows a schematic of the plane wave model which was constructed, and Table 3.2 gives its specific dimensions. The system is very similar to that described in Belcher's dissertation.⁹ The length of the stack was 1.25 cm and the resonant frequency 280 Hz (which required a tube length of 61 cm). These quantities were chosen to be the same as the radial length of the stack and the resonant frequency in the proposed radial system. Heat exchangers were copper fins mounted in solid blocks of copper, the hot one heated electrically and the cold one cooled with ambient water flow. The stack material was a ceramic composite square pore material having 400 pores per square inch manufactured by Corning,²⁷ previously described in Ref. 28. The tube diameter was 8.5 cm. The location of the stack was determined by numerically choosing the location which produced the lowest onset temperature.

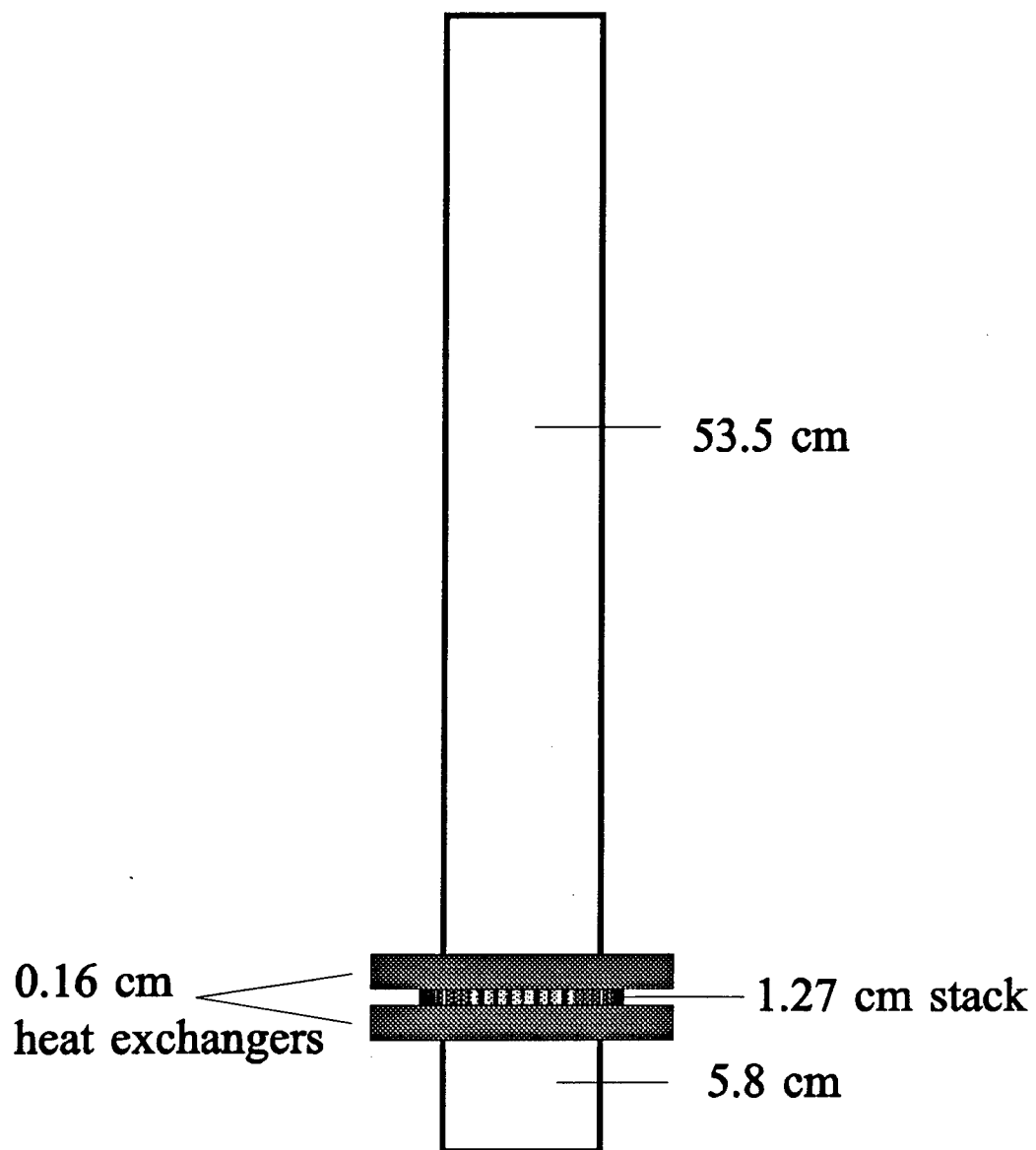


Figure 3.5: Plane wave model with dimensions similar to the proposed large radial wave thermoacoustic prime mover. All lengths shown are in the vertical direction. The tube diameter is 8.5 cm.

	LENGTH (cm)	R (cm)	POROSITY	MATERIAL
HOT TUBE	5.8	4.22	1.00	----
HOT HEAT EXCHANGER	0.16	0.051	0.50	copper
STACK	1.27	0.057	0.81	celcor
COLD HEAT EXCHANGER	0.16	0.051	0.50	copper
COLD TUBE	53.5	4.22	1.00	----

Table 3.2: Description of the plane wave model with similar dimensions to the proposed large radial wave prime mover. R is the plate spacing in heat exchangers and the stack, and the resonator radius in open tube sections.

The predicted onset temperature difference across the stack was 99 K. Experiment produced an onset temperature difference of 103 K. This good agreement between experiment and theory led to the expectation that there was nothing inherent in the dimensions of the proposed radial engine which should hinder it from working, and construction of the large radial prime mover was initiated.

3.3.2 Radial Wave Model

As mentioned previously, the cold heat exchanger and stack from the small radial prime mover were incorporated into the design of the new model. In the new design, however, the stack and heat exchangers were located *inside* the pressure node. This required that the hot heat exchanger be located on the inside of the stack and the cold heat exchanger be located outside the stack, since the hot side must always face the nearest pressure antinode. The former cold heat exchanger in the small system was converted into a hot heat exchanger by feeding 80% Nickel, 20% Chromium resistively heated wire through ceramic bead insulators (hole fish spine ceramic beads from Omega Engineering, Inc.). The beaded wire was then inserted into the copper tubing in the heat exchanger and electric leads were attached. A new cold heat exchanger identical to the former cold heat exchanger was constructed at the University of Nevada at Reno and fitted to the outside of the stack.

The diameter of the new resonator was 148.6 cm, and was chosen such that the existing stack was optimized for operation in air at atmospheric pressure. It was

constructed of cement (bottom and outer ring) and a double layer of 3/4 in. plywood (top). Q measurements of the empty resonator were significantly lower than predicted due to leaks. A test of the thermoacoustic capability of the new resonator with the thermoacoustic elements in place showed that increasing the temperature difference across the stack, even at large temperature differences, had little effect upon the Q of the resonance. Numerous attempts to seal the resonator with polyurethane, water-proofing paint, and rubber cement were ineffective, and it was determined that a new sealed steel resonator would be necessary.

3.4 Final Design

A schematic of the steel resonator which would serve as the final housing for the operational radial wave thermoacoustic prime mover is shown in Fig. 3.6. The pieces were manufactured by O'Neal Steel²⁹ and machined by Williams Machine Works, Inc.³⁰ The inner diameter of piece #3 is 148.6 cm. The diameter of the hole in piece #2 is 35.6 cm, and allows access to the thermoacoustic elements. All seals are made with o-rings lubricated with SIL-GLYDE lubricating compound. The thickness of piece #2 is 2.54 cm, while the radial thickness of piece #3 is 3.8 cm. The caps, piece #1, are composed of stainless steel, and have a groove cut at the location of the stack to decrease thermal conduction of heat across the stack region of the resonator. When the caps, pieces #1, are placed into the holes of pieces #2, the inner face of the cap is flush with the inner face of the larger piece #2. The height of piece #3, and thus the inner height of the resonator,

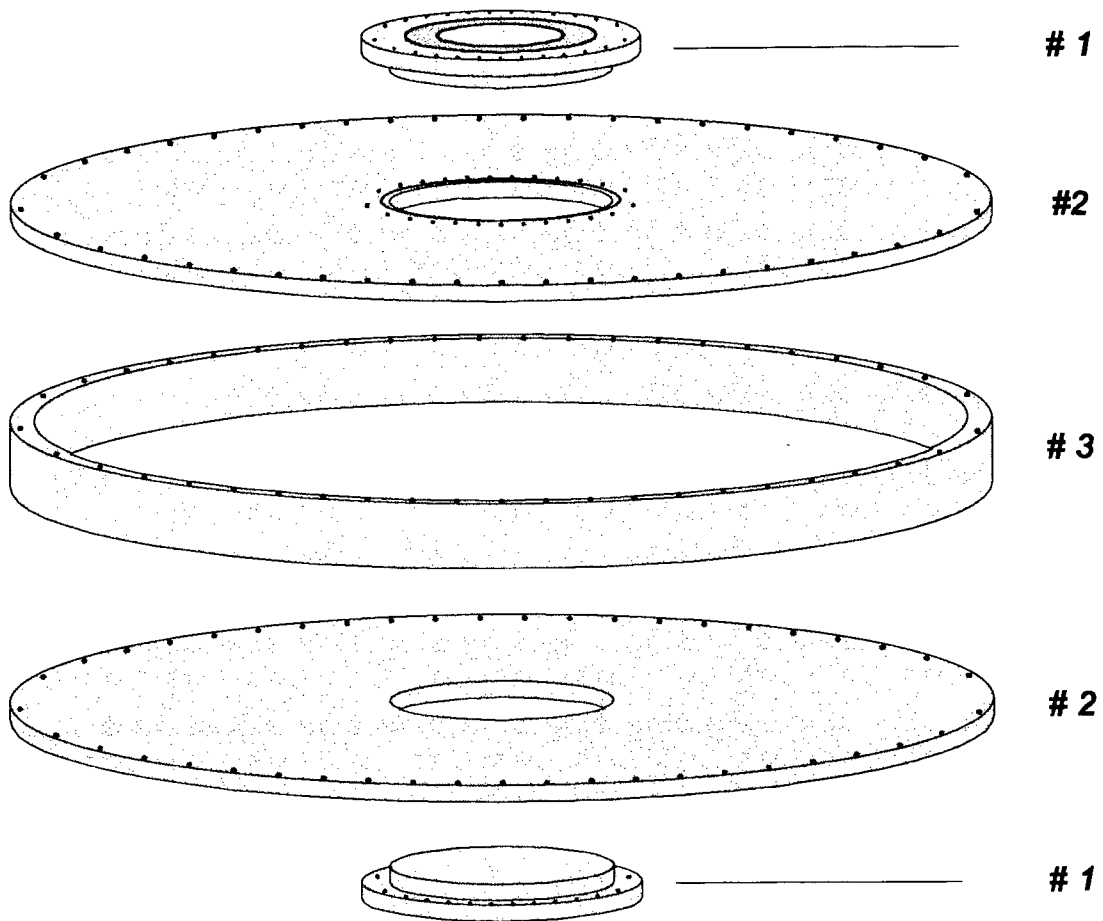


Figure 3.6: Unassembled view of the resonator used for the large radial wave thermoacoustic prime mover. Pieces #1 are stainless steel caps which allow access to the inner thermoacoustic elements. Pieces #2 and #3 are plain carbon steel.

is 10.2 cm. The assembled resonator has a mass of about 1360 kg. It should be noted that measures can be taken to significantly reduce the mass of the resonator for later applications. However, the current model was convenient for testing.

Fig. 3.7 shows the completed radial wave prime mover. For size comparison, a meter stick has been laid across the resonator. Some of the details of the system can be seen in this figure, including: the electrical heating leads (on the right side), the cooling fluid inlet and outlet (on the left side next to the cooler), and the groove in the center cap to reduce thermal conduction across the stack. The system has been made portable by placing it on a cart with four heavy duty casters.

Fig. 3.8 shows the thermoacoustic elements inside the resonator. A 30 cm ruler is also included in the photo for comparison. The o-ring which seals the cap to the resonator is seen just inside the cap bolt holes. The inner heat exchanger is heated electrically, and the outer heat exchanger is cooled by circulating water. The construction of the stack and heat exchangers has been described in previous sections. Traces of the plumbing leading into the cold heat exchanger can be seen at the left side of Fig. 3.8. The hot heat exchanger is heated electrically and is capable of delivering 1000 Watts of power. The stack is sandwiched between the heat exchangers as shown in Fig. 3.8. It is composed of washer shaped pieces of silicon bonded mica paper, described previously. An image of a single stack element is shown in Fig. 3.9.

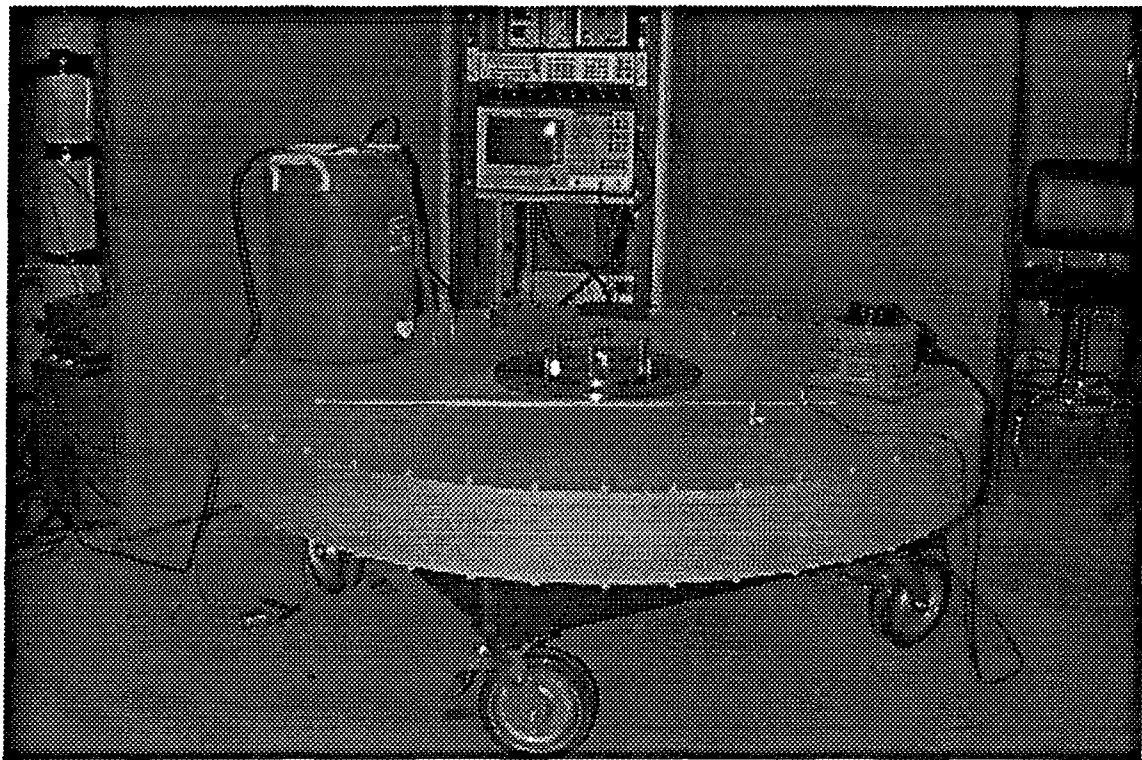


Figure 3.7: The finished and operational radial wave thermoacoustic prime mover.

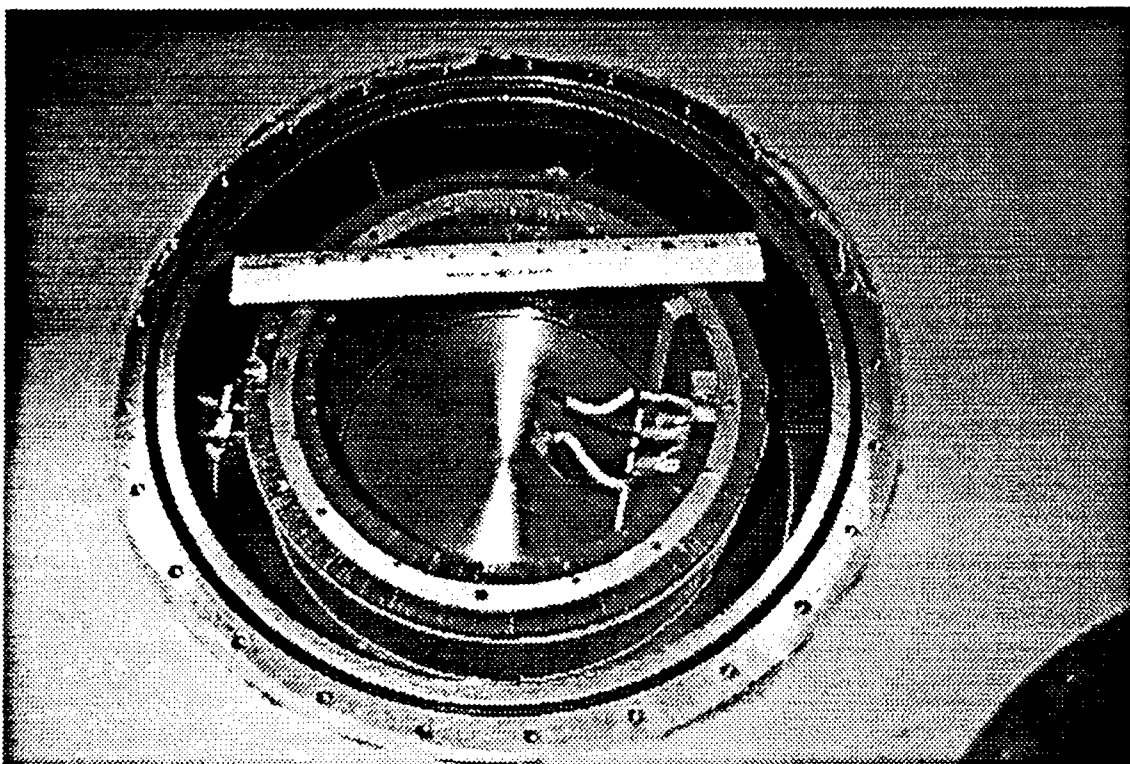


Figure 3.8: Thermoacoustic elements inside the resonator. The center cap fits flush against the inner elements (heat exchangers and stack).

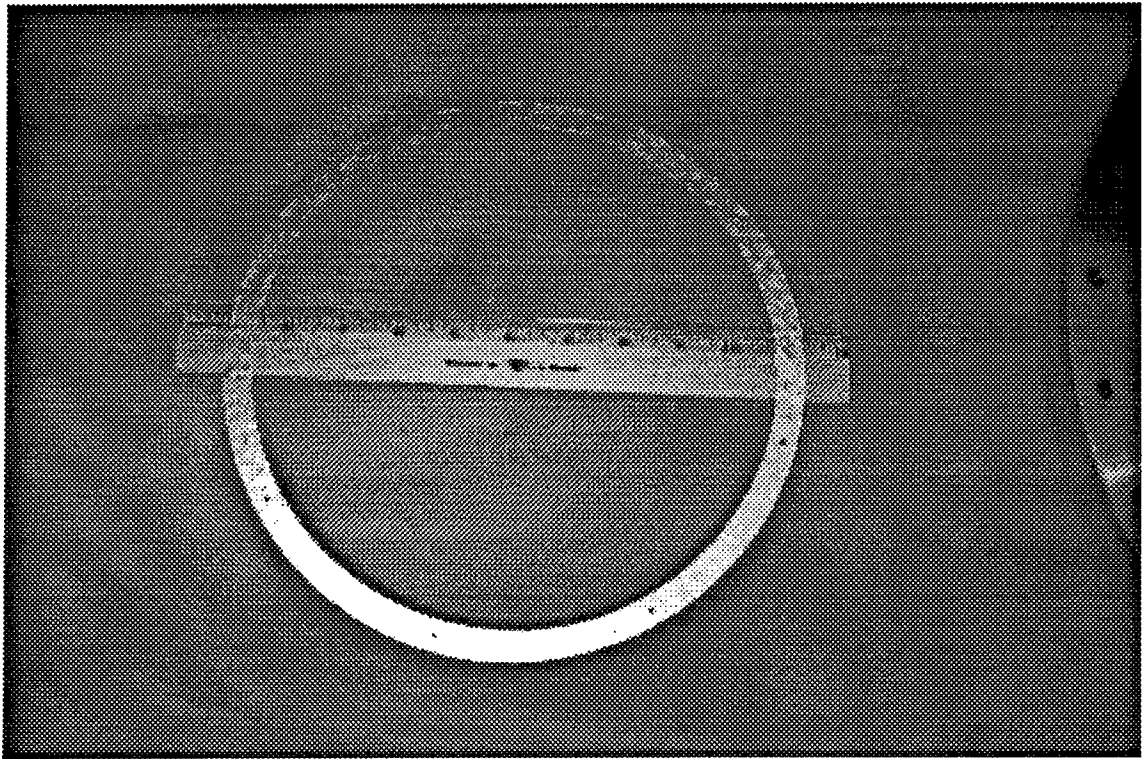


Figure 3.9: A single element of the stack. The stack material is a silicon bonded mica paper.

A line drawing of the entire system³¹ is shown in Fig. 3.10, and dimensions of the individual components are given in Table 3.3. The microphone used for detection of the acoustic wave, an Endevco 8510B-5 piezo-resistive microphone used in conjunction with an Endevco 106 signal conditioner and an Endevco 109 power supply, is located at a pressure antinode next to the outer wall of the resonator. It would be preferable to have the microphone at the center of the resonator, since the highest sound pressure levels occur there, but due to the high temperatures it is necessary to leave it at the outer wall and extrapolate values to the center. All inlets to the resonator other than the microphone (plumbing, heating, pressure valve, and thermocouples) are located at the pressure node in order to reduce losses due to leaks at these junctures. Electric leads are routed through the top by threading two 8-32 screws through nylon insulating bolts which are screwed into threaded holes in the top of the resonator. Leaks are minimized by wrapping all threads with Teflon tape. Teflon tape was also used on all plumbing threads and the pressure valve. Leaks through thermocouple leads, both around the insulation and through the insulation, are eliminated by stripping pieces from the insulation, feeding the stripped section through a pre-drilled brass thumb screw, and sealing the hole in the thumb screw with STYCAST 1266 epoxy from Grace Manufacturing. This epoxy flows in as a low viscosity liquid, completely surrounding the stripped wires, and hardens over a 24 hour period. The thumb screws are then placed into threaded holes in the top of the resonator.

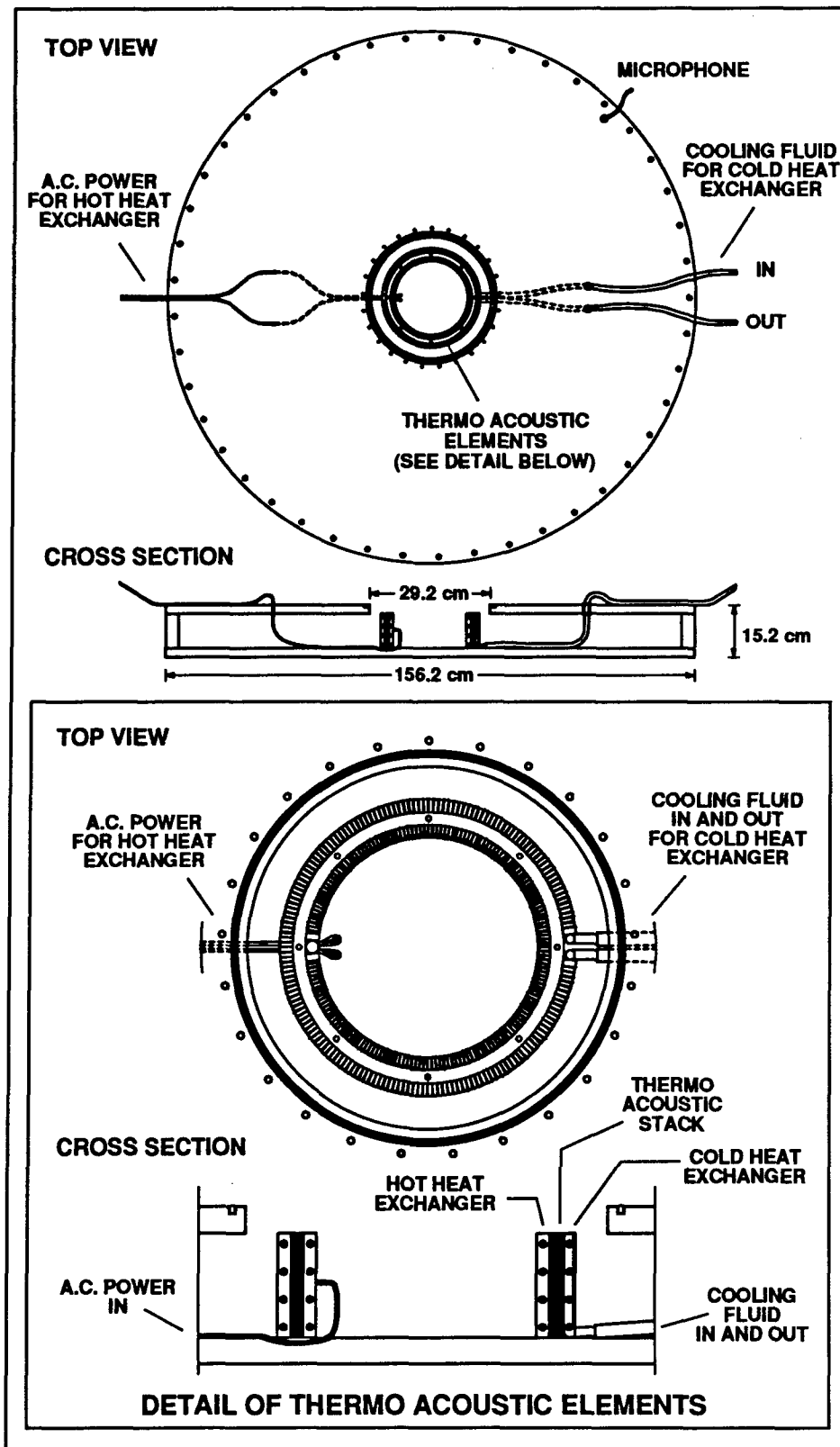


Figure 3.10: Line drawing of the radial wave thermoacoustic prime mover.

	RADIAL LENGTH (cm)	R (cm)	POROSITY	MATERIAL
HOT TUBE NEAR TUBE CENTER	10.5	10.16	1.00	---
HOT HEAT EXCHANGER	1.31	0.089	0.32	copper
STACK	1.25	0.040	0.70	mica
COLD HEAT EXCHANGER	1.31	0.089	0.32	copper
COLD TUBE NEAR TUBE WALL	59.9	10.16	1.00	---

Table 3.3: Description of the large operational radial wave prime mover. R is the plate spacing in heat exchangers and the stack, and the resonator height in open tube sections

3.5 Experimental Measurements and Associated Errors

All temperature measurements described in this chapter were taken with an Omega HH82 digital thermometer and type K thermocouples with a precision of ± 1 K. The thermocouples were placed between plates of the heat exchangers and coupled to the heat exchangers using OMEGATHERM "201" high temperature - high thermal conductivity paste. The onset temperature is taken when the sound pressure level, initiated by a small tap on the resonator, increases without decaying. The error associated with this measurement is estimated to be ± 2 K (the difference between the earliest onset temperature after tapping and the onset temperature without tapping), so that the total error in temperature measurements is ± 3 K. Section 4.2 in the following chapter discusses a peculiar behavior in the radial prime mover, oscillation into and out of onset.

Sound pressure level measurements were made using an Endevco 8510B-5 piezo-resistive microphone located near the outer wall of the resonator in conjunction with an Endevco 109 power supply and an Endevco 106 conditioner. The microphone was calibrated using a Bruel & Kjaer pistonphone. The microphone output was sent to a Hewlett Packard 35665A dynamic signal analyzer to view the SPL as a function of frequency. The error associated with SPL measurements is less than 0.2 dB, and the frequency step size is 0.25 Hz.

Chapter 4

Radial Wave Thermoacoustic Prime Mover Experimental Results and Comparison to Theory

4.1 Introduction

There are several questions which need to be answered with results from the radial wave prime mover described in the previous chapter. The first has to do with theoretical predictions; can we predict the behavior of radial wave prime movers using radial wave thermoacoustic theory? The second has to do with the quality of performance of the radial engine relative to the plane wave engine. One difficulty in a purely plane wave engine is the generation of higher harmonics, reducing the energy which might be supplied to the fundamental mode. Since the harmonics of the radial engine are determined by Bessel functions rather than sines and cosines, they are not integral multiples of the fundamental resonant frequency, so the resonator should not enhance the non-linear generation of higher harmonics. A third original interest was the effect of sloped stacks in radial wave thermoacoustic engines, but theory has shown that the effect in radial prime movers with a natural slope between plates is minimal (this will be shown in Chapter 6).

4.2 Comparison of Plane and Radial Wave Harmonic Generation

In most cases, the linear acoustic wave equation suffices to describe the behavior of a system. However, when the acoustic pressure amplitude reaches a sufficient base value, higher order terms must be taken into account. Coppens and Sanders accounted for non-linear effects for finite-amplitude standing waves in a resonance tube by modifying the linear equations of state and continuity to allow for second order effects.³² Chen included an additional second order term in the momentum equation for the same problem and found the correction to be small,³³ as would be expected since good agreement was shown between theory and experiment using the Coppens and Sanders approximation.

This has particular application to thermoacoustic prime movers. The general behavior of a prime mover was effectively described by Atchley *et al.*³⁴

“Once onset of self oscillation is reached, the acoustic amplitude in the tube immediately assumes a large value, typically about 1 % of the ambient pressure. The observed waveform is noticeably non-sinusoidal. As more energy is supplied to the hot end of the stack, the temperature of that end increases only slightly while the acoustic amplitude in the tube increases rapidly ... Unfortunately, as the acoustic amplitude increases, an increasing fraction of the acoustic energy appears as higher harmonics - harmonic distortion increases.”

Atchley *et al.*³⁴ presented results for a constant cross-section plane wave prime mover immediately after onset and also when the hot end temperature was raised 43 K beyond the necessary temperature for onset. In both cases, non-linear generation of higher harmonics was demonstrated. The experimental results for the relative amplitudes of the harmonics to the fundamental in the prime mover just beyond onset provided nice agreement with the theory of Ref. 32.

It is desirable in a prime mover to minimize the generation of higher harmonics so that more acoustic energy is trapped in the fundamental. In a plane wave resonator, one of the ways to accomplish this is to vary the cross-section of the tube. This detuning of the resonator causes the natural modes of the resonator to be anharmonic so that they do not enhance non-linear harmonic generation. Gaitan and Atchley, following the method outlined by Coppens and Sanders in a later paper, investigated higher harmonic generation in tubes with harmonic and anharmonic natural modes for application to thermoacoustic engines.^{35,36} The anharmonic tubes were made by varying the tube cross-section in the center of the tube to a size different than at the ends of the tube. Experimental results for the amplitudes of the harmonics for a given amplitude of the fundamental were in excellent agreement with theory for both harmonic and anharmonic tubes. In the case of the harmonic tube, the amplitude of the first harmonic was only 10-20 dB below the fundamental, depending upon the acoustic pressure amplitude. However, in two separate anharmonic tubes (one with a larger center cross-section than

at the ends and one with a smaller center cross-section) the amplitude of the first harmonic was reduced to 30-40 dB below the fundamental, depending upon the acoustic pressure amplitude.

The generic non-linear wave equation presented in Ref. 36 is

$$\sum_n \left(c_n^2 \nabla^2 - \frac{\partial^2}{\partial t^2} + \frac{n\omega}{Q_n} \frac{\partial}{\partial t} \right) \frac{p_n}{\rho_0 c^2} = - \frac{\partial^2}{\partial t^2} \left[\left(\frac{u}{c} \right)^2 + \frac{\gamma-1}{2} \left(\frac{p}{\rho_0 c^2} \right)^2 \right], \quad (4.1)$$

where c_n and Q_n are the sound speed and quality factor of the n th resonance of the tube, ω is the angular driving frequency (the fundamental resonance for a prime mover), p_n is the acoustic pressure of the n th harmonic of the driving frequency, u and p are the total acoustic velocity and pressure and are functions of radial location r in radial systems (or longitudinal position z in plane systems) and time t . Equation 4.1 is valid near resonance and assumes the total standing wave to be of the form

$$p = \sum_{n=1}^{\infty} p_n = \sum \rho_0 c^2 M R_n \cos(nkz) \sin(n\omega t + \phi_n), \quad (4.2)$$

where M is the peak Mach number of the fundamental, R_n is the nondimensional amplitude of the n th harmonic, k is the wave number of the driving frequency, and ϕ_n is

the temporal phase of the n th harmonic. For a radial system, Eq. 4.2 would have J_0 in place of cosine. The harmonic amplitudes, R_n , are shown in References 35 and 36 to be directly proportional to

$$R_n \propto Q_n \cos\left(\tan^{-1}\left(2Q_n \frac{n\omega - \omega_n}{\omega_n}\right)\right), \quad (4.3)$$

where ω_n denotes normal modes of the resonator, so that the harmonic amplitudes are maximized when the normal modes correspond exactly to the harmonics of the fundamental frequency. Therefore, a detuned resonator leads to a reduction in the amplitudes of the harmonics.

With the existing radial wave prime mover, we are limited to examination of the behavior of the system just above onset. The reason for this is that when attempts are made to increase the temperature beyond onset, the tendency is to increase the acoustic pressure amplitude and thus increase the heat being transported by the acoustic wave from the hot side of the stack to the cold side of the stack. The cold heat exchanger is not able to keep up with the heat load at these higher amplitudes, and the system begins to go in and out of onset. The cycle is described as follows. When the necessary temperature difference is reached, the system begins to produce sound. The heat transport then increases to a point where the cold heat exchanger can not keep up with

the heat being delivered by conduction and acoustic heat transport, and the cold side heats up until the temperature difference across the stack falls below the necessary difference for oscillations to be maintained. When the acoustic wave ceases, the acoustic heat transport also ceases, and the cold heat exchanger cools back down. When the temperature difference becomes sufficient, the acoustic wave is again generated and the cycle is repeated. A similar effect was observed by Olson and Swift in a plane wave prime mover.³⁷ Though it would be nice to get a comparison of plane and radial prime movers at lower and higher acoustic pressure amplitudes, the results for temperatures just above onset should give some insight into the reduction of higher harmonic generation which occurs in radial systems as compared to plane systems.

Figure 4.1 shows a spectrum from the previously described radial wave prime mover. The hot heat exchanger temperature is 427 K and the ambient heat exchanger temperature is 293 K, giving a temperature difference of 134 K. The fundamental frequency of oscillation is 288 Hz in air at atmospheric pressure. The sound pressure level (SPL) at the microphone is 153 dB. Using Eq. (2.31) the SPL at the center of the resonator is estimated to be 161 dB. The first radial wave harmonic occurs at about 526 Hz, but there is no noticeable signal at this frequency. The first non-linear harmonic occurs at twice the fundamental, or 584 Hz. There is a significant harmonic generation at this frequency, with a SPL of 115 dB. However, this is 38 dB below the fundamental. Frequencies were measured to within 0.5 Hz. These results are very similar to those of

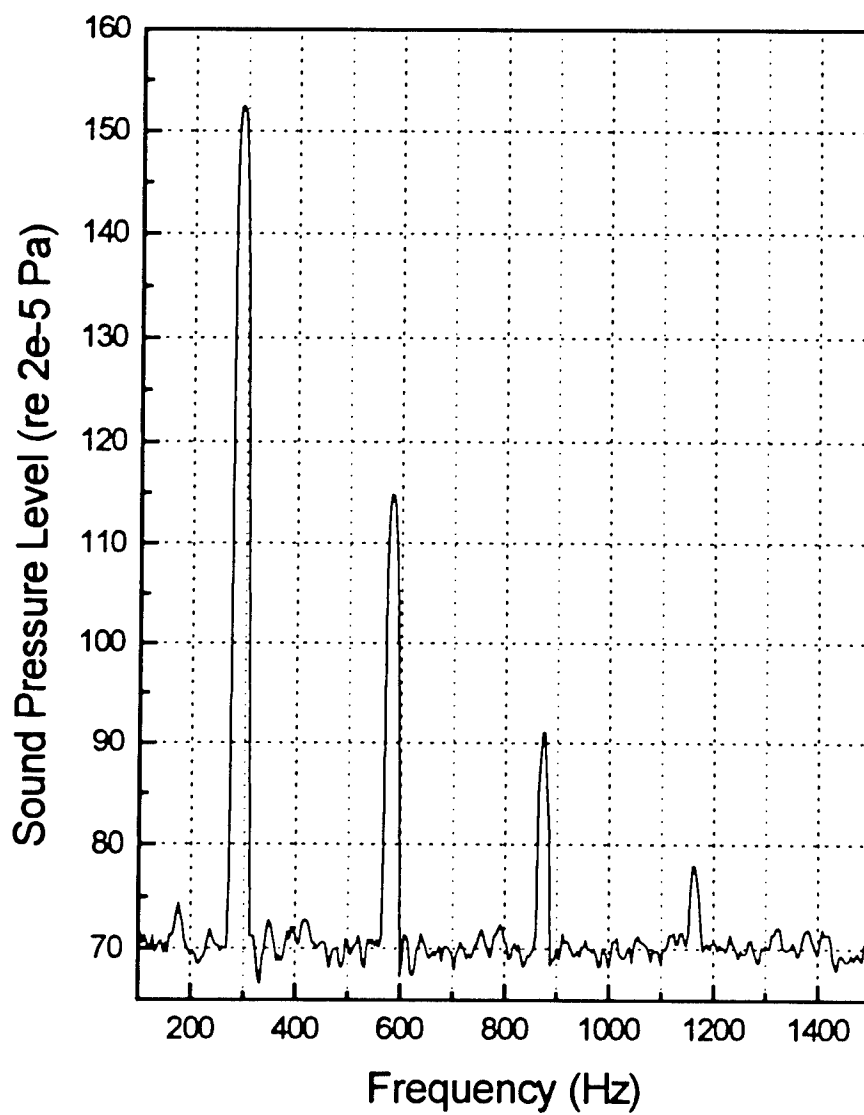


Figure 4.1: Acoustic spectrum from the radial wave prime mover in air at atmospheric pressure.

Ref. 35 for a detuned plane wave resonator driven by a piston. In both cases, the first harmonic is nearly 40 dB below that of the fundamental, and there is no noticeable sound production at the other normal modes of the tubes. In the radial prime mover, the second and third nonlinear harmonics occur at three and four times the fundamental, 876 Hz and 1.168 kHz, and are 63 dB and 75 dB below the fundamental, respectively.

For comparison, a constant cross-section plane wave prime mover was constructed (the plane wave prime mover is pictured in Fig. 3.5), and the spectrum is shown in Fig. 4.2. The hot heat exchanger temperature is 410 K and the ambient heat exchanger temperature is 300 K for a temperature difference of 110 K. The frequency of operation was the same as in the radial case, 288 Hz, and the thermoacoustic elements were located at the position predicted to give the lowest temperature difference necessary to produce sound. A ceramic square pore stack and parallel-plate copper heat exchangers were used. The microphone was located at the ambient end of the tube. The sound pressure level (SPL) at the microphone was 156 dB. The first harmonic occurs at twice the fundamental frequency, or 576 Hz. There is a large contribution at this frequency, with a SPL of 137 dB, only 19 dB below the fundamental (compared to a first harmonic which was 38 dB below the fundamental in the radial prime mover). The first through sixth harmonics give noticeable contributions in the plane engine compared to only the first through third harmonics in the radial engine. The results of the plane wave prime mover are similar to those of Ref. 34 for a prime mover just beyond onset, and

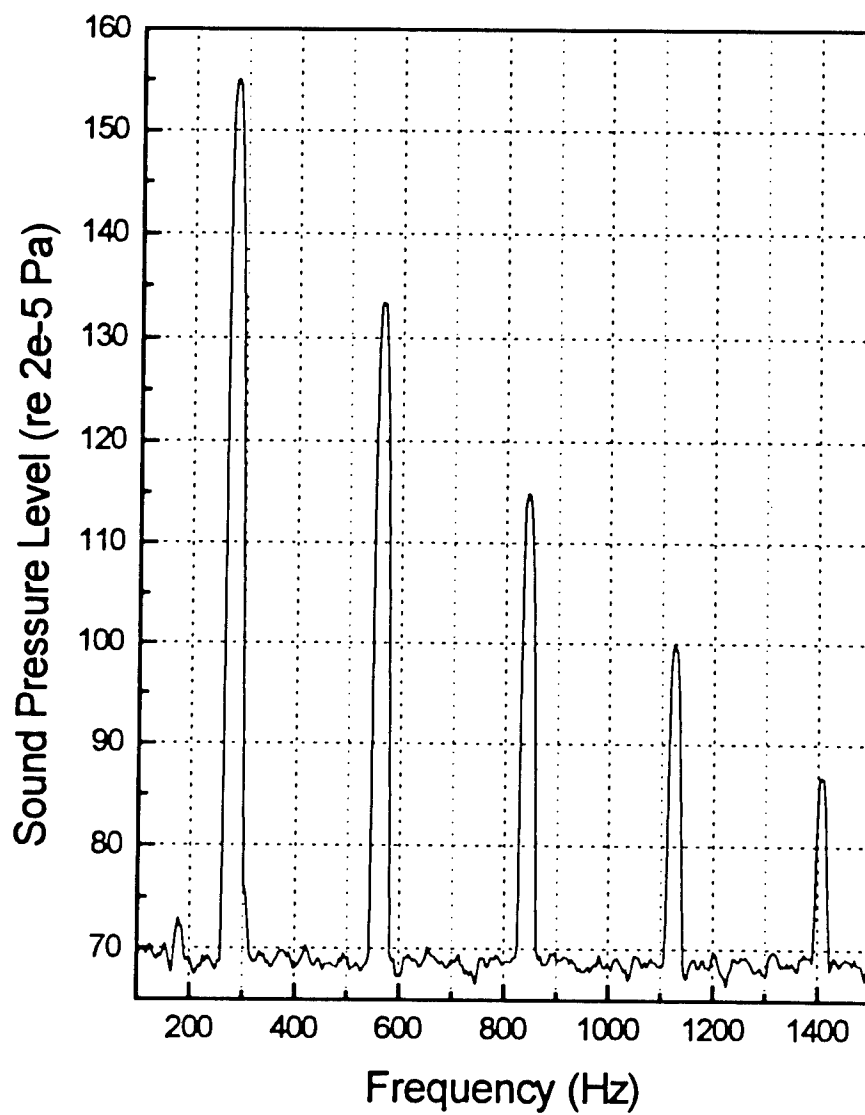


Figure 4.2: Acoustic spectrum from the plane wave prime mover in air at atmospheric pressure.

Ref. 35 for a harmonic resonator driven by a piston. In all three cases, the first harmonic has an amplitude about 20 dB below the fundamental with more harmonics having significant amplitudes than in the radial and detuned plane resonators.

The reduction in higher harmonic generation for the radial engine is understood qualitatively by considering the proximity of the non-linear higher harmonics to the natural modes or overtones of the resonator. In general, the non-linear harmonics have a very narrow bandwidth³⁴ while the overtones have a wider bandwidth. In the case of the plane resonator the non-linear harmonics are not exactly the same as the overtones, since a very slight detuning of the overtones occurs due to dissipation in the resonator and the thermoacoustic elements; however, the two are in the same vicinity so that the non-linear harmonics certainly fall within the bandwidth of the overtones, thus enhancing the higher harmonic generation. The radial engine and detuned plane resonators, by contrast, have no overtones in the vicinity of the non-linear harmonics so that these systems do not enhance the generation of higher harmonics. An advantage of a radial system is that no variation in tube shape is necessary to make the resonator anharmonic.

4.3 Initial Comparison of Experimental and Theoretical Onset Temperatures

The onset temperature (ΔT) is defined as the temperature difference between the hot and ambient sides of a thermoacoustic prime mover at which acoustic oscillations are produced. Correct prediction of ΔT , in addition to being a useful tool in prime mover

design, is an indication that the radial wave theory which has been developed⁵ is correct and the numerical implementation of the theory⁵ is accurate and useful for future radial refrigeration performance predictions.

Measurements of the onset temperature have been made on the previously described radial wave prime mover. Thermocouples were placed in the heat exchangers (attempts to measure the temperature at the face of the stack gave ambiguous results due to the short radial length of the stack and an inability to precisely position the thermocouple). Belcher assumed that the variation of the stack face temperatures from those of the heat exchangers was negligible, and thus took ΔT to be the temperature difference between the two heat exchangers.⁹ Figures 4.3 and 4.4 show the best (lowest) experimental onset temperature results (solid circles) achieved as a function of ambient pressure, for air and argon respectively. Ambient temperature in both cases was 293 K. Also shown are the theoretical predictions for the hot side temperature (dashed line) *assuming that the stack faces maintain the same temperature as the heat exchangers*. For the present discussion, the dotted lines in Figures 4.3 and 4.4 should be ignored. It is obvious that theory and experiment are not at all in agreement, with the experimental onset temperatures being significantly higher than predicted for both fluids.

There are three noticeable problems with the radial engine. First, the measurements are sensitive to the "fit" of the heat exchangers around the stack. The heat exchanger "fit" is not as difficult in the plane wave case, since the stack surfaces can

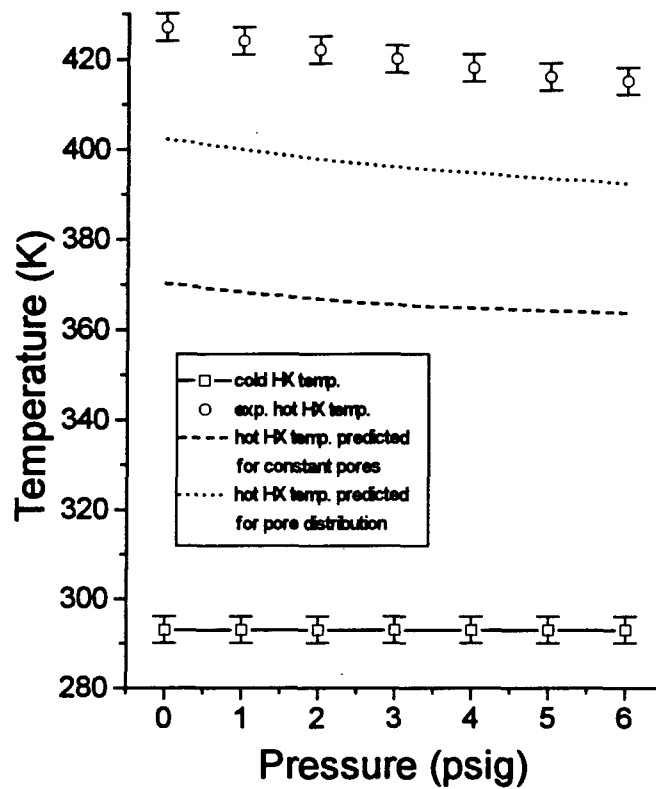


Figure 4.3: Onset temperatures for the radial wave prime mover with air as the working fluid, assuming no temperature discontinuity between the stack and heat exchangers. Solid line shows cold heat exchanger temperature, dashed line is the predicted hot heat exchanger temperature for a stack with a single pore size, dotted line is the predicted hot heat exchanger temperature for the stack with the pore distribution shown in Fig. 4.5, and circles show experimental results.

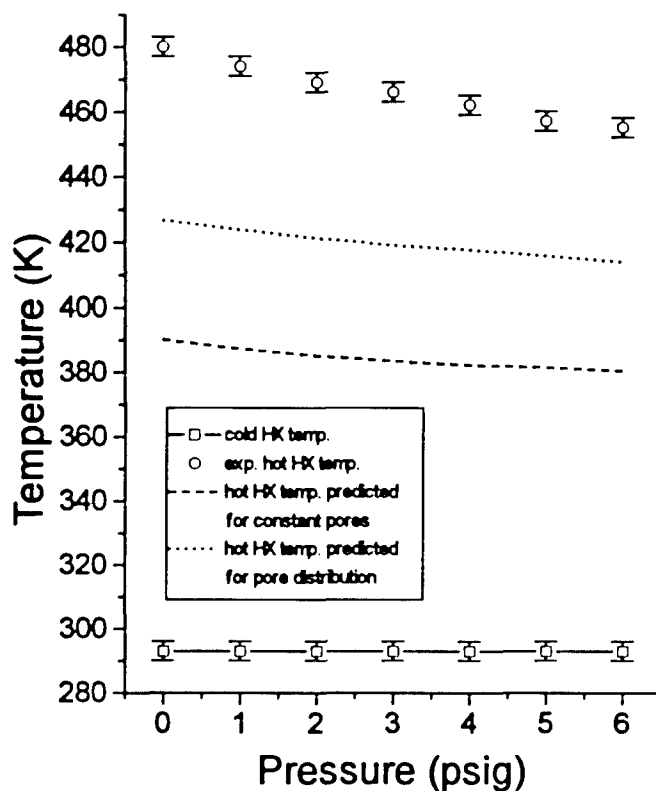


Figure 4.4: Onset temperature difference for the radial wave prime mover with argon as the working fluid, assuming no temperature discontinuity between the stack and heat exchangers. Solid line shows cold heat exchanger temperature, dashed line is the predicted hot heat exchanger temperature for a stack with a single pore size, dotted line is the predicted hot heat exchanger temperature for the stack with the pore distribution shown in Fig. 4.5, and circles show experimental results.

be forcibly wedged between the heat exchangers with no alteration of the stack pore shape, so that direct thermal contact is sustained between the stack and the heat exchanger. This is more difficult in the radial case since the heat exchanger surfaces are not flat and must maintain perfect curvature to provide the best possible thermal contact between stack and heat exchanger. Attempts to force the heat exchangers against the stack, thus creating the necessary curvature in the heat exchangers, tend to distort the stack plate spacing (since the heat exchanger is much more rugged than the stack, a point is reached where the stack conforms to the heat exchanger shape via warping of the stack plates rather than the heat exchanger conforming to the stack shape). Results for ΔT varied from experiment to experiment, as indicated above by the phrase "best results", depending upon the proximity of the heat exchangers to the stack. The second problem is the short radial stack length of the existing radial prime mover stack. For a stack with a longer radial dimension, the fit would become less important, as we will see later. A third problem is due to the unstressed variance in plate spacing in the mica stack.

4.4 Non-uniform Stack Plate Spacing

As mentioned in the previous chapter, attempts were made to maintain a constant plate spacing throughout the stack by using mica washer spacers and later by adding teflon thread to maintain the correct spacing. In hindsight, it would have been much better to use thicker (and thus more rigid) mica plates in the stack at the expense of

significantly reducing the stack porosity (this would also have prevented additional distortion of the stack spacing due to pressure from the heat exchangers). However, with the materials at hand we were left with a porous, but rather flimsy stack. In order to characterize the present stack, measurements were made by photocopying and enlarging several locations on the face of the stack, measuring the plate spacings over the entire height of the stack (this assures that the average spacing is equal to the previously expected constant spacing), and scaling the measurements back down to their true values. Over 500 measurements were made to assure an accurate representation of the pore size distribution. Fig. 4.5 shows the resulting distribution in terms of the percent of the total open area in the stack occupied by each different plate spacing.

Prediction of the onset temperature, ΔT , for a stack with a distribution of pore sizes is accomplished by treating the various pore sizes as having impedances in parallel. The electrical analog would be a set of parallel resistors. Beginning with a known impedance and pressure amplitude at the hot, rigid end of the resonator, the pressure and impedance at the hot face of the stack may be determined using the translation theorems, Eqs. 2.28 and 2.29. The boundary conditions at the hot face of the stack are continuity of pressure and volume velocity, so

$$P_i = P_{hot}, \quad (4.4)$$

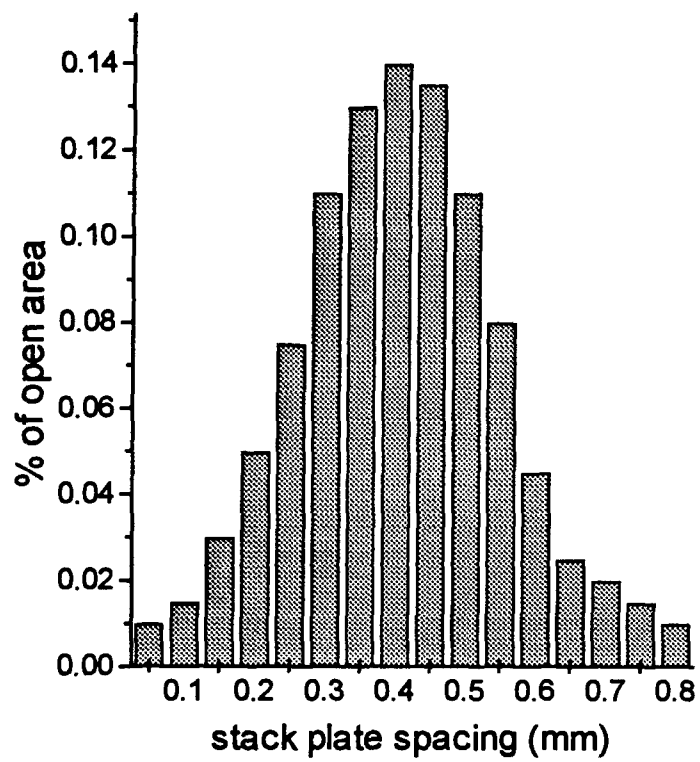


Figure 4.5: Area distribution of plate spacing in the radial prime mover stack.

and

$$\sum_i A_i V_i = A_{hot} V_{hot} , \quad (4.5)$$

where i represents quantities for a given pore size at the hot side of the stack, P_i is the complex acoustic pressure at the hot side of an individual pore, P_{hot} is the pressure at the hot face of the stack determined by translation, A_i is the stack cross-section occupied by a particular pore size, A_{hot} is the resonator cross-sectional area at the hot face of the stack, V_i is the bulk particle velocity averaged over the cross-section of the stack having a given plate spacing at the hot side, and V_{hot} is the velocity at the hot face of the stack determined by translation.

To obtain a full numerical solution to the problem, it would be necessary to postulate guesses for the complex pressure P_{cold} and the various pore velocities v_j at the cold side of the stack, integrate backwards to the hot side of the stack checking to see if the conditions in Eqs. 4.1 and 4.3 have been met, and repeat the process with new guesses until the solution converges. This would require scanning an extremely large parameter space. Therefore, the method of Raspet *et al.* for approximating thermoacoustic calculations using a single step³⁸ has been utilized to reduce computation times. The single step method was shown to be accurate for $|kL| \leq 0.3$, where L is the

stack length and k is the wavenumber defined in Eq. 2.24. The radial prime mover certainly meets this criterion since $|kL| \approx 0.065$.

The assumptions made in Chapter 3 still apply, namely that the acoustic pressure is constant across the pore cross section and is a function only of the radial distance along the pore, and that the transverse velocity is small relative to the radial velocity. The relevant equations describing the fluid motion in the pore are taken from Eqs. 2.14 and 2.22 (with porosity accounted for such that $v_r(r) = V_i / \Omega_i$, where Ω_i is the porosity for a given pore size) and are given by

$$V_i = \frac{\Omega_i F(\lambda)}{i\omega \rho_0} \frac{dP_i}{dr} \quad (4.6)$$

and

$$\frac{dV_i}{dr} + \frac{1}{T} \frac{dT}{dr} \left[\frac{F(\lambda_r)/F(\lambda) - 1}{1 - N_{pr}} \right] V_i + \frac{V_i}{r} + \frac{\Omega F(\lambda)}{i\omega \rho_0} k^2 P_i = 0, \quad (4.7)$$

where k^2 is given by Eq. 2.24. The finite difference forms of these equations are given by

$$iA \frac{V_i + V_j}{2} = \frac{P_i - P_j}{L} \quad (4.8)$$

and

$$iA \frac{V_i - V_j}{L} + iAB \frac{V_j + V_i}{2} + k^2 \frac{P_j + P_i}{2} = 0, \quad (4.9)$$

where

$$A = \frac{\omega \rho_0}{\Omega F(\lambda)}, \quad (4.10)$$

and

$$B = \frac{1}{T} \frac{dT}{dr} \left[\frac{F(\lambda_r)/F(\lambda) - 1}{1 - N_{pr}} \right] + \frac{1}{r}, \quad (4.11)$$

subscript j refers to pore quantities at the cold side of the stack, and all parameters are evaluated at the center of the stack. Note that the volume coefficient of expansion, β , in

Eq. 4.11 has been replaced by the ideal gas result, $1/T$.³⁹ Equations 4.8 and 4.9 may be combined to eliminate V_j so we are left with V_i in terms of P_i and P_j

$$V_i = \frac{1}{iAL} \left\{ P_i \left[1 - \frac{BL}{2} - \frac{k^2 L^2}{4} \right] - P_j \left[1 - \frac{BL}{2} + \frac{k^2 L^2}{4} \right] \right\}. \quad (4.12)$$

Now, we need only to guess the magnitude and phase of P_j , and use the known pressure P_i to determine V_i . These values of V_i are then tested to see if the condition in Eq. 4.5 holds. If the requirement is not met, P_j is adjusted and the process is repeated. When the requirement is met, Eq. 4.8 is rearranged to give V_j using the now known values for V_i , P_i , and P_j . The pressure and velocity at the cold side of the stack are then determined by requiring conservation of pressure and volume velocity

$$P_{cold} = P_j \quad (4.13)$$

and

$$A_{cold} V_{cold} = \sum_j A_j V_j, \quad (4.14)$$

where P_{cold} is the pressure in the tube at the cold face of the stack, A_{cold} is the resonator cross-section at the cold face of the stack, and V_{cold} is the area averaged particle velocity in the tube at the cold face of the stack.

Using the method outlined above, the onset temperature was determined for a stack having a distribution of pore sizes (see section 2.8 for a description of onset temperature calculations). The dotted lines in Figures 4.3 and 4.4 show corrections, using the measured pore distribution of Fig. 4.5, to the constant pore size results represented by dashed lines for the hot side temperature at onset in air and argon, respectively. It is obvious that the pore distribution in the stack explains a significant portion of the discrepancy between experiment and theory, but further interpretation is required to account for the remaining disparity.

4.5 Temperature Discontinuities Between the Heat Exchanger and the Stack Face

As the stack in a thermoacoustic prime mover becomes very short, the temperature gradient necessary for onset of oscillations increases, which in turn raises the amount of heat flowing via thermal conduction from the hot side to the cold side of the stack. In addition, any small gap between the stack and the heat exchanger becomes a more appreciable percentage of the stack length, so that the heat which is conducted across the gap may no longer be ignored by assuming that the stack face and the heat exchanger maintain the same temperature. Rather, it becomes necessary to account for

conduction through the fluid across gaps between stack and heat exchanger as well as for normal thermal conduction through the stack, when determining the temperatures at the faces of the stack which ultimately are responsible for causing onset.

A simple model may be used to explain the remaining difference between experiment and theory, and why the difference is much more noticeable for the radial engine than for Belcher's plane wave device. Consider the heat exchanger - stack - heat exchanger pictured in Fig. 4.6. Perfect insulators have been placed on top and bottom to confine heat flows to the horizontal direction. The hot and cold heat exchangers are held at temperatures T_H and T_C . Rather than assuming that the stack face and the heat exchanger are in physical contact and at the same temperature, they are separated by a small gap of length ℓ filled with gas. The stack length is again denoted by L . Assumptions are : heat is transported only by conduction, κ_C (the thermal conductivity of the gas in the gap near the cold heat exchanger) is evaluated for a temperature of T_C , κ_H (the thermal conductivity of the gas in the gap near the hot heat exchanger) is evaluated for a temperature of T_H , κ_S (the thermal conductivity of the solid stack material) is assumed to be constant and is evaluated for a temperature of $\frac{1}{2} (T_H - T_C)$. Our goal is to find T_1 and T_2 in terms of the known quantities ℓ , L , T_C , T_H , κ_C , κ_H , and κ_S . Assuming linear temperature gradients within the three regions and applying boundary conditions, the temperature in each region is given by

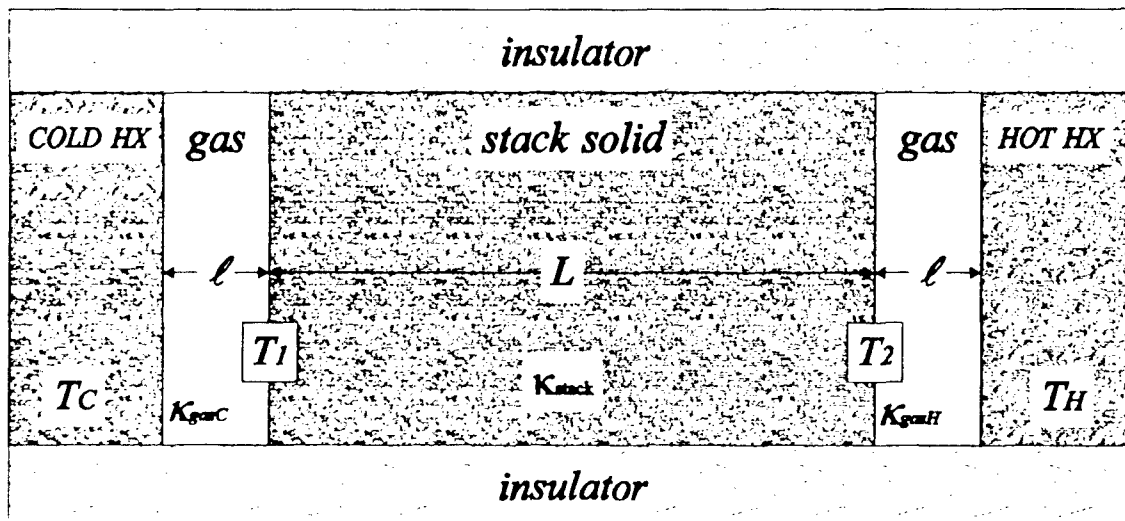


Figure 4.6: Illustration of the gaps present between the radial stack and heat exchangers.

$$T_{0 \leq x \leq \ell} = \frac{T_c(\ell - x) + T_1 x}{\ell}, \quad (4.15)$$

$$T_{\ell+L \leq x \leq 2\ell+L} = \frac{T_1(\ell + L - x) + T_2(x - \ell)}{L}, \quad (4.16)$$

and

$$T_{\ell+L \leq x \leq 2\ell+L} = \frac{T_2(2\ell + L - x) + T_H[x - (\ell + L)]}{\ell}. \quad (4.17)$$

Since no heat is being generated in the gas or the stack solid, we require that the heat flowing through each segment (cold gas, solid stack, and hot gas) be the same. Using the heat conduction equation

$$q = -\kappa A \nabla T, \quad (4.18)$$

where q is heat, A is the cross-sectional area, and T is temperature, and equating q for the cold gas and the solid stack results in

$$T_2 = \frac{\kappa_H T_H + \kappa_C T_C - \kappa_C T_1}{\kappa_H} \quad (4.19)$$

Similarly, equating q for the solid stack and the hot gas and inserting Eq. 4.8 for T_2 produces

$$T_1 = \frac{[\kappa_C \kappa_H + \kappa_C \kappa_S (\ell/L)] T_C + \kappa_H \kappa_S T_H (\ell/L)}{\kappa_H \kappa_C + \kappa_H \kappa_S (\ell/L) + \kappa_C \kappa_S (\ell/L)} \quad (4.20)$$

Examining Equations 4.8 and 4.9, it is evident that as $\ell/L \rightarrow 0$, $T_1 \rightarrow T_C$ and $T_2 \rightarrow T_H$ as expected. In the case of the radial wave prime mover, $L = 1.25 \text{ cm}$ and a good average estimate for ℓ (determined by physical measurement of the gaps between the heat exchangers and the stack) is $\ell = 0.45 \text{ mm}$, producing a ratio of $\ell/L = 0.036$. For the 5.08 cm stack which Belcher used, a conservative estimate would be $\ell = 0.025 \text{ mm}$ so that $\ell/L = 0.002$. This estimate is conservative because in Belcher's engine the heat exchanger and stack were in physical contact across the full stack face.

Figures 4.7 and 4.8 show deviations of the stack face temperatures from the heat exchanger temperatures over a range of heat exchanger temperature differences for the above values of ℓ/L for air and argon. From Fig. 4.7 we see that the radial prime mover does a poor job of establishing the expected temperature difference across the stack due to the short radial length of the stack and the presence of non-negligible gaps

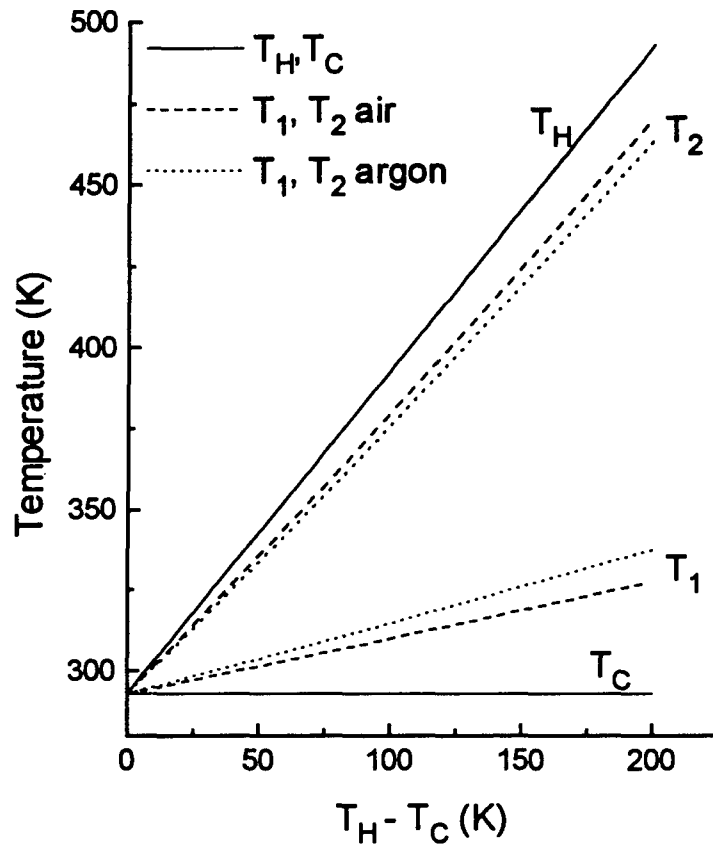


Figure 4.7: Demonstration of the temperature discontinuity between the stack and heat exchanger face for $\ell / L = 0.036$. The various temperature locations are shown pictorially in Fig. 4.6.

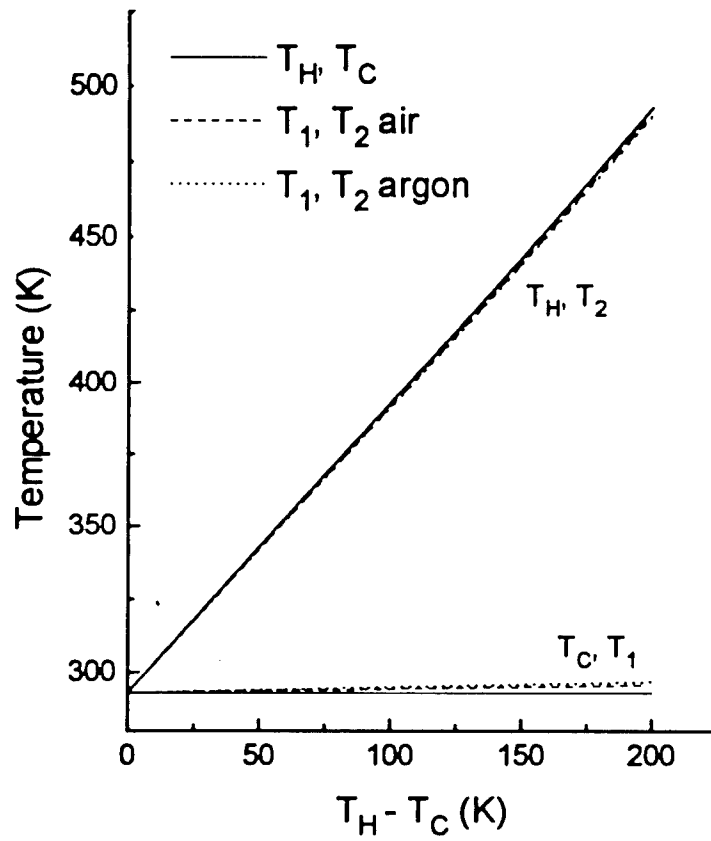


Figure 4.8: Demonstration of the temperature discontinuity between the stack and heat exchanger face for $\ell / L = 0.002$. The various temperature locations are shown pictorially in Fig. 4.6.

between the stack and heat exchanger. For a 150 K difference across the heat exchangers, the actual difference across the stack is only 106 K for air and 94 K for argon, while a conservative estimate for Belcher's 5.08 cm stack shown in Figure 4.8 gives differences of 147 K for air and 144 K for argon. Experiments by Belcher also verified the need for an increased heat exchanger temperature difference for heat exchangers displaced from the stack in a plane wave prime mover. From the above results, it is clear that Belcher's assumption that the heat exchanger temperature was equivalent to the stack face temperature was much more appropriate than the same assumption would be in the case of our radial wave prime mover.

Previously, it was mentioned that experimental measurements of ΔT varied depending upon the "fit" of the heat exchangers to the stack. Measurements of the gap between the heat exchangers and the stack range from 0 - 0.6 mm when the heat exchangers are tightened and pressed against the stack. The upper end of this gap can be reduced to about 0.4 mm by lightly hammering the heat exchanger against the stack. Measurements have been made for a forced (hammered) and an unforced (only tightened and pressed) fit of the heat exchangers against the stack. In both cases, ℓ should be close to the average gap value, though a slight variance from the average gap value due to azimuthal heat flows in the fluid and the stack may do a better job of modeling the experimental results. Therefore, an effective gap length, ℓ_{eff} , is defined to simulate the effect that the entire gap distribution has on the onset temperature.

In order to compare experiment with theory using the measured distribution of pore sizes and accounting for a gap between the stack and heat exchangers, T_1 and T_2 are calculated using the measured values for T_C and T_H for a guessed ℓ_{eff} in air (the initial guess is the average gap size). T_1 is then used as the cold side stack temperature in the onset temperature calculation to determine the predicted hot side temperature required for onset, denoted by $T_{2\text{ calc}}$. This predicted value is compared with T_2 . ℓ_{eff} is then adjusted and the process repeated until $T_{2\text{ calc}}$ and T_2 best match up over a range of pressures. Admittedly, this process is rather backwards, since ℓ_{eff} is adjusted to give the best possible results for a given gas (air). However, if the theory is correct, then the resulting ℓ_{eff} for one gas should be applicable to other gases as well. Therefore, the ℓ_{eff} determined for air is used to determine T_1 and T_2 for the prime mover filled with argon, and the resulting T_2 is compared with $T_{2\text{ calc}}$ for argon.

Figures 4.9 and 4.10 show T_C , T_1 , T_2 , T_H , and $T_{2\text{ calc}}$ for air and argon, respectively. The experimental results are the same as shown in Figures 4.3 and 4.4, and again represent the configuration giving the lowest temperature difference for onset. Keep in mind that T_C and T_H are experimental results, however, the comparison will be between the calculated-from-experiment T_2 and the predicted hot side onset temperature using T_1 for the cold side stack temperature, $T_{2\text{ calc}}$. In the upper plot of Fig. 4.9, we see that a chosen value of $\ell_{eff} = 0.2$ mm produces nice agreement for air. Applying this

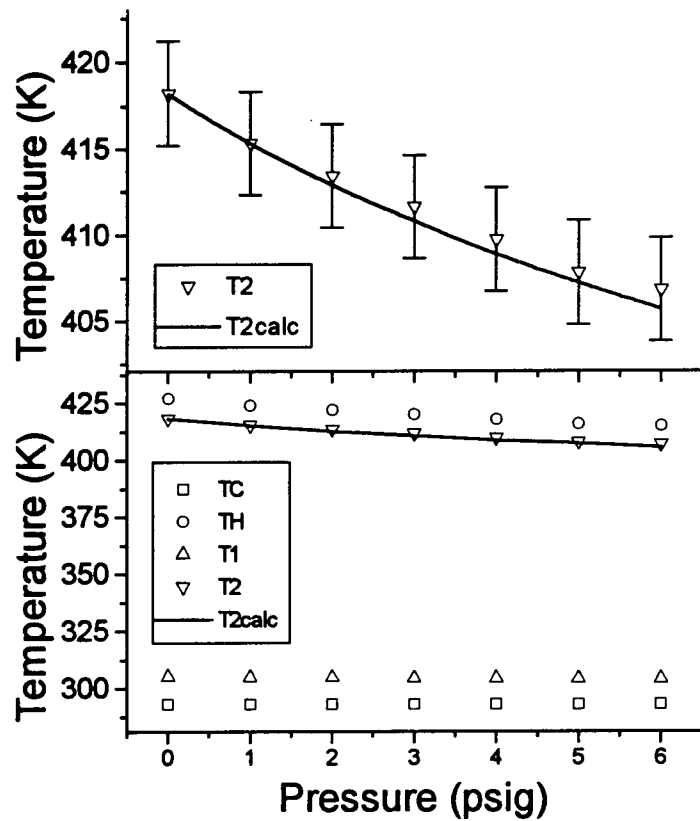


Figure 4.9: Air results for $\ell_{eff} = 0.2$ mm. The upper plot is a blown up version of T_2 and $T_{2\text{ calc}}$ in the lower plot, where $T_{2\text{ calc}}$ is the numerically predicted onset temperature using T_1 as the temperature at the cold side of the stack. Errors in the lower plot are smaller than the data points.

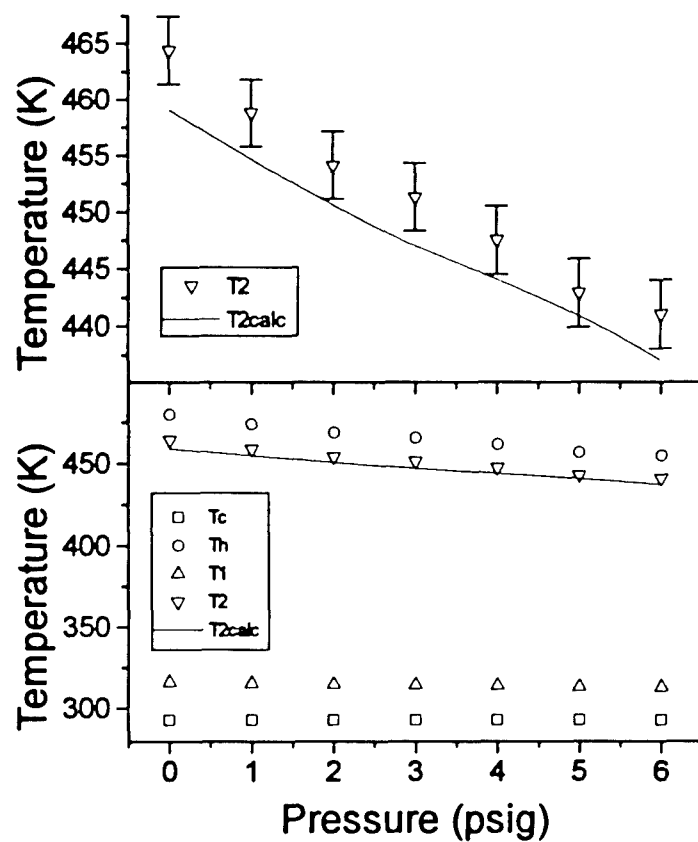


Figure 4.10: Argon results for $\ell_{eff} = 0.2$ mm. The upper plot is a blown up version of T_2 and T_{2calc} in the lower plot, where T_{2calc} is the numerically predicted onset temperature using T_1 as the temperature at the cold side of the stack. Errors in the lower plot are smaller than the data points.

value of ℓ_{eff} to the argon data, we see in the upper plot of Fig. 4.10 that T_2 and T_{2calc} are within 5 K of each other over the pressure range tested, and appear to be following the same general trend. It should be mentioned at this point that it would have been nice to extend the pressure range over which measurements were made, however, due to the large flat surface area of the resonator, increasing the pressure beyond 6 psig would have placed an exorbitant amount of force upon the bolts holding the resonator together, and could have caused the steel plates to bow outward.

Measurements were also made which gave higher onset temperatures due to a looser fitting of the heat exchangers. Figures 4.11 and 4.12 show the results for air and argon, respectively. $\ell_{eff} = 0.41$ mm provides good agreement between T_2 and T_{2calc} in air. Applying this ℓ_{eff} to the argon data also gives good results, such that T_2 and T_{2calc} are within 8 K of each other, and again the general trend of the curves are the same. The agreement is not as good as in the previous case, due to a larger distribution of gaps between the stack and heat exchangers. In particular, we have assumed that ℓ_{eff} is the same at the hot and cold sides of the stack. For a looser fit of the heat exchangers on the stack, this assumption becomes less valid than in the case where the heat exchangers were fit as tightly as possible without disfiguring the stack.

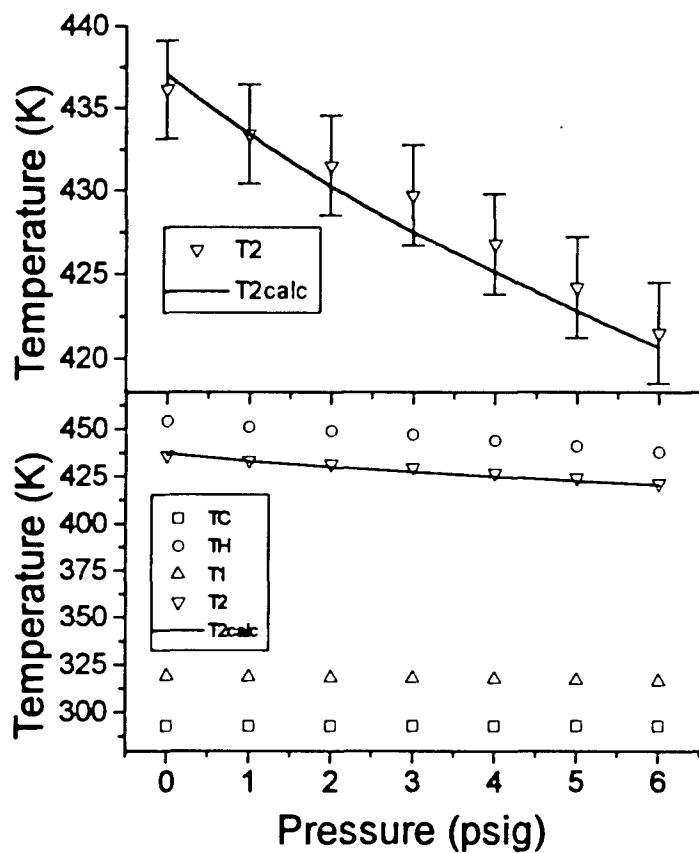


Figure 4.11: Air results for $\ell_{eff} = 0.41$ mm. The upper plot is a blown up version of T_2 and T_{2calc} in the lower plot, where T_{2calc} is the numerically predicted onset temperature using T_1 as the temperature at the cold side of the stack. Errors in the lower plot are smaller than the data points.

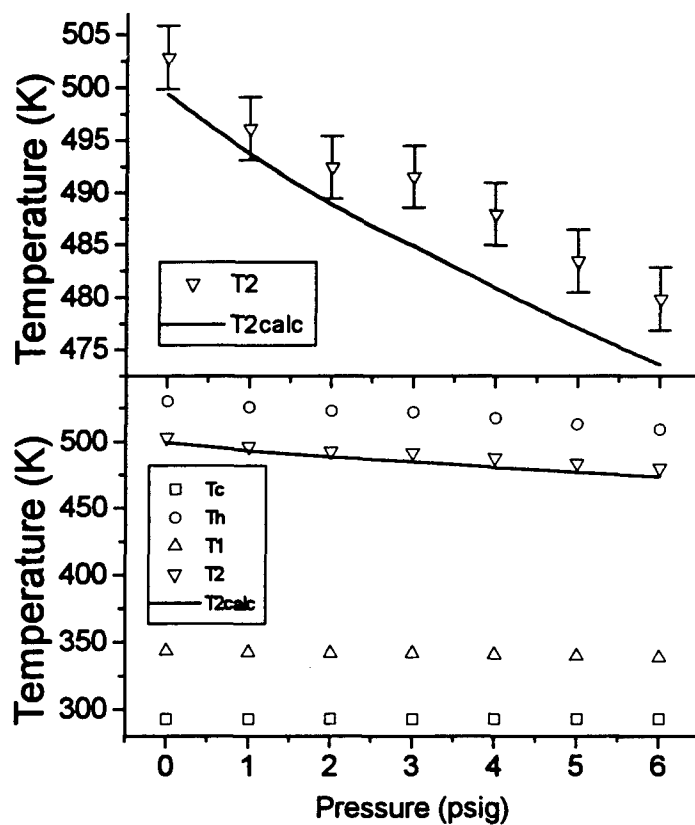


Figure 4.12: Argon results for $\ell_{eff} = 0.41$ mm. The upper plot is a blown up version of T_2 and $T_{2\text{ calc}}$ in the lower plot, where $T_{2\text{ calc}}$ is the numerically predicted onset temperature using T_1 as the temperature at the cold side of the stack. Errors in the lower plot are smaller than the data points.

Chapter 5

Theory of Sloped Stacks in Plane and Radial Wave Thermoacoustic Engines

5.1 Introduction

The radial thermoacoustic stacks described so far have been composed of washer shaped pieces aligned on top of each other to form a parallel plate configuration as in Fig. 2.1. Parallel plate stack configurations present a problem in both the plane and radial geometries since R , the characteristic pore dimension or plate spacing, is constant throughout the stack, while the thermophysical properties of the fluid may vary significantly from the cold side to the hot side of the stack. In particular, the relationship between the plate spacing and the thermal penetration depth (δ_κ) plays an important role in thermoacoustics. Arnott *et al.*²³ showed that, neglecting losses, the thermoacoustic gain produced by the temperature gradient across a prime mover stack *in the short stack approximation* is maximized when the magnitude of the imaginary part of $F^*(\lambda_T)/F^*(\lambda)$ is a maximum. Fig. 5.1 shows that this occurs when $\lambda_T \approx 3.2$ or $R/\delta_\kappa \approx 2.26$. Fig. 5.2 shows δ_κ for Helium gas at a pressure of 200 kPa and an acoustic

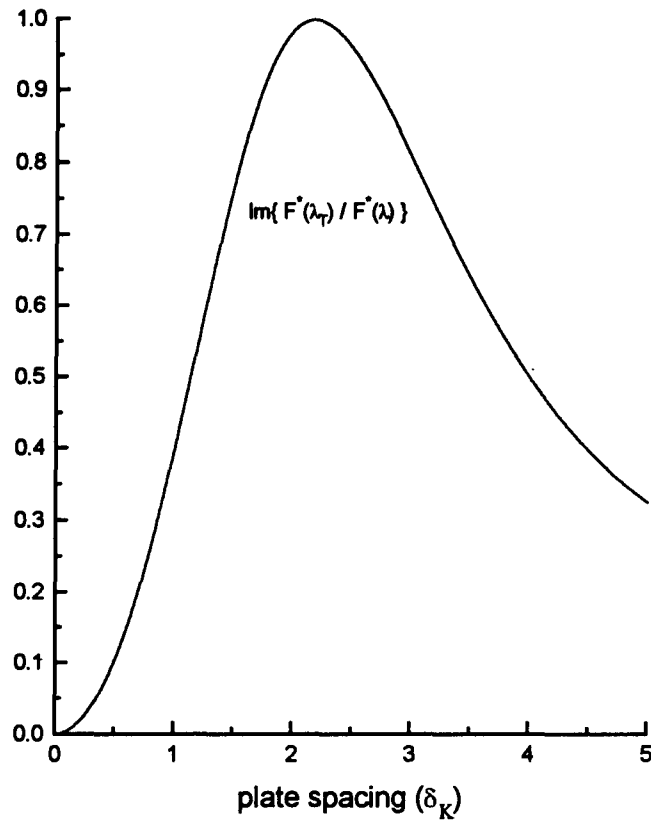


Figure 5.1: Normalized short stack thermoacoustic gain as a function of plate spacing in number of thermal penetration depths. This plot shows that maximum gain occurs for a plate spacing near 2.2 thermal penetration depths.

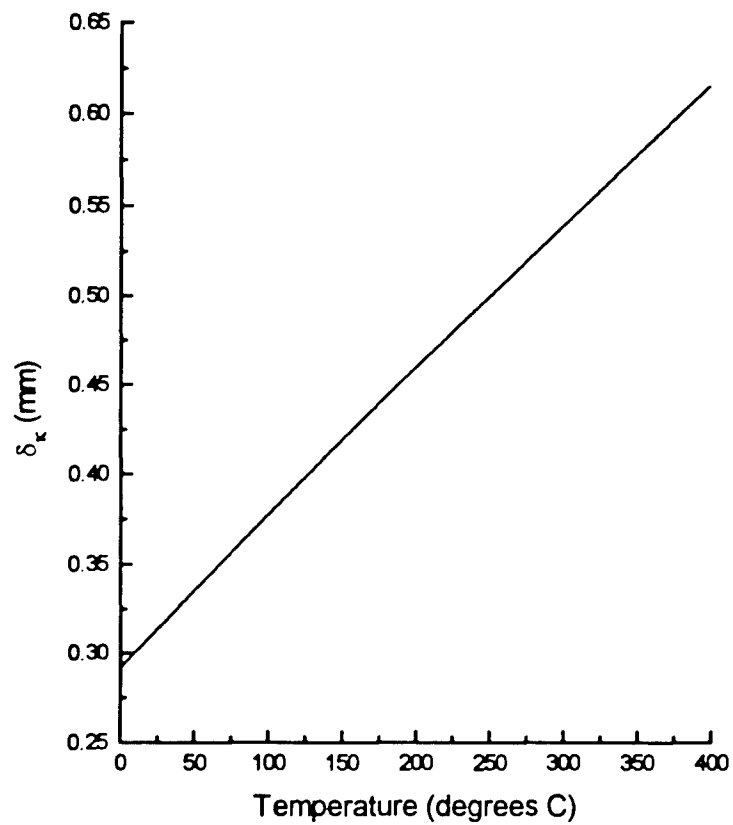


Figure 5.2: Thermal penetration depth as a function of temperature. Calculated for Helium gas, acoustic frequency 300 Hz, and ambient pressure 200 kPa.

frequency of 300 Hz as a function of temperature. It is clear, particularly for a prime mover with a large temperature difference across the ends of the stack, that δ_k can vary by a factor of two or more.

A second important factor in thermoacoustic engine design is the minimization of viscous and thermal losses in the stack. The dominant loss mechanisms in thermoacoustic engines are those due to viscous forces which oppose fluid flow in the stack. Providing good thermal contact between the fluid and the plates, while increasing the thermoacoustic gain or heat pumping ability of an engine, may significantly increase the viscous losses in the system. Analysis of the dependence of the short stack work flow terms in Eq. 3 of Ref. 23 on the thermoviscous dissipation function reveals that a plate spacing which maximizes the thermoacoustic gain in the stack also maximizes the losses in the stack. In addition, the plate spacing can influence the magnitude and phasing of the pressure and velocity in the stack, further influencing the gain and loss terms. A good design must strike a balance between maximizing the thermoacoustic gain or thermoacoustic heat flow and reducing the viscous and thermal losses to achieve the desired results: a large acoustic power output for prime movers and a high COP or heat pumping ability for refrigerators.

One of the anticipated advantages of the radial geometry is that it can easily accommodate a varying plate spacing from the cold to the hot side of the stack. Fig. 5.3 shows the simplest types of stacks in the radial geometry. The washer style stack is

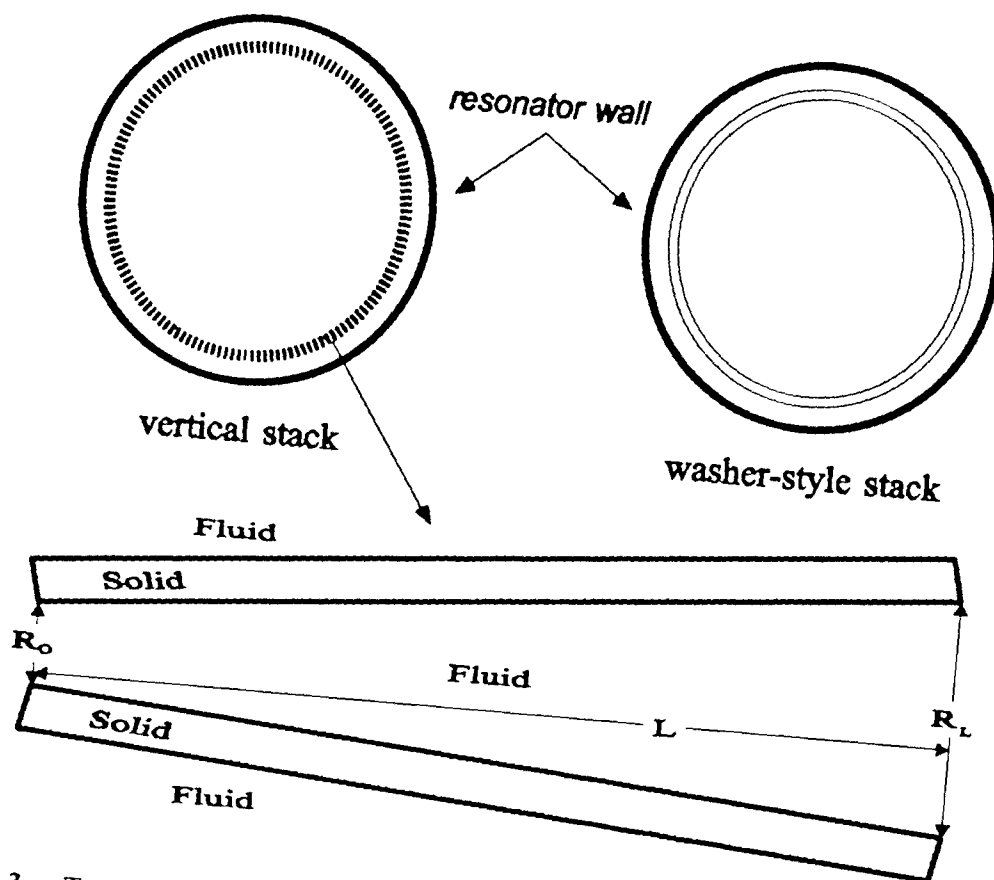


Figure 5.3: Two simplest stacks in the radial geometry. The vertical plate stack provides a naturally varying plate spacing from the cold side to the hot side of the stack.

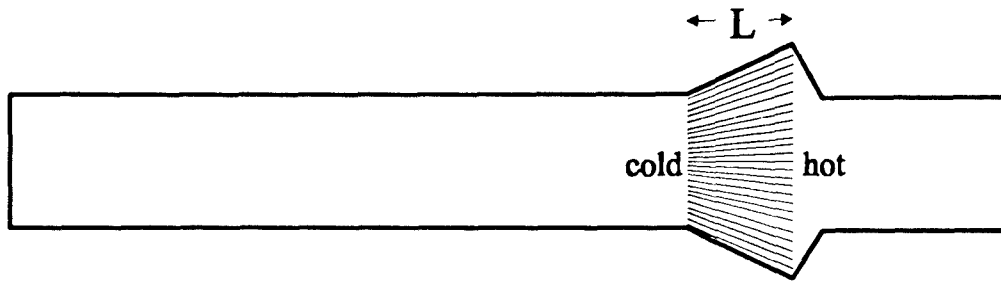
analogous to the parallel plate stack in the plane wave case, while the vertical plate stack allows for a naturally varying plate spacing from the cold side to the hot side of the stack. Sloped stacks can also be utilized in plane wave resonators by varying the cross-sectional dimensions of the resonator, as shown in Fig. 5.4.

5.2 Previous Relevant Analysis

Some previous analysis of Sondhauss tubes is relevant. Thermally driven acoustic oscillations have been studied in Sondhauss tubes with constant cross-section,^{40,41} discontinuous cross-section,⁴² and constantly varying cross-section.⁴³ It was found that a discontinuous increase in the cross-sectional area of the hot end of the tube tends to decrease the temperature difference between the hot and cold ends of the tube at which acoustic oscillations are induced.⁴⁴ Similarly, continuously varying tube cross-sections can decrease the temperature gradient necessary to sustain a given acoustic pressure amplitude when the hot tube cross-section is enlarged.⁴⁵ These ideas are extended to thermoacoustic stacks in resonators.

Sloped stacks in thermoacoustic systems were first examined by Bennett with application to cooling instruments used in hot geothermal wells.⁴⁶ She formulated a solution for sloped stacks using the plane thermoacoustic wave equation for parallel plates by allowing the relevant quantities (λ and λ_T) to change consistent with the slope of the stack. Analyzing Bennett's work for application to vertical plate radial wave thermoacoustic engines, it was noticed that the wave equation itself needed modification

(a)



(b)

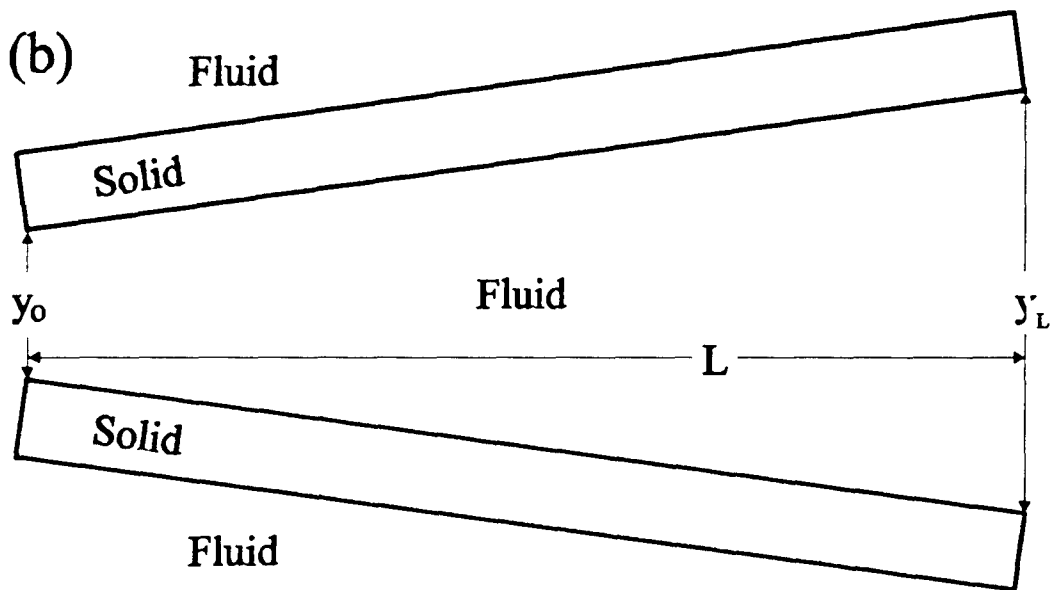


Figure 5.4: Sloped stack plane wave thermoacoustic engine. (a) shows the resonator and elements. (b) is a close-up of the space between two adjacent plates.

for application to sloped stacks. Beginning with the correct wave equation, the general theory for sloped stacks in thermoacoustic systems, applicable to plane and radial wave prime movers and refrigerators, is presented in the following sections.

5.3 Wave Equation for Thermoacoustic Engines with Sloped Stacks

The thermoacoustic equations for radial engines which were reviewed in Chapter 2 are already applicable to sloped stacks in the radial geometry if the varying plate spacing is taken into account in λ and λ_T when stepping through the stack in a numerical integration. In this chapter, the problem will be approached from the more general plane wave perspective, but is completely applicable to the radial case. The wave equation for parallel plate thermoacoustic engines is⁹

$$\frac{\rho_0}{F(\lambda)} \frac{d}{dr} \left[\frac{F(\lambda)}{\rho_0} \frac{dp_1(r)}{dr} \right] + 2\alpha(\lambda, \lambda_T) \frac{dp_1(r)}{dr} + k^2(\lambda, \lambda_T) p_1(r) = 0 \quad , \quad (5.1)$$

where $\alpha(\lambda, \lambda_T)$, $k^2(\lambda, \lambda_T)$, and $F(\xi)$ are given by Eqs. (2.23), (2.24), and (2.15); γ is the ratio of fluid specific heats, $\rho_0(r)$ is the ambient density, c is the speed of sound in the fluid, ω is the oscillatory angular frequency of the acoustic variables, $p_1(r)$ is the acoustic pressure, β is the coefficient of thermal expansion of the fluid, N_{pr} is the Prandtl number of the fluid, $T_0(r)$ is the mean fluid temperature, λ is the shear wave number

given by Eq. (2.12), λ_T is the thermal disturbance number given by Eq. (2.13), and δ_v (δ_v) is the thermal (viscous) penetration depth in the fluid. Refer to Eq. (2.22) for the corresponding wave equation for the radial geometry.

Fig. 5.4 shows a plane wave thermoacoustic engine with a constant slope between successive plates. Bennett accounted for a sloped engine by replacing R , the plate spacing, with $R(r)$ in the parallel plate wave equation (Eq. 5.1), where

$$R(r) = R_0 + \varsigma r \quad , \quad (5.2)$$

R_0 is the plate separation at the cold (left) side of the engine, $\varsigma = (R_L - R_0) / L$ is the slope of the plates relative to each other, L is the engine or stack length, $R_L = R(L)$ is the plate separation at the right side of the stack, and r is the distance from the left side of the stack.

Allowing for a constant slope between stack plates, λ and λ_T in Eq. (5.1) are now position dependent quantities since R has been replaced by $R(r)$ in Eqs. (2.12) and (2.13). The constituent equations (see Eqs. 2.6 - 2.10 for the radial equations) for thermoacoustics are the r component of the Navier-Stokes equation, the continuity equation, the equations of state for density and entropy, and the heat transfer equation. The form of four of these remains unchanged in the transition from a constant cross-section to a varying cross-section resonator in the stack region; however, care must be

taken in forming the correct continuity equation in a duct with varying cross-section.^{42,47}

The modified continuity equation is

$$-i\omega\rho_1(x,y,r) + \rho_0(r)\nabla_{\tau} \cdot \mathbf{v}_{\tau}(x,y,r) + \frac{1}{A_p(r)} \frac{\partial}{\partial r} [A_p(r)\rho_0(r)v_r(x,y,r)], \quad (5.3)$$

where ρ_1 is the acoustic density fluctuation, ∇_{τ} is $\frac{\partial}{\partial x}\hat{\mathbf{x}} + \frac{\partial}{\partial y}\hat{\mathbf{y}}$, x and y are the transverse coordinates, r is the longitudinal coordinate, A_p is the cross-sectional area of the pore at r , \mathbf{v}_{τ} is the transverse velocity, and v_r is the longitudinal velocity. The last term in Eq. (5.3) is the only one which varies from the constant cross-section case. It requires that the volume velocity be continuous as the pore cross-sectional area changes, or since the acoustic pressure must be continuous, it requires that the specific acoustic impedance be continuous. Application of Eq. (5.3) leads to the correct wave equation for sloped stacks

$$\frac{\rho_0}{A_p(r)F(\lambda)} \frac{d}{dr} \left[\frac{A_p(r)F(\lambda)}{\rho_0} \frac{dp_1(r)}{dr} \right] + 2\alpha(\lambda, \lambda_T) \frac{dp_1(r)}{dr} + k^2(\lambda, \lambda_T)p_1(r) = 0, \quad (5.4)$$

where R is replaced with $R(r)$ from Eq. (5.2) for determining λ and λ_T . Eq. (5.4) is similar to Webster's horn equation.¹⁹ A specific example of Eq. (5.4) is the radial wave equation (Eq. 2.27) obtained by an appropriate definition of $A_p(r)$.

5.4 Pressure, Bulk Velocity, and Specific Acoustic Impedance

The derivation to follow is completely analogous to that of Chapter 2 and Ref. 12, with r dependence showing up in some previously constant terms due to the changing cross-sectional area between the plates. Restating some of the definitions of Chapter 2, define as a pore the space between two plates. Let $v_r(r)$ be the average particle velocity for a particular pore cross-section at r , n the total number of pores in the section, $A_{res}(r)$ the resonator cross-sectional area at r , $A_p(r)$ the cross-sectional area of a pore at r , $V_{rb}(r)$ the bulk velocity at r , and $\Omega(r)$ the porosity or the ratio of open area at r to $A_{res}(r)$. Volume velocity is $A_{res}(r)V_{rb}(r) = nA_p(r)v_r(r)$, but $\Omega(r) = nA_p(r) / A_{res}(r)$; hence, $v_r(r) = V_{rb}(r) / \Omega(r)$.

The equation of motion for the fluid in a pore is given by Eq. (2.14) as $i\omega\rho_0 v_r(r) = F(\lambda)(dp_1 / dr)$ which, with the expression for $v_r(r)$ above, can be written as

$$\frac{dp_1(r)}{dr} = ik(\lambda, \lambda_T)Z_{int}(r)V_{rb}(r) \quad , \quad (5.5)$$

where Z_{int} is given by Eq. (2.26). The first order bulk velocity equation is derived by inserting Eq. (5.5) into Eq. (5.4) with the result given by

$$\frac{dV_{rb}(r)}{dr} = ik(\lambda, \lambda_T) \frac{p_1(r)}{Z_{int}(r)} - \left\{ 2\alpha(\lambda, \lambda_T) + \frac{1}{A_{res}(r)} \frac{d}{dr} A_{res}(r) \right\} V_{rb}(r) \quad , \quad (5.6)$$

and the specific acoustic impedance is

$$Z(r) = \frac{p_1(r)}{V_{rb}(r)} \quad . \quad (5.7)$$

In terms of Z , Eq. (5.6) can be written as

$$\frac{dZ(r)}{dr} = ik(\lambda, \lambda_T) Z_{int}(r) \left[1 - \frac{Z^2(r)}{Z_{int}^2(r)} \right] + \left\{ 2\alpha(\lambda, \lambda_T) + \frac{1}{A_{res}(r)} \frac{d}{dr} A_{res}(r) \right\} Z(r) \quad . \quad (5.8)$$

However, Eq. 5.6 is much more stable for numerical calculations, particularly near velocity nodes where Z goes to infinity. Eq. (5.8) reduces to the constant stack cross-section plane wave result⁹ when $A_{res}(r)$ is constant throughout each section, and to the radial wave "washer" stack result, Eq. (2.27), when $A_{res}(r) = 2\pi rh$, where h is the resonator height.

5.5 Enthalpy Flow

The enthalpy flow equation⁹ is the same for sloped and constant plate spacing except that A_{res} is position dependent for sloped stacks. Let Re and Im denote the real and imaginary parts of a quantity, respectively. In terms of $p_1(r)$ and $V_{rb}(r)$, enthalpy flow is given by

$$\bar{H}_2(r) = \bar{Q}_2 + \bar{W}_2 - \bar{Q}_{loss}(r) \quad , \quad (5.9)$$

where the work flow is

$$\bar{W}_2(r) = \frac{A_{res}(r)}{2} |V_{rb}|^2 \operatorname{Re}[Z(r)] \quad . \quad (5.10)$$

$\bar{Q}_{loss}(r)$ is due to thermal conduction through the stack and the fluid in the stack.

Thermoacoustic heat flow in the stack is given by

$$\begin{aligned} \bar{Q}_2(r) = \frac{A_{res}(r)}{2} \frac{\beta T_0}{1 + N_{Pr}} & \left\{ \operatorname{Re} \left[p_1^*(r) V_{rb}(r) \left(\frac{F^*(\lambda_T)}{F(\lambda)} - 1 \right) \right] \right. \\ & \left. - \frac{T_{0r}}{\beta T_0} \frac{\rho_0 c_P}{\Omega \omega} \left| \frac{V_{rb}(r)}{F(\lambda)} \right|^2 \frac{\operatorname{Im}[F^*(\lambda_T) + N_{Pr} F(\lambda)]}{1 - N_{Pr}} \right\} \quad . \end{aligned} \quad (5.11)$$

5.6 Finite Difference Solution

The short stack approximation is a nice tool for understanding the physics of thermoacoustic engines. However, one of the assumptions of such an approximation using a one-step finite difference approach is that all quantities involved in the calculation are evaluated at the center of the stack. In the case of sloped stacks, this would require a calculation based upon the average plate spacing or the spacing at the center of the stack, thus removing the advantage of a varying plate spacing over the length of the stack. Therefore the short stack approximation is of little value for predicting the performance of sloped stack thermoacoustic engines.

To get simple meaningful results for sloped stacks and/or varying resonator cross-section in the stack region, a numerical approach is required. This is accomplished rather simply by using a finite difference scheme and employing some of the assumptions necessary for short stack calculations. Work is delivered to the hot end of the stack in typical thermoacoustic refrigerators, so that near standing wave phasing exists in the cold end of the tube. Work is generated throughout the stack, but exits the stack primarily at the cold end in prime movers driving a load, so that near-standing wave phasing exists in the hot end of the tube. Therefore, boundary layer impedance⁴⁸ and a purely real acoustic pressure are assumed at the cold rigid tube end in a prime mover and at the hot rigid tube end in a refrigerator. Pressure and impedance translation theorems (Eqs. 2.28 and 2.29 for radial systems and Eqs. 36 and 37 of Ref. 12 for plane systems) are then

used to determine these quantities at the cold stack face for prime movers and at the hot stack face for refrigerators. In addition, conservation of acoustic pressure and volume velocity are enforced when tube cross-sections are varied. Equations 4.8 and 4.9 may then be used to determine the pressure and impedance a short distance from the end of the stack by replacing L with L/N (where N is the number of integration steps in the stack) and setting B from Eq. 4.11 to

$$B = \frac{1}{T} \frac{dT}{dr} \left[\frac{F(\lambda_r)/F(\lambda) - 1}{1 - N_{pr}} \right] + \frac{1}{A_{rw}(r)} \frac{d}{dr} A_{rw}(r). \quad (5.13)$$

Repetition of this process gives the pressure and impedance at the opposite face of the stack so that heat and work flows may be calculated using Eqs. 5.11 and 5.12. For each step through the stack, the plate spacing is taken to be the plate spacing at the center of the step, so a large N is desirable. In practice, $N=20$ gives results which do not vary appreciably from much higher values of N , however, for calculations in the following chapter $N=200$ is used since computing times are not large. For refrigerators and prime movers operating beyond onset, the temperature gradient at each integration step is determined by enforcing the enthalpy flow equation, Eq. 5.9, since the temperature gradient is not generally linear in these cases.⁴⁹

Chapter 6

Sloped Stack Results for Plane and Radial Wave Prime Movers and Refrigerators

6.1 Introduction

One of the original plans in this research was to construct a sloped stack for comparison with the existing washer style stack in the radial wave prime mover. However, the natural slope of a vertical plate stack in a radial resonator is small, so that the difference in spacing at the hot and cold sides of the stack is insignificant. Calculations predict a negligible difference between the onset temperatures of comparable vertical plate and washer style stacks. An example of the small effect of naturally sloped stacks in a radial prime mover is shown in Fig. 6.1, where the solid line shows predicted results for the parallel plate stack in the radial wave prime mover (as depicted in chapter 3) and the dashed line gives results for a sloped stack having the same plate thickness as in the parallel plate case. The slope of the plates is 0.00321. The parallel plate results are the same as those shown in Fig. 4.3 for air with a constant pore size, assuming that the stack faces maintain the same temperatures as the heat exchangers. The sloped stack results were obtained by making minor adaptations to

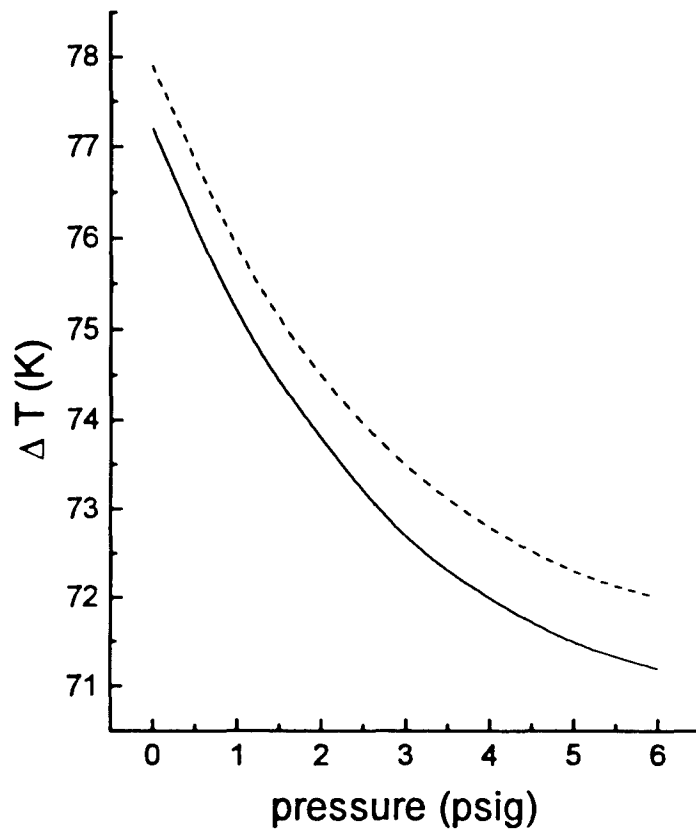


Figure 6.1: Temperature required for onset as a function of pressure for air in the radial prime mover. Solid line is for the ideal parallel plate stack described in Chapter 3 under the assumption that the stack faces maintain the same temperatures as the heat exchangers. Dashed line is for an optimized sloped stack with the same radial dimensions as the parallel plate stack.

Arnett's existing radial wave prime mover program to account for varying plate spacing through the stack. (Since the integration equations, Eqs. 2.25 and 2.27, do not change for the radial sloped stack case, only the plate spacing at each integration step required adjustment in the program to account for sloped stacks). As expected, the sloped stack increases the onset temperature since the slope is in the wrong direction for optimizing the plate spacing, but this increase is not significant since the slope between the plates is small.

Rather than construct a sloped stack to replace the existing parallel plate stack with expectations that there would be no noticeable difference in behavior, particularly when considering the non-uniform construction of the parallel plate stack as detailed in Chapter 4, a numerical examination of sloped stacks in both the plane and radial geometries for prime movers and refrigerators is presented. In order to keep the results simple, the finite difference scheme detailed in Section 5.6 will be utilized to generate sloped stack results.

Fig. 6.2 shows the four stacks which are used in the plane geometry to determine the influence of stacks with varying pore cross-section, varying resonator cross-section, and a combination of the two upon the performance of thermoacoustic engines. The resonator in all cases is square in cross-section away from the stack with sides of length 10.16 cm. *The height measured out of the paper is held constant in all cases, even in the stack region, at 10.16 cm.* Stack (A) has varying plate spacing and

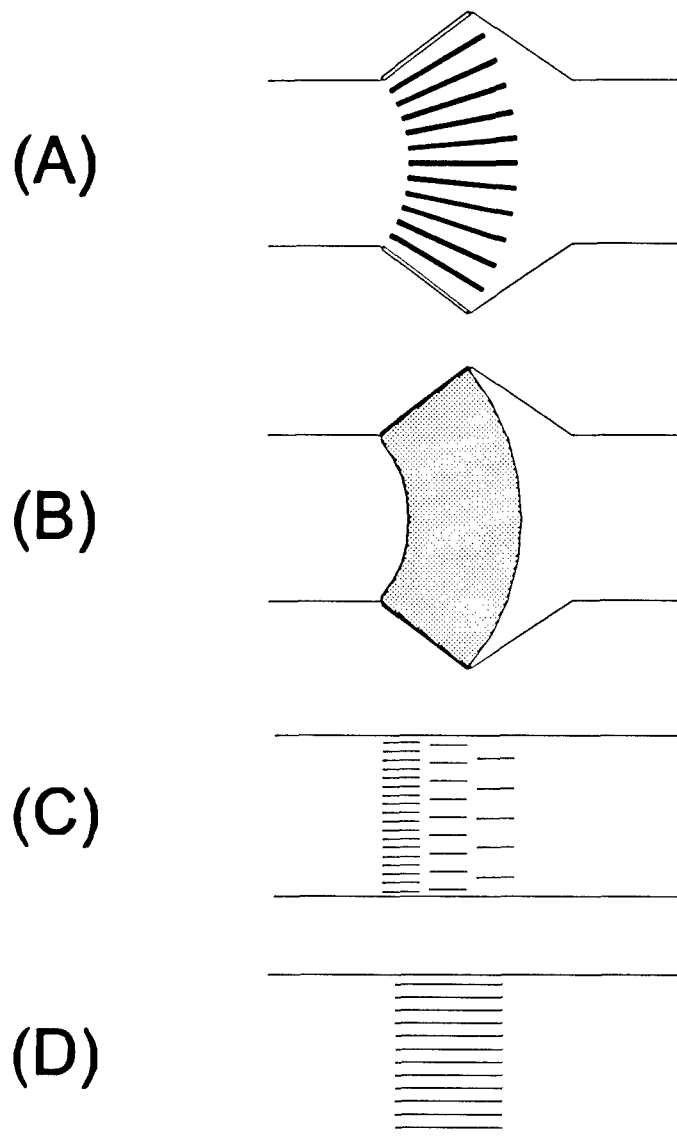


Figure 6.2: The four stacks used for plane wave calculations. In all cases the resonator height (out of the paper) is constant and the tube cross-section away from the stack is square. (A) sloped stack. (B) parallel plate stack in same tube shape as (A). (C) segmented stack. (D) parallel plate stack in constant cross-section tube.

varying tube cross-section. Stack (B) is composed of parallel plates with varying tube cross-section, and has the same resonator shape as stack (A). Stack (C) is composed of segments of parallel plates in a constant cross-section tube, with the stack plate spacing in the segments varying linearly over the length of the stack. Stack (D) is a typical parallel plate stack in a constant cross-section tube. Comparison of results from these four stacks will determine the relative importance and the magnitude of engine performance improvement generated by the two varying quantities, pore cross-section and resonator cross-section.

The prime movers and refrigerators which will be considered in the remainder of this chapter assume argon gas at an ambient pressure of 1 MPa. The resonant frequency of the system is 265 Hz, and the stack is 7.62 cm long. ϕ identifies the location of the center of the stack in the standing wave such that $\phi = \frac{\omega}{c} R_{mid}$, where R_{mid} is the axial distance from the one end of the resonator to the middle of the stack for plane systems (or the radial distance from the resonator center to the middle of the stack for radial systems), and c is the sound speed at the cold end of the resonator. The plates composing all four stacks are assumed to have infinite heat capacity and zero thickness in order to eliminate porosity variations in the different stacks.

The most general case of sloped stacks in plane wave prime movers will be considered first. For plane wave sloped stacks, the two varying quantities which may significantly effect the performance of the engine by either increasing the gain or

reducing the losses are the plate spacing and the varying resonator cross-section. Looking at the thermoacoustic equations, the changing resonator cross-section shows up as the second term in Eq. 5.13, while changing plate spacing is accounted for at each discrete step through the stack in the numerical calculation by adjusting $F(\lambda)$ and $F(\lambda_T)$.

6.2 Prime Mover Results

6.2.1 Plane Wave Prime Mover

Prime movers are usually designed to meet one of two criteria: minimizing the temperature difference necessary to induce oscillations, or maximizing the acoustic power generated by the stack. For the following calculations, we have maximized the acoustic power generated by the stack for a given temperature difference and heat flow at the hot end of the stack. The cold side temperature is $T_C = 293$ K, and the hot side temperature is $T_H = 693$ K. The fact that calculations at these temperatures yield positive work being generated by the stack assure that the temperature is sufficient for oscillations to be maintained. A specified work flow is placed in upon the system (e.g. refrigeration stack in a heat driven cooler) which would require such a temperature difference. Heat is supplied to the hot side of the stack at a rate of $Q_H = 300$ Watts. This is a fair comparison, and concerns about comparing stacks having different areas at the stack faces are removed, because a stack with a larger hot cross-section has a lower heat flow per unit area. With T_C , T_H , and Q_H specified, the stacks of Fig. 6.2 are

optimized to deliver maximum work flow or acoustic power out of the cold end of the stack. The work flow is maximized at the cold side of the stack because there is near standing wave phasing in the hot end so that the work flow there is small. In addition, a typical load placed on a prime mover, for example a thermoacoustic refrigeration unit as in a heat driven refrigerator, would be placed in the cold end of the tube, thus absorbing the acoustic power leaving the cold end of the prime mover stack.

Fig. 6.3a shows the acoustic power generated in the prime movers of Fig. 6.2 for different locations of the stack within the resonator. The hot resonator width and number of plates comprising stack (A) are varied to produce the maximum sloped stack acoustic power, shown as circles. The resulting hot resonator width is then imposed upon stack (B) and the number of plates is varied to produce the maximum parallel plate acoustic power, shown as squares. This allows a direct comparison of sloped and parallel plates, since the resonator shape is the same in both cases. Results from stacks (C) and (D), each optimized for producing acoustic power, are shown as triangles and diamonds, respectively. Fig. 6.3b shows the plate spacing at the hot and cold sides of the stack in number of thermal penetration depths for the corresponding stack configurations which produced Fig. 6.3a.

Examining Figures 6.3a and 6.3b, we see that in regions of low velocity (where ϕ is larger) the optimal configuration for all four stack types reduces to parallel plates in a constant cross-section resonator. As the stack moves into higher velocity regions which

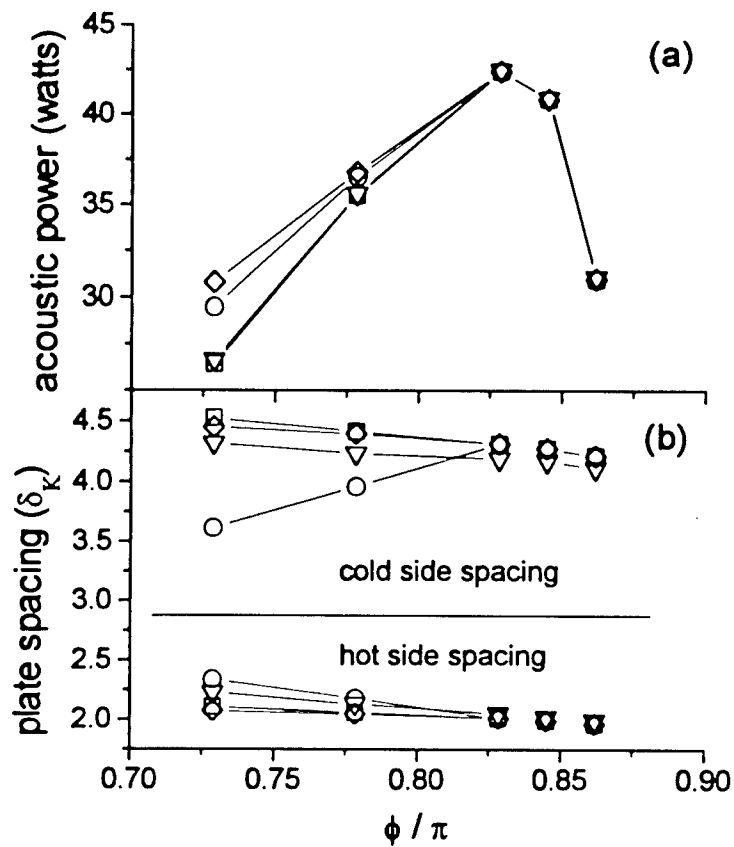


Figure 6.3: (a) acoustic power generated by the prime movers of Fig. 6.2 as a function of stack location. $T_H = 693$, $T_C = 293$, and 300W of power are delivered at the hot heat exchanger. (b) plate spacing at the hot and cold sides associated with results in (a). Four upper plots in (b) are for the cold side of the stack and the lower four are for the hot side. Circles, diamonds, triangles, and squares correspond to stacks A, B, C, and D, respectively. Fluid is argon with ambient pressure 1 MPa.

increase the viscous losses, the modified stacks (A, B, and C) begin to moderately increase the engine performance above that of the typical parallel plate stack (D). In particular, stack (B) increases the acoustic power output of the engine by at least 17% over the typical parallel plate stack (D) for $\phi/\pi < .725$. An unexpected result is that stack (A), though it generates at least 12% more power than stack (D) for $\phi/\pi < .725$, actually produces less acoustic power than stack (B). Recall that the resonator shape is the same for these two cases. This result is surprising because the sloped stack allows the stack plate spacing to more closely approach the optimal plate spacing of $2.26 \delta_K$ at both sides of the stack as seen in Fig. 6.3b. This result is understood by noticing that the segmented stack (C) is optimized with a relatively small change in plate spacing from the parallel plate case (D) and increases the acoustic power of the engine only about 2% over that of stack (D). From these results it is evident that in higher velocity regions, a larger tube cross-section at the hot end plays a major role in increasing the engine performance, and the parallel plate configuration provides a near optimum plate spacing for maximizing the net acoustic power generated by the stack. In the case of stack (A), the increasing resonator cross-section provides the improved engine performance, while the stack slope reduces engine performance. The impact of varying tube cross-sections was previously recognized by Rott in Sondhauss tubes with varying cross-section.⁴² An additional point of interest is that the hot side of the stack in all cases is in the vicinity of

the expected optimum spacing of $2.26 \delta_k$. However, the cold side spacing tends to be much higher, approximately twice the expected optimum.

These results are better understood by considering the square of the magnitude of the velocity and the real part of the impedance in each of the four stacks in a high velocity region. From Eq. 5.10 we see that the acoustic power generated by a prime mover is directly proportional to their product. Therefore, to maximize the acoustic power for a given stack location, it is desirable to have high velocity at the cold end of the stack. This may be accomplished in two ways. First, since a narrower plate spacing would lead to higher viscous loss, thus reducing the velocity, an optimized engine has a wider plate spacing at the cold side to reduce viscous loss while still providing a large net thermoacoustic gain. Second, the variation in tube cross-section in stacks (A) and (B) leads to lower velocities at the hot end and higher velocities at the cold end where work is generated. Figures 6.4a and 6.4b show $|V_{rb}|^2$ and $\text{Re}(Z)$ in the stack region for the $\phi/\pi=0.725$ results of Figures 6.3a and 6.3b. In Fig. 6.4b we see that within the stack the real impedance is changed significantly by varying the tube cross-section, however, at the cold end where acoustic power is produced the variation in all cases is less than the variation in $|V_{rb}|^2$ at the cold side of the stack, as seen in Fig. 6.4a. In addition, the parallel stack with varying tube cross-section (B) leads to a higher $|V_{rb}|^2$ at the cold end than the sloped stack (A), and thus more acoustic power is generated by the parallel

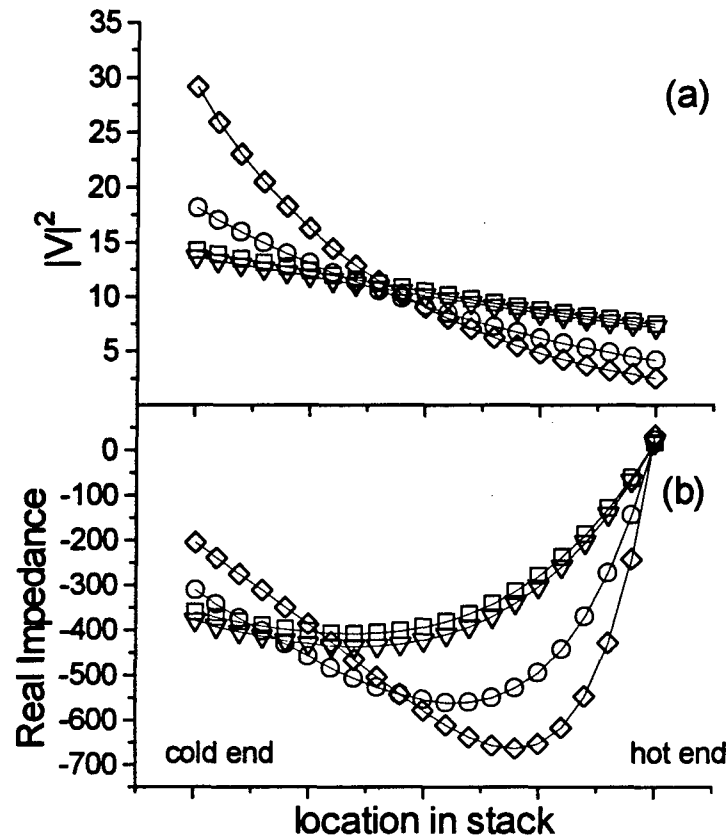


Figure 6.4: (a) Square of the magnitude of the velocity throughout the stack. Plot goes from the cold end of the stack at the left to the hot end at the right. (b) Real part of the impedance throughout the stack. Above results correspond to the $\phi / \pi = .725$ results of Fig. 6.3. $T_H = 693$, $T_C = 293$, and 300W of power are delivered at the hot heat exchanger. Fluid is argon with ambient pressure 1 MPa. Circles, diamonds, triangles, and squares correspond to stacks A, B, C, and D, respectively.

plate stack (B). This occurs because the sloped stack narrows the plate spacing at the cold end of the tube. Although this brings more fluid into thermal contact with the stack solid which should help the thermoacoustics, it also increases the viscous drag on the fluid, thus reducing the velocity. In the trade-off between increasing thermal contact and reducing viscous losses, the results indicate that the latter takes precedence in prime movers, particularly at the cold end of the stack where a high velocity is desirable.

6.2.2 Radial Wave Prime Mover

From the previous section, it is expected that a radial prime mover stack should be located outside the pressure node in order to maximize acoustic power output, since this would require a larger cross-sectional area at the hot side of the stack than at the cold side of the stack. It is anticipated that replacing the radial parallel plate stack at this location with a vertical plate sloped stack should have little effect on the acoustic power generated since the natural radial slope is extremely small compared to the slopes considered in the plane wave prime mover. In addition, the plane wave results showed that changing the plate spacing without varying the tube cross-section has only a minor effect in prime movers.

For the following results, the prime mover has a hot end temperature of 693 K, a cold end temperature of 293 K, and the heat flow into the hot heat exchanger is 1000 W. The resonator is dimensionally similar to that of the large radial prime mover discussed in Chapter 3. Fig. 6.5a shows results for a radial prime mover optimized for generating

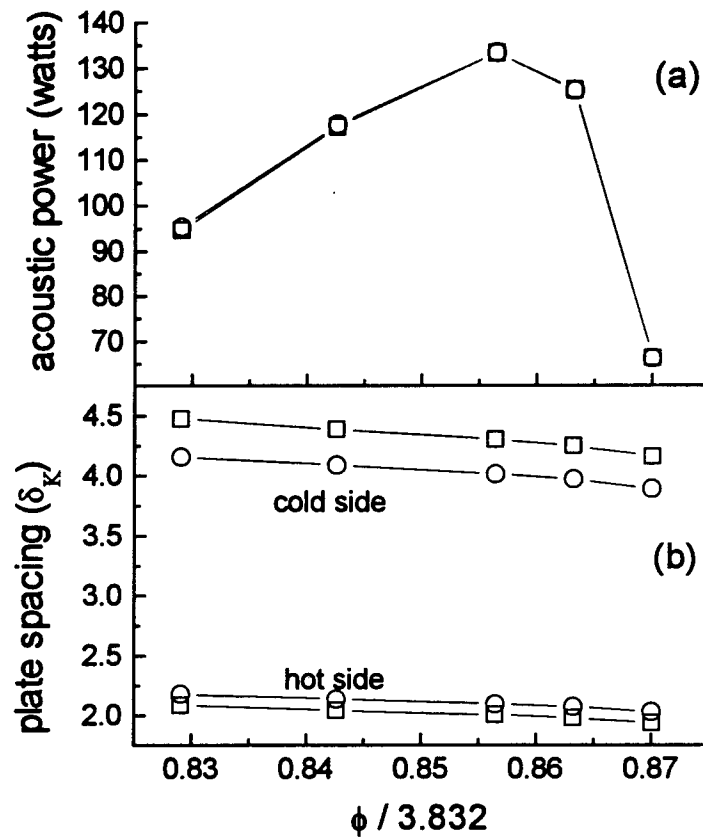


Figure 6.5 (a) radial parallel (squares) and sloped (circles) stack acoustic power as a function of stack location. $T_H = 693$, $T_C = 293$, and 1000W of power are delivered at the hot heat exchanger. Fluid is argon with ambient pressure 1 MPa. b) shows the plate spacing in number of thermal penetration depths at the cold (upper two curves) and hot sides (lower two curves).

acoustic power. As expected, the sloped stack results are nearly identical to those of the parallel plate stack due to the small slope. Fig. 6.5b shows the corresponding plate spacing at the hot and cold sides of the stack. Note that the x-axis in the radial case becomes $\phi / 3.832$ since 3.832 is the first zero of J_1 .

6.3 Refrigerator Results

6.3.1 Plane Wave Refrigerator

Refrigerators are usually designed to remove a specified heat load and maintain a specified temperature difference. The goal in refrigerator design is to maximize the coefficient of performance (COP) while meeting these design requirements, where COP is defined as the heat pumped at the cold side of the stack divided by the work absorbed at the hot side of the stack. For the following calculations the hot side temperature is $T_H = 293$, and the cold side temperature is $T_C = 273$. The heat load at the cold side of the stack, and thus the heat which must be pumped away from it, is $Q_C = 100$ W. With T_H , T_C , and Q_H specified, the stacks of Fig. 6.2 are optimized to require a minimum work flow or acoustic power at the hot end of the stack, which will create a maximum COP. Fig. 6.6a shows the maximum COP attained for each of the four stacks over a range of stack locations. Note again that the resonator has the same shape for stacks (A) and (B) and its shape has been optimized for stack (A). Fig. 6.6b shows the associated hot and cold side plate spacings.

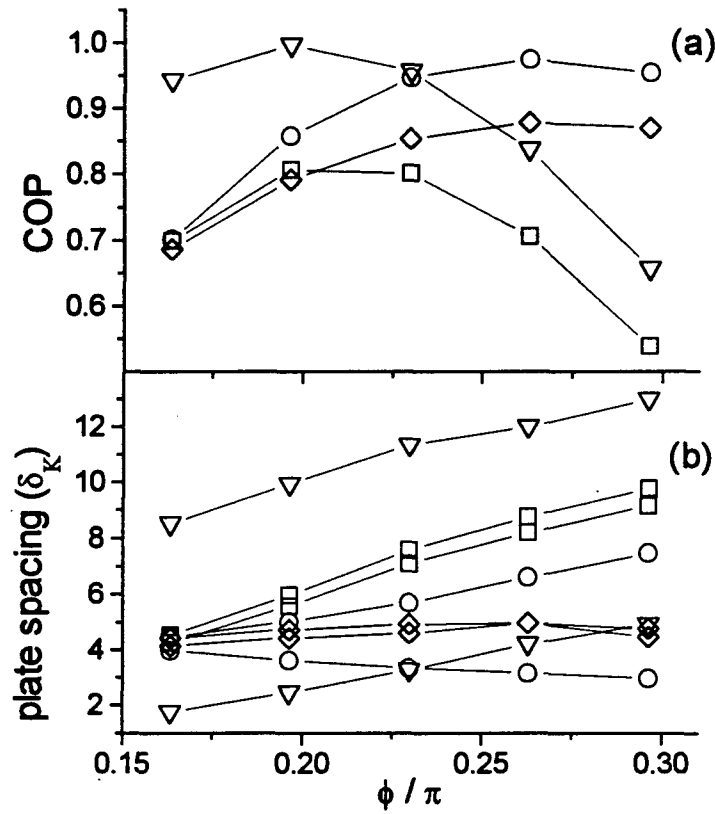


Figure 6.6: (a) COP for various stack locations. $T_H = 293$, $T_C = 273$, and heat is pumped from the cold side at a rate of 100W. (b) Stack plate spacing at the hot and cold sides in number of thermal penetration depths for the curves in (a). Wider spacings represent the cold side spacing for each stack type. Fluid is argon at an ambient pressure of 1 MPa. Circles, diamonds, triangles, and squares correspond to stacks A, B, C, and D, respectively.

Several things are immediately noticeable from these figures. First, it is clear that the segmented stack (triangles), which relies only upon changing plate spacing from the hot to the cold side and not upon changing resonator cross-section, has a significantly improved performance over the parallel plate configuration (squares). At their peaks, $\phi/\pi = .195$, the segmented stack improves the COP over parallel plates by 25%. Second, varying the tube cross-section of the tube for stacks (A) and (B) produces an increase in COP and shifts the location of the maximum COP toward the center of the tube. In this case, the sloped stack has a maximum COP nearly identical to that of the segmented stack. *The sloped stack should have particular application in heat driven refrigerators, where the refrigeration stack is typically shifted toward the center of the tube away from its prime location in order to make room for the prime mover stack.* A third point of interest is the surprisingly large plate spacings in all of the engines. The typical parallel plate arrangement, which has nearly equal plate spacings at the hot and cold sides in terms of thermal penetration depths, increases from a spacing of $4\delta_K$ to $9\delta_K$ as the stack is shifted to regions of higher velocity. Likewise, the other stack arrangements have a wider plate spacing in high velocity regions.

Fig. 6.7a shows $|V_{rb}|^2$ throughout stacks (C) and (D). These results are taken from the $\phi/\pi = .195$ results of Fig. 6.6 where the COP is maximized for these two stack types. Contrary to the prime mover case where a large velocity is desired at the cold side, in the refrigerator a small velocity is desired at the hot side in order to reduce the

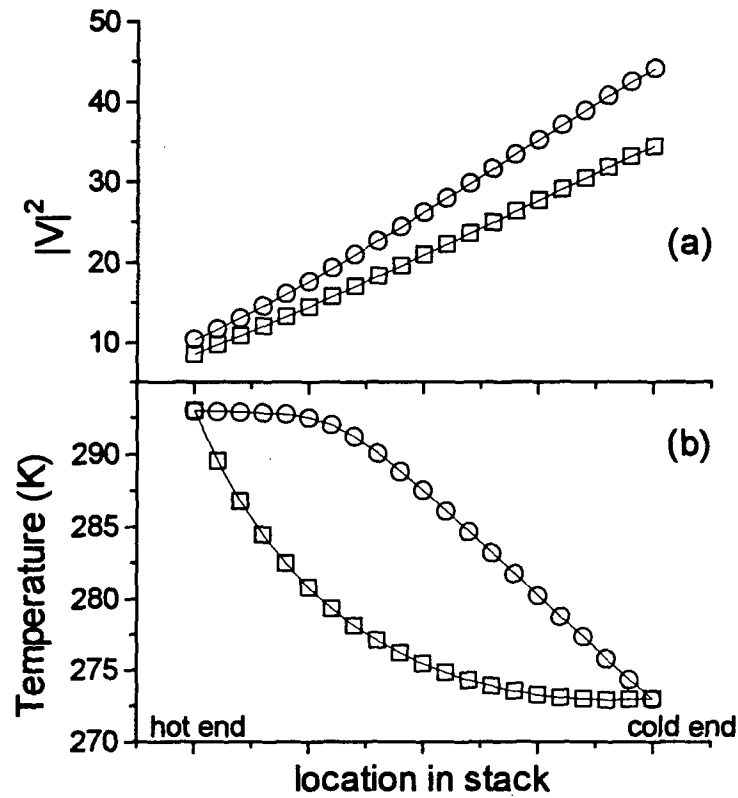


Figure 6.7: (a) Magnitude of the velocity squared throughout the stack region for parallel (circles) and segmented (squares) stacks both having a constant cross-section in the stack region. (b) Temperature profile in the stack for the two stack types. These results are taken from the $\phi / \pi = .195$ results of Fig. 6.6.

amount or work while still pumping the necessary heat across the temperature difference. The wider plate spacing in the segmented stack, particularly at the cold end, reduces the viscous losses in the stack. This decreases the acoustic pressure amplitude at the cold end of the tube necessary to pump the heat, which in turn reduces the acoustic velocity.

Integration of the velocity through the stack shows that the segmented stack velocity at the hot side of the stack is 20% lower for the segmented stack, leading to a lower work flow and thus a higher COP. An additional source of reduced viscous losses in the segmented stack is the reduction in temperature throughout the stack as seen in the temperature profile of Fig. 6.7b, since lower temperatures lead to a lower coefficient of viscosity.

Figures 6.8a and 6.8b show similar plots for stacks (A) and (B) from the $\phi/\pi = .265$ results of Fig. 6.6 where the COP is maximized for these two stack types. Comparison of Figures 6.7a and 6.8a show a large reduction in velocity at the cold side of stacks (A) and (B) below that of stacks (C) and (D) due to the varying tube cross-section. This is the reason for a shift in location of the maximum COP. Without the varying tube cross-section, the higher velocity toward the center of the tube pushes the optimal location toward the end of the tube where viscous losses are smaller. However, the varying tube cross-section allows the stack to move toward the center without increasing viscous losses.

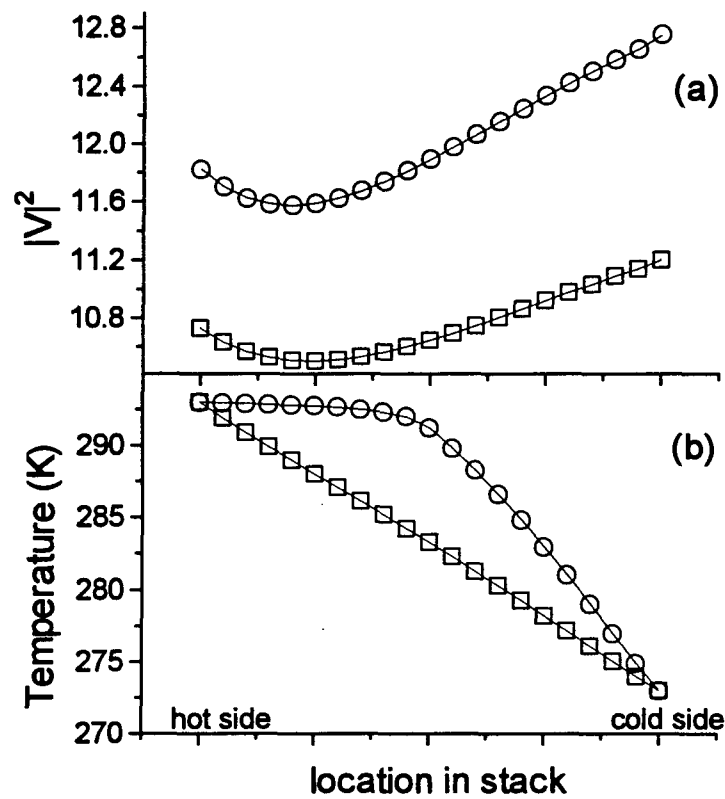


Figure 6.8: (a) Magnitude of the velocity squared throughout the stack region for parallel (circles) and sloped (squares) stacks both having varying tube cross-section in the stack region. (b) Temperature profile in the stack for the two stack types. These results are taken from the $\phi / \pi = .265$ results of Fig. 6.6.

Comparing $|V_{\text{rh}}|^2$ for stacks (A) and (B) in Fig. 6.8a, we see that the sloped stack (A) produces a 9% lower $|V_{\text{rh}}|^2$ at the hot side of the stack than the parallel stack (B), leading to a higher COP in the case of the sloped stack. The reduction in velocity for the sloped stack is again due to a reduction in the viscous losses in the cold end of the stack, which faces a velocity antinode. This decreases the acoustic pressure amplitude at the cold end of the tube necessary to pump the heat, which in turn reduces the acoustic velocity. It should be noted that the real part of the impedance was also examined for refrigerators, but the variation was much smaller than for the velocity squared. As in the constant tube cross-section case, an additional source of reduced viscous losses is the overall reduction in temperature throughout the sloped stack as seen in the temperature profile of Fig. 6.8b.

Note that these results are consistent with measurements made by Hofler for a two-segment refrigeration stack. He found that a long segmented stack with greater than a 100 K temperature span over the stack length produced more than a 50% increase in the COP over that achieved by a constant pore cross-section stack.⁵⁰ However, it should be noted that the COP's in the plane wave refrigerators considered are low (less than 10% of Carnot COP). It is likely that optimization of stack length would influence the results, though it is not known how great that influence would be. It is expected that sloped and segmented stacks would continue provide improvements to

the typical parallel plate engine, but the percent increase in COP may not be as high as the results presented here.

6.3.2 Radial Wave Refrigerator

For radial wave refrigerator calculations, the stack is set inside the pressure node so that sloped stacks will produce a wider spacing at the cold side and so that the resonator cross-section is wider at the cold side based upon the results for plane wave refrigerators. Fig. 6.9a shows the maximum COP attained by sloped and parallel stacks in the radial geometry over a range of stack locations (again, the x-axis in the radial case becomes $\phi / 3.832$ since 3.832 is the first zero of J_1). Figure 6.9b shows the associated hot and cold side spacings. The sloped stack shows more improvement over parallel stacks than in the case of the prime mover, due to the larger slope between plates since the stack is located nearer the center of the resonator. In addition, varying plate spacing was shown in the plane wave case to have a greater effect in refrigerators than in prime movers. The COP is about 7% greater than in the parallel plate case. Again, as in the plane wave case, wider plate spacings are better in regions of higher velocity in order to reduce viscous losses.

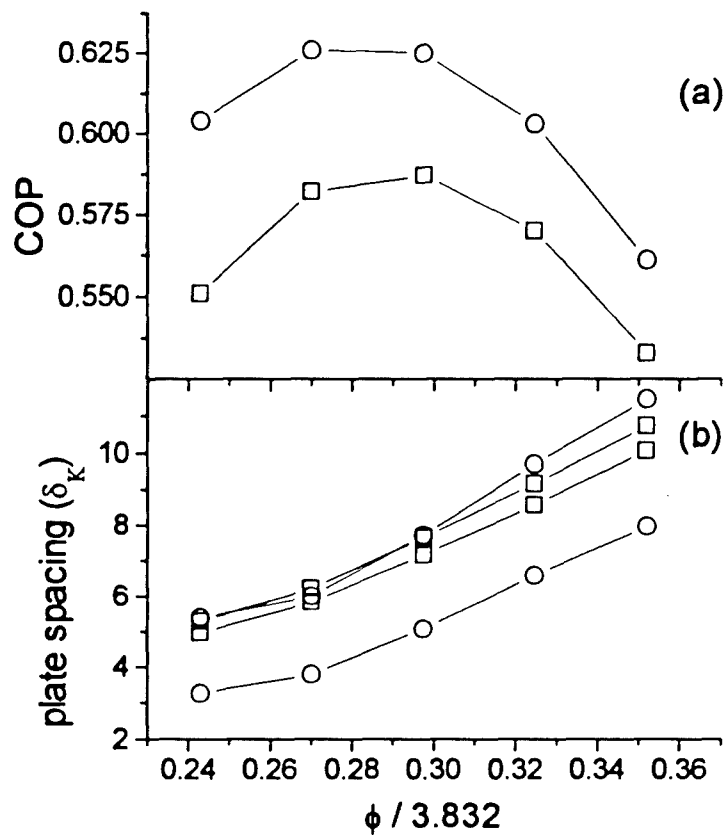


Figure 6.9: (a) radial wave parallel (squares) and sloped (circles) stack COP results. $T_H = 293$, $T_C = 273$, and heat is pumped from the cold end of the stack at a rate of 100 W. Fluid is argon at a pressure of 1 MPa. b) shows the plate spacing in number of thermal penetration depths at the hot and cold sides. The two upper spacings are for the cold side and lower spacings are for the hot side.

Chapter 7

Conclusions

The first goal for the experimental results of the radial engine was to test the generation of higher harmonics in the radial mode. This was certainly attained and the results were as expected. Comparison of harmonic generation in the radial prime mover and a similar plane prime mover showed that the radial prime mover does not enhance the generation of higher harmonics, since the resonator harmonics are not in the vicinity of multiples of the fundamental. In addition, sound pressure levels of the higher harmonics in the radial prime mover were found to be similar to those produced by a detuned plane prime mover.

A second experimental goal was to test the radial wave thermoacoustic theory. Although some satisfaction is lost in not being able to directly compare measured onset temperatures with predicted values due to unforeseen physical constraints on the system (i.e. significant gaps between stack and heat exchanger), with account taken of these physical constraints it has been shown that the existing radial wave theory is accurate and useful for future prediction of engine performance.

We accidentally identified several areas in which care should be taken in future research, and developed some useful tools in order to understand these problem areas. In

radial engines, stack plates which are rigid enough to provide a constant plate spacing should be used. Since the radial stack was characterized by a distribution of pore sizes rather than a constant pore size, a method was developed for analyzing pore distributions in the stack. This should be useful for analysis of inhomogeneous stacks (i.e. steel wool, fiberglass, etc.). In addition, some difficulties with short stacks have been discovered and understood. It was shown that the fit of the heat exchanger to the stack is much more important when short stacks are used.

The original plan to construct a sloped stack similar in dimensions to the parallel plate stack used in the radial prime mover was altered, since theory shows only small improvements in engine performance for sloped stacks over parallel plate stacks in prime movers, particularly in radial prime movers where the slope is small. Therefore, the idea of sloped stacks was extended to plane wave engines. Radial wave thermoacoustic theory for sloped stack thermoacoustic engines was derived, and theoretical predictions for prime movers were made.

For prime movers, sloped stacks were shown to have little effect in increasing the acoustic power generated by the stack; however, increasing the tube cross-section at the hot end while keeping a parallel plate stack arrangement does produce some gain in high velocity regions due to the influence that this has upon the acoustic particle velocity at the cold side of the stack where work flow is generated. The plate spacing at the hot

side of the stack was consistently near the expected value, however, in regions of higher velocity the spacing was increased to reduce viscous losses in the stack.

Thermoacoustic refrigerators appear to be a promising application for sloped and segmented stacks. Theoretical calculations show as much as a 25% increase in the COP for sloped and segmented stacks over parallel plate stacks. While the segmented stack has a maximum COP near the end of the tube (ideal for speaker driven systems), the sloped stack maximum is shifted toward the center of the tube, a particularly useful result for heat driven refrigerators. Refrigerator plate spacings are significantly higher than expected, due to the importance of minimizing the viscous losses in the stack. In the case of sloped stacks, a wider cross-section is needed at the cold side in refrigerators, since it is in a region of higher velocity and thus is prone to higher viscous losses. In addition, it was found that sloped and segmented stacks alter the temperature profile in the stack so that the average temperature in the stack is lower, further reducing the viscous losses in the stack.

List of References

List of References

1. United States Environmental Protection Agency Office of Air and Radiation Stratospheric Protection Division's March, 1995 report.
2. United States Environmental Protection Agency Office of Air and Radiation Stratospheric Protection Division, "Final regulation to accelerate the phaseout of ozone depleting substances," July 28, 1995.
3. S. C. Ballister and D. J. McKelvey, "Shipboard Electronics Thermoacoustic Cooler," M. S. Thesis, Naval Postgraduate School (1995).
4. S. K. Fischer, J. J. Tomlinson, and P. J. Hughes, "Energy and Global Warming Impact of Not-in-Kind and Next Generation CFC and HCFC Alternatives," U. S. Department of Energy, Oak Ridge National Laboratories, Oak Ridge, TN (1994).
5. G. W. Swift, "Thermoacoustic engines and refrigerators," *Physics Today* **48** (7), 22-28 (1995).

-
6. G. W. Swift, "Thermoacoustic engines," *J. Acoust. Soc. Am.* **84**, 1145-1180 (1988).
 7. N. Rott, "Thermoacoustics," *Adv. Appl. Mech.* **20**, 135-175 (1980).
 8. B. Ward and G. Swift, "Design Environment for Low-Amplitude Thermoacoustic Engines," Los Alamos National Laboratory, (1994).
 9. James R. Belcher, "A Study of Element Interactions in Thermoacoustic Engines," Ph. D. dissertation, The University of Mississippi (1996).
 10. G. W. Swift and R. M. Keolian, "Thermoacoustics in pin-array stacks," *J. Acoust. Soc. Am.* **94**, 941 (1993).
 11. T. J. Hofler, "Thermoacoustic Refrigerator Design and Performance," Ph.D. dissertation, Physics Department, University of California at San Diego, 1986.

-
12. W. P. Arnott, Henry E. Bass, and Richard Raspet, "General formulation of thermoacoustics for stacks having arbitrarily shaped pore cross-sections," *J. Acoust. Soc. Am.* **91**, 3228-3237 (1991).
 13. T. J. Hofler, "Effective heat transfer between a thermoacoustic heat exchanger and stack," *J. Acoust. Soc. Am.* **94**, 1772 (1993).
 14. N. Castro, T. J. Hofler, and A. A. Atchley, "Experimental heat exchanger performance in a thermoacoustic prime mover," *J. Acoust. Soc. Am.* **94**, 1772 (1993).
 15. G. W. Swift, "Analysis and performance of a large thermoacoustic engine," *J. Acoust. Soc. Am.* **92**, 1551 (1992).
 16. W. P. Arnott, J. A. Lightfoot, R. Raspet, and Hans Moosmüller, "Radial wave thermoacoustic engines: Theory and examples for refrigerators and high-gain narrow-bandwidth photoacoustic spectrometers," *J. Acoust. Soc. Am.* **99** (2), 734-745 (1996).

-
17. H. Tijdeman, "On the propagation of sound waves in cylindrical tubes," *J. Sound Vib.* **39**, 1-33 (1975).
 18. A. L. Fetter and J. D. Walecka, *Theoretical Mechanics of Particles and Continua* (McGraw-Hill, New York, 1980).
 19. A. D. Pierce, *Acoustics: An Introduction to Its Physical Principles and Applications* (American Institute of Physics, New York, 1980).
 20. S. V. Patankar, *Numerical Heat Transfer and Fluid Flow* (Hemisphere Publishing Co., New York, 1980).
 21. Abramowitz and Stegun, *Handbook of Mathematical Functions* (Dover Publications, Inc., New York, 1972), pp. 358-433.
 22. P. M. Morse and K. U. Ingard, *Theoretical Acoustics* (Princeton U.P., Princeton, NJ, 1986), pp. 519-522.

-
23. W. P. Arnott, J. R. Belcher, R. Raspet, and H. E. Bass, "Stability Analysis of a helium-filled thermoacoustic engine," *J. Acoust. Soc. Am.* **96** (1), 370-375 (1994).
 24. Anthony A. Atchley, "Standing wave analysis of a thermoacoustic prime mover below onset of self-oscillation," *J. Acoust. Soc. Am.* **92** (5), 2907-2914 (1992).
 25. A. A. Atchley, H. E. Bass, T. J. Hofler, and H. Lin, "Study of a thermoacoustic prime mover below onset of self-oscillation," *J. Acoust. Soc. Am.* **91** (2), 734-743 (1992).
 26. Kinsler, Frey, Coppens, and Sanders, *Fundamentals of Acoustics*, (John Wiley & Sons, Inc., New York, 1982), pp. 14-17.
 27. The ceramics were manufactured by Corning Incorporated, Industrial Products Division, Corning, New York 14831.
 28. H. Roh, W. P. Arnott, and J. M. Sabatier, "Measurement and calculation of acoustic propagation constants in arrays of small air-filled rectangular tubes," *J. Acoust. Soc. Am.* **89** (6), 2617-2624 (1991).

-
29. The Memphis, TN location of O'Neal Steel provided the unmachined pieces of the resonator. The corporate office is located at: O'Neal Steel, P.O. Box 2623, Birmingham, AL 35202-2633.
 30. Williams Machine Works, Inc., 2270 Channel Avenue, P.O. Box 13307, Memphis, TN 38113-0307.
 31. Fig. 3.10 was created by Mr. Paul Mitchell, Technical Design Specialist at the University of Mississippi.
 32. A. B. Coppens and J. V. Sanders, "Finite-amplitude standing waves in rigid-walled tubes," J. Acoust. Soc. Am. **43** (3), pp. 516-529 (1968).
 33. R. Chen, "Time Averaged Pressure Distributions for Finite Amplitude Standing Waves," Master's Thesis from Pennsylvania State University, Graduate Program in Acoustics, December, 1994.
 34. A. A. Atchley, H. E. Bass, and T. J. Hofler, "Development of nonlinear waves in a thermoacoustic prime mover," in *Frontiers of Nonlinear Acoustics: Proceedings of*

-
- 12th ISNA, edited M. F. Hamilton and D. T. Blackstock (Elsevier, New York, 1990), pp. 603-608.
35. D. F. Gaitan and A. A. Atchley, "Finite amplitude standing waves in harmonic and anharmonic tubes," J. Acoust. Soc. Am. 93 (5), pp. 2489-2495 (1993).
36. A. B. Coppens and J. V. Sanders, "Finite-amplitude standing waves within real cavities," J. Acoust. Soc. Am. 58 (6), pp. 1133-1140.
37. J. R. Olson and G. W. Swift, "Similitude in thermoacoustics," J. Acoust. Soc. Am. 95, 1405-1412 (1994).
38. Richard Raspet, James Brewster, and Henry E. Bass, "A new approximation method for thermoacoustic calculations," to be published in J. Acoust. Soc. Am.
39. F. Reif, *Fundamentals of Statistical and Thermal Physics*, (McGraw-Hill, Inc., New York, 1965), pp.166-169.

-
40. N. Rott, "Damped and thermally driven acoustic oscillations," *Z. Angew. Math. Phys.* **20**, 230 (1969).
41. N. Rott, "Thermally driven acoustic oscillations, part II: stability limit for helium," *Z. Angew. Math. Phys.* **24**, 54 (1973).
42. N. Rott, and G. Zouzoulas, "Thermally driven acoustic oscillations, part IV: tubes with variable cross-section," *Z. Angew. Math. Phys.* **27**, 197-224 (1976).
43. U. A. Müller, "Thermoakustische gasschwingungen: definition und optimierung eines wirkungsgrades," dissertation from Eidgenössischen Technischen Hochschule, 73-78 (1982).
44. N. Rott, and G. Zouzoulas, "Thermally driven acoustic oscillations, part IV: tubes with variable cross-section," *Z. Angew. Math. Phys.* **27**, 197-224 (1976).
45. U. A. Müller, "Thermoakustische gasschwingungen: definition und optimierung eines wirkungsgrades," dissertation from Eidgenössischen Technischen Hochschule, 73-78 (1982).

-
46. Bennett, "Active Cooling for Downhole Instrumentation: A Miniature Thermoacoustic Refrigerator," dissertation from the University of New Mexico, 159-162 (1991).
 47. R. Raspet and J. M. Sabatier, "The surface impedance of grounds with exponential porosity profiles," *J. Acoust. Soc. Am.* **99**, 147-152 (1996).
 48. P. M. Morse and K. U. Ingard, *Theoretical Acoustics*, (Princeton U.P., Princeton, NJ, 1986), pp. 519-522.
 49. J. C. Wheatley, "Intrinsically irreversible or natural engines," *Frontiers in Physical Acoustics* (1986), pp. 395-475.
 50. Personal communication. Experiment performed by Dr. Tom Hofler at the Naval Postgraduate School.